

2011

Crenulation Cleavage Development and the Influence of Rock Microstructure on Crustal Seismic Anisotropy

Felice Maria Johanna Naus-Thijssen

Follow this and additional works at: <http://digitalcommons.library.umaine.edu/etd>

 Part of the [Geophysics and Seismology Commons](#)

Recommended Citation

Naus-Thijssen, Felice Maria Johanna, "Crenulation Cleavage Development and the Influence of Rock Microstructure on Crustal Seismic Anisotropy" (2011). *Electronic Theses and Dissertations*. 62.
<http://digitalcommons.library.umaine.edu/etd/62>

This Open-Access Dissertation is brought to you for free and open access by DigitalCommons@UMaine. It has been accepted for inclusion in Electronic Theses and Dissertations by an authorized administrator of DigitalCommons@UMaine.

**CRENULATION CLEAVAGE DEVELOPMENT AND THE INFLUENCE OF ROCK
MICROSTRUCTURE ON CRUSTAL SEISMIC ANISOTROPY**

By

Félice Maria Johanna Naus-Thijssen

Drs. Universiteit Utrecht, the Netherlands, 2004

A THESIS

Submitted in Partial Fulfillment of the

Requirements for the Degree of

Doctor of Philosophy

(in Earth Sciences)

The Graduate School

The University of Maine

May, 2011

Advisory Committee:

Scott E. Johnson, Professor of Earth Sciences, Advisor

Christopher C. Gerbi, Assistant Professor of Earth Sciences

Edward S. Grew, Research Professor of Earth Sciences

Peter O. Koons, Professor of Earth Sciences

Martin G. Yates, Instructor of Earth Sciences

Senthil S. Vel, Associate Professor of Mechanical Engineering

Michael L. Williams, Professor of Geosciences, University of Massachusetts

THESIS
ACCEPTANCE STATEMENT

On behalf of the Graduate Committee for Félice M.J. Naus-Thijssen, I affirm that this manuscript is the final accepted thesis. Signatures of all committee members are on file with the Graduate School at the University of Maine, 42 Stodder Hall, Orono Maine.

Dr. Scott E. Johnson, Professor of Earth Sciences

LIBRARY RIGHTS STATEMENT

In presenting this thesis in partial fulfillment of the requirements for an advanced degree at The University of Maine, I agree that the Library shall make it freely available for inspection. I further agree that permission for "fair use" copying of this thesis for scholarly purposes may be granted by the Librarian. It is understood that any copying or publication of this thesis for financial gain shall not be allowed without my written permission.

Signature:

Date:

**CRENULATION CLEAVAGE DEVELOPMENT AND THE INFLUENCE OF ROCK
MICROSTRUCTURE ON CRUSTAL SEISMIC ANISOTROPY**

By Félice M.J. Naus-Thijssen

Thesis Advisor: Dr. Scott E. Johnson

An Abstract of the Dissertation Presented
in Partial Fulfillment of the Requirements for the
Degree of Doctor of Philosophy
(in Earth Sciences)
May, 2011

This thesis investigates the cause of mass transfer during crenulation cleavage formation and the role that elastically anisotropic minerals and fabric development play in promoting seismic anisotropy in the crust. Crenulation cleavage is the most common fabric in multiply-deformed, phyllosilicate-rich metamorphic rocks. During its formation the originally planar fabric gets crenulated, eventually leading to the differentiation of quartz- and feldspar-rich regions (QF-domains) in the crenulation hinges, and phyllosilicate-rich regions (P-domains) in the crenulation limbs. This differentiation is driven by the dissolution of quartz and feldspar in the P-domains, and the precipitation of those minerals in the QF-domains.

Finite element models are created to investigate how the elastic interactions of quartz and muscovite minerals affect the grain-scale stress and strain distributions at different stages of crenulation cleavage development. Gradients in mean stress and volumetric strain develop between the limbs and hinges of the microfolds during fabric formation and are sufficient to drive mass transfer between the two domains.

To study the influence of different microstructural variables on seismic wave speed anisotropy, simplified muscovite-quartz models are created with varying amounts of muscovite, varying quartz and muscovite orientations, and varying spatial distributions. The asymptotic expansion homogenization method coupled with finite element modeling (AEH-FE) is used to calculate bulk stiffness tensors and seismic wave speeds. Muscovite's abundance and preferred orientation have significant influence of seismic wave speed anisotropy due to the extreme anisotropic elasticity of the mineral.

The same method is employed to study the seismic behavior of rocks containing different stages of crenulation cleavage. Mineral orientation maps of rock samples were created, using electron backscatter diffraction, and used as input files for the AEH-FE program. Schists with a planar foliation are highly elastically anisotropic, but a rock with a well developed crenulation cleavage is much less anisotropic. These results imply that regions with larger scale crustal structures, such as folds and shear-zones, can be much more muted in their seismic signal than the schistose samples that make up those structures.

ACKNOWLEDGEMENTS

This thesis would not be lying in front of you without the help of a number of people and organizations that all deserve my gratitude. Financial support for the research was provided by both the National Science Foundation, through research grants to my advisor Scott E. Johnson, and the University of Maine, through a Provost Graduate Fellowship, a Summer Graduate Research Fellowship, and numerous Graduate Student Government Grants. Intellectually this thesis benefitted greatly from the scientific expertise and guidance from Scott Johnson, Chris Gerbi, Ed Grew, Peter Koons, Marty Yates, and Senthil Vel. Mike Williams is thanked for helpful discussions on crenulation cleavage formation and for providing me with his crenulation cleavage samples from the Moretown Formation. The collaboration with Andy Goupee from the Department of Mechanical Engineering (now at the AEWAC Advanced Structures & Composites Center) played a crucial role in conducting part of the work in this dissertation, which I gratefully acknowledge. Rachel Beane is thanked for introducing and guiding me in using the Electron Backscatter Diffraction microscope at her department. David Mainprice provided me with a version of his software specifically written for our EBSD software system, this, and his guidance and help in using his software are greatly appreciated. Additionally, the guidance and help in the use of the OOF2 software by Steve Langer and Andrew Reid of the National Institution of Standards and Technology are greatly appreciated as well.

I would also like to thank all fellow grad students at the Department of Earth Sciences and the Geodynamics and Crustal Studies Group for their friendship and support throughout the years, especially Adam Barker, Laura Brothers, Wes and Malissa Groome, Jeff Marsh, Meredith Petrie, Kathy Pingree, Chuck Rodda, WonJoon Song and Eva Wadoski. I want to direct a special thank you to Nancy Price. Your friendship (and gym-time ☺) helped me through this stage in my life, on both a professional and personal level. Thank you very much!

Without the support and love of my family back in the Netherlands I would not be where I am today. Being so far away from you was hard at times and I am really looking forward spending more time with you again once we return to Europe.

Last, but certainly not least I want to express my gratitude to, and love for Harm. Five and a half years ago we arrived in Maine (the middle of nowhere!) without knowing what to expect. These past years have been hard sometimes, but fun as well, they certainly brought us closer together. Thank you for always being there for me! You are my rock!

TABLE OF CONTENTS

| | |
|------------------------|------|
| ACKNOWLEDGEMENTS | iii |
| LIST OF FIGURES | ix |
| LIST OF TABLES | xiii |

Chapter

| | |
|---|----|
| 1. INTRODUCTION | 1 |
| 1.1 Aim of Study..... | 1 |
| 1.2 Introduction to Crenulation Cleavage..... | 2 |
| 1.2.1 Mass Transfer of Felspar | 3 |
| 1.2.2 Mass Transfer of Quartz | 4 |
| 1.3 Introduction to Seismic Anisotropy..... | 5 |
| 1.3.1 Rock Microstructures..... | 6 |
| 1.3.2 Crenulation Cleavage..... | 6 |
| 1.4 Geologic Setting | 6 |
| 2. NUMERICAL MODELING OF CRENUATION CLEAVAGE | |
| DEVELOPMENT: A POLYMINERALIC APPROACH | 9 |
| 2.1 Chapter Abstract | 9 |
| 2.2 Introduction..... | 10 |
| 2.3 Background..... | 12 |
| 2.3.1 General Observations..... | 12 |
| 2.3.2 Previous Modeling..... | 13 |
| 2.3.3 Mass Transfer | 15 |

| | | |
|---------|---|----|
| 2.4 | Numerical Modeling | 15 |
| 2.4.1 | Anisotropic Elasticity | 15 |
| 2.4.2 | Method..... | 17 |
| 2.4.3 | Model Results | 19 |
| 2.4.3.1 | Maps | 19 |
| 2.4.3.2 | Statistical Analysis of the Data | 21 |
| 2.5 | Discussion..... | 25 |
| 2.5.1 | Model Results | 25 |
| 2.5.1.1 | Influences of the Orientation of the Quartz Grains..... | 25 |
| 2.5.1.2 | Comparison of Different Domains and Stages | 26 |
| 2.5.1.3 | Skewness and Kurtosis of the Data..... | 26 |
| 2.5.2 | Implications for Crenulation Cleavage Development..... | 27 |
| 2.6 | Summary and Conclusions | 32 |
| 3. | THE INFLUENCE OF MICROSTRUCTURE ON SEISMIC WAVE SPEED ANISOTROPY IN THE CRUST: COMPUTATIONAL ANALYSIS OF QUARTZ-MUSCOVITE ROCKS | 33 |
| 3.1 | Chapter Abstract | 33 |
| 3.2 | Introduction..... | 34 |
| 3.3 | Background..... | 37 |
| 3.3.1 | Analytical Bounds and Estimates | 38 |
| 3.3.2 | Asymptotic Expansion Homogenization Formulation with Finite Element Implementation..... | 39 |
| 3.3.3 | Wave Propagation and Measures of Seismic Anisotropy | 42 |
| 3.4 | Creation of the Synthetic Rock Microstructures..... | 44 |

| | | |
|-------|--|----|
| 3.5 | Results and Discussion | 46 |
| 3.5.1 | Comparison of AEH and Analytic Estimates | 48 |
| 3.5.2 | Sensitivity Analysis of Modal Abundances, Orientations, and Spatial Distribution | 51 |
| 3.6 | Conclusions..... | 57 |
| 3.7 | Details of the Asymptotic Expansion Homogenization Method | 58 |
| 4. | THE INFLUENCE OF CRENULATION CLEAVAGE DEVELOPMENT ON THE BULK ELASTIC PROPERTIES AND SEISMIC WAVE VELOCITIES OF PHYLLOSILICATE-RICH ROCKS..... | 61 |
| 4.1 | Chapter Abstract | 61 |
| 4.2 | Introduction..... | 62 |
| 4.3 | Samples..... | 65 |
| 4.4 | EBSD Orientation Mapping..... | 66 |
| 4.4.1 | Sample Preparation..... | 67 |
| 4.4.2 | Data Acquisition | 68 |
| 4.4.3 | Data Processing | 68 |
| 4.5 | Calculation of Bulk Elasticity Data | 70 |
| 4.5.1 | Voigt and Reuss Bounds..... | 70 |
| 4.5.2 | AEH-FE Method..... | 72 |
| 4.5.3 | Single Crystal Properties | 73 |
| 4.6 | Results..... | 74 |
| 4.6.1 | Cleanup Procedure..... | 74 |
| 4.6.2 | Calculation of Bulk Elastic Properties..... | 75 |

| | | |
|-------|--|-----|
| 4.7 | Discussion..... | 82 |
| 4.7.1 | Sample Preparation and Cleanup Procedure..... | 82 |
| 4.7.2 | Calculation of Bulk Elastic Properties..... | 83 |
| 4.7.3 | Geological Implications..... | 84 |
| 4.8 | Summary and Conclusions | 87 |
| | REFERENCES | 89 |
| | APPENDIX A. A SENSITIVITY STUDY REGARDING RESULTS OBTAINED WITH AEH-FE..... | 104 |
| | APPENDIX B. MASS TRANSFER OF QUARTZ DURING CRENULATION CLEAVAGE FORMATION: A CATHODOLUMINESCENCE STUDY..... | 116 |
| | BIOGRAPHY OF THE AUTHOR..... | 140 |

LIST OF FIGURES

| | | |
|--------------|---|----|
| Figure 1.1. | Backscatter electron image of a P-domain from a stage IV crenulation cleavage sample from the Mooselookmeguntic Pluton aureole..... | 4 |
| Figure 1.2. | Tectonostratigraphic units of New England, USA | 8 |
| Figure 2.1. | Photomicrograph of crenulation cleavage | 11 |
| Figure 2.2. | Six stages of crenulation cleavage development | 12 |
| Figure 2.3. | Stiffness matrix for Quartz and Muscovite in GPa at room temperature and atmospheric pressure..... | 16 |
| Figure 2.4. | Model setup | 17 |
| Figure 2.5. | Boundary conditions | 19 |
| Figure 2.6. | Contour maps of the mean stress and volumetric strain for the three different stages of the model with the randomly oriented quartz grains..... | 20 |
| Figure 2.7. | Detail of the volumetric strain map from stage 3, model I..... | 22 |
| Figure 2.8. | Average mean stress and average volumetric strain in the quartz grains per structural domain | 23 |
| Figure 2.9. | Skewness and kurtosis of the mean stress and volumetric strain datasets | 23 |
| Figure 2.10. | Gradients between Q- and X- or P-domains in %..... | 24 |
| Figure 2.11. | Schematic diagram of fluid flow at stages 2, 3, and 4 of crenulation cleavage development | 30 |
| Figure 3.1. | Correlation between the large scale structure and the microstructure | 37 |
| Figure 3.2. | Construction of the microstructure | 46 |
| Figure 3.3. | Characteristic functions and shear strain and stress for the microstructure shown in Figure 3.2b | 47 |
| Figure 3.4. | P- and S-velocities, P-delay and shear wave splitting calculated for three separate microstructural models shown at the top of the figure | 50 |

| | | |
|-------------|---|-----|
| Figure 3.5. | P and S velocities, P-delay and shear wave splitting as a function of incidence angle γ for microstructures with muscovite modal fractions of $\varphi_{Ms} = 0$, $\varphi_{Ms} = 0.3$, $\varphi_{Ms} = 0.6$, $\varphi_{Ms} = 0.9$, and varying quartz orientations..... | 53 |
| Figure 3.6. | P and S velocities, P-delay and shear-wave splitting as a function of incidence angle γ for microstructures with muscovite modal fractions of $\varphi_{Ms} = 0.3$, $\varphi_{Ms} = 0.6$, $\varphi_{Ms} = 0.9$, and varying muscovite orientation distributions. | 54 |
| Figure 3.7. | Percentage anisotropy of the P-wave, percentage anisotropy of the S-waves, and $V_p(45^\circ)$ as a function of the modal fraction of muscovite..... | 55 |
| Figure 4.1. | Six stages of crenulation cleavage development | 63 |
| Figure 4.2. | Photomicrographs (in plane and crossed polarized light) of sample areas <i>a</i> , <i>b</i> , and <i>c</i> | 64 |
| Figure 4.3. | EBSD orientation maps and equal area, lower hemisphere pole figures of the main axes of biotite, muscovite, and quartz for map <i>a</i> | 76 |
| Figure 4.4. | Cleaned EBSD data for map <i>b</i> | 77 |
| Figure 4.5. | Cleaned EBSD data for map <i>c</i> | 78 |
| Figure 4.6. | Comparison of the Voigt, Reuss, VRH, and AEH-FE stiffness components for the three mapped areas shown in Figures 4.3-4.5 | 79 |
| Figure 4.7. | P and S velocities for the three mapped areas shown in Figures 4.3-4.5 | 80 |
| Figure 4.8. | 3D velocity plots for the three mapped areas shown in Figures 4.3-4.5..... | 81 |
| Figure 4.9. | Influence of structure on seismic anisotropy from micro- to macroscale | 86 |
| Figure A1. | Sample DH13..... | 106 |
| Figure A2. | Sample D3053..... | 107 |

| | | |
|------------|---|-----|
| Figure A3. | Examples of meshes for different window sizes and mesh densities for sample MT23P1 | 109 |
| Figure A4. | The AEH stiffnesses for increasing window sizes for the three different samples | 111 |
| Figure A5. | Comparison of the C11 and C22 stiffness moduli for samples DH13 and D3035 calculated from the entire map, the average of 9 tiled samples covering the entire map, 30 random samples from the entire map, and the cumulative average of the random samples. | 112 |
| Figure A6. | C11, C22 and C33 stiffness components calculated from the average of multiple window sizes with comparable mesh densities and with different mesh densities | 114 |
| Figure B1. | Five stages of crenulation cleavage formation as found in the Mooselookmeguntic Pluton aureole | 118 |
| Figure B2. | Geological map of the area east of the Mooselokmeguntic Pluton, western Maine showing the sample locations | 119 |
| Figure B3. | Color CL and corresponding BSE images of specific features within each sample from the Mooselookmeguntic Pluton aureole..... | 125 |
| Figure B4. | Color CL and corresponding blue component CL and BSE images for sample MT1G1 | 126 |
| Figure B5. | Mosaic of color CL images of sample D3034 | 128 |
| Figure B6. | Mosaic of color CL maps of sample D3051 | 129 |
| Figure B7. | Mosaic of color CL maps of sample Ra36n..... | 130 |
| Figure B8. | Mosaic of color CL maps of sample MT1G1 | 131 |
| Figure B9. | Average wt% of Ti per point measurements for 4 quartz grains from sample Ra36n..... | 132 |

Figure B10. Wt% of Ti per point measurement per individual spectrometer for four
quartz grains from sample Ra36n133

LIST OF TABLES

| | | |
|------------|---|-----|
| Table 4.1. | Percentage maximum anisotropy for the P- and S- waves for the three mapped areas based on the 3D velocity calculations..... | 81 |
| Table A1. | Overview of the number of elements for the different window sizes and mesh densities for sample MT23P1..... | 110 |
| Table B1. | Probe analysis measurements of wt% Ti for four quartz grains from sample Ra36n..... | 134 |

Chapter 1

INTRODUCTION

1.1. Aim of Study

To reconstruct the tectonic history of an area, geologists need to understand the deformational and kinematic processes that occur below the earth's surface. In order to learn more about these processes it is important to understand how the strength of rocks is influenced by the microstructures within them. Part of this thesis investigates the evolution of an important microstructure in the upper and middle crust, namely crenulation cleavage. The role of grain-scale elastic interactions on mean stress and volumetric strain distributions in a rock with this fabric is investigated using an object-oriented finite element code (OOF2). Three models representing three stages of crenulation cleavage formation were created in which quartz and muscovite grains were assigned their own 3D stiffness tensor and orientation. These geometries were subjected to 1% horizontal shortening. The stress and strain heterogeneities that developed throughout the fabric are dependent mainly on the orientations of the elastically anisotropic phyllosilicate grains that define the fabric. The volumetric strain gradients approximate pore fluid pressure gradients which are sufficient to drive the mass transfer that is responsible for forming the characteristic mineralogical differentiation in this fabric.

Seismology is the primary tool used to gain information on the mineralogy and structure of deeper parts of the earth. Detailed seismic studies provide constraints on the distribution of velocities within the mantle and crust. In order to interpret these velocity distributions and relate them to the processes that formed them, velocity measurements of different rock types are necessary. These velocity measurements can be made through petrophysical studies, by directing high frequency waves at an oriented rock sample, or can be calculated from the crystallographic orientation measurements of minerals in a polished rock sample. Part of this thesis investigates the role of different microstructural parameters, such as modal mineralogy, crystallographic

(preferred) orientations, and spatial distributions, to wave velocities of synthetic quartz-muscovite rock structures using asymptotic expansion homogenization with an implementation of the finite element method (AEH-FE). The effects of crenulation cleavage formation on seismic wave velocities is investigated as well, using mineral orientation maps as an input for the AEH-FE method. Both studies show that the orientations of the highly elastically anisotropic phyllosilicate grains play an important role in determining the seismic anisotropy of a rock. In rocks containing 50% muscovite with a planar foliation, anisotropy of the P- and S-waves can be up to 35% and 50% respectively (for synthetic cases with a perfect alignment of muscovite grains). The presence of a well-developed crenulation lowers the amount of anisotropy because the orientations of the micas on opposite sides of the microfold limbs cancel one another effectively out. These results can be correlated to larger structures, such as folds, and imply that the seismic signal of a deformed region might be much more muted in its seismic anisotropy than that the schistose samples that make up these structures.

This chapter contains a short introduction to crenulation cleavage formation and seismic anisotropy, and describes the geological setting of the samples used in this study. More detailed background information regarding these topics can be found in the various chapters of this thesis. Chapter 2 investigates the grain-scale elastic interactions in rocks with a crenulation cleavage and how the resulting gradients in mean stress and volumetric strain contribute to driving mass transfer. Chapter 3 describes how different microstructural features influence the seismic anisotropy of the crust. Chapter 4 focuses on a particular microstructure, crenulation cleavage, and studies how different stages in its evolution influences seismic anisotropy.

1.2. Introduction to Crenulation Cleavage

Crenulation cleavage is one of the most commonly formed fabrics in multiply-deformed, meta-pelitic, crustal rocks (e.g., Williams et al., 2001). The fabric is characterized by the differentiation of minerals into a phyllosilicate-rich (P-) domain, in which the phyllosilicates

define the overall cleavage, and a quartz- and feldspar-rich (QF-) domain. The characteristic mineralogical differentiation into P- and QF-domains that takes place during crenulation cleavage formation is the result of dissolution of quartz and feldspar in the P-domains, and precipitation of these minerals in the QF-domains (e.g., Gray and Durney, 1979; Mancktelow, 1994). It is possible that part of the dissolved material is removed from the local system (Bell et al., 1986; Wright and Henderson, 1992). The phyllosilicates in the P-domains undergo recrystallization and neocrystallization, but there is no evidence for any mass transfer of phyllosilicates during crenulation cleavage development (e.g., Marlow and Etheridge, 1977; Worley et al., 1997; Williams et al., 2001). Both stress- (Durney, 1972; Robin, 1979; Rutter, 1983) and strain- (Bell et al., 1986; Vernon, 2004) induced dissolution are postulated as possible driving forces for both the dissolution and mass transfer from P- to QF-domains during crenulation cleavage formation. Chapter 2 of this thesis explores the stress and strain distributions within a developing crenulation cleavage and gives suggestions on what processes are most likely to cause material to dissolve and move.

1.2.1 Mass Transfer of Feldspar

High resolution chemical mapping has proven to be a good tool for investigating mass transfer of feldspar during crenulation cleavage development. Williams et al. (2001) performed such a study on rocks from the Moretown Formation and found overgrowths on the feldspar grains that were indicative of them being formed during crenulation cleavage formation. They found that during the formation of the fabric 10-20% plagioclase grew in the hinge-domains of the crenulation cleavage, and only 1% plagioclase and a large amount of phengitic muscovite grew in the limb-domains of the crenulation cleavage.

Chemical mapping on rocks from the Mooselookmeguntic pluton aureole shows that some plagioclase grains do have more sodic overgrowths on more calcic cores (which is the opposite from the chemistry reported by Williams et al., 2001). Figure 1.1 shows a backscatter

electron image of a P-domain from a sample with a well developed crenulation cleavage from the Mooselookmeguntic Pluton aureole, the boxes indicate plagioclase grains that were mapped using the CAMECA SX-100 electron microprobe at the Department of Earth Sciences, University of Maine. The overgrowths on the plagioclase grains in this figure are also visible in BSE images, and most plagioclase grains in the samples investigated did not show this structure in the BSE image. Also, the chemical variation in the plagioclase grains from the Moretown Formation is clearly visible in cathodoluminescence (CL), whereas the plagioclase grains from the Mooselookmeguntic Pluton aureole have a very homogeneous blue CL color (see also Appendix B). Although no mapping is performed to investigate the spatial distribution and variation of the overgrowths shown in Figure 1.1, I think for the reasons mentioned above that most plagioclase grains in these rocks are probably relatively homogeneous and not suitable to investigate mass transfer of plagioclase during crenulation cleavage formation.

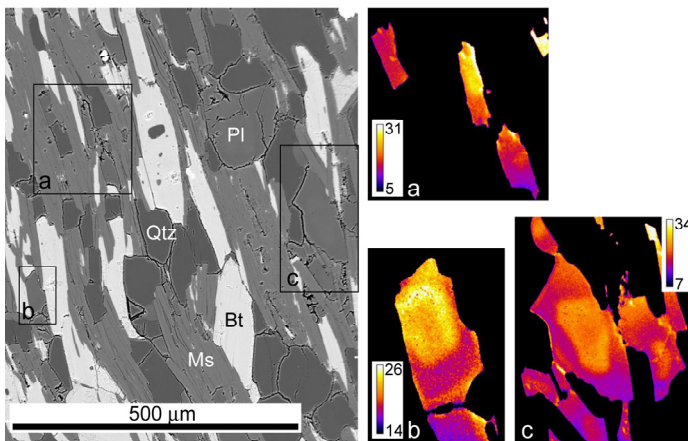


Figure 1.1. Backscatter electron (BSE) image of a P-domain from a stage IV crenulation cleavage sample from the Mooselookmeguntic Pluton aureole. The color images are CaK α maps of the plagioclase grains indicated in the BSE image. Scaling is in An content (= Ca/(Ca+Na)).

1.2.2 Mass Transfer of Quartz

Cathodoluminescence is a good method to study the mass transfer of quartz, because the chemical variation within quartz is typically not sufficiently large for chemical mapping with the electron microprobe. The mass transfer of quartz during crenulation cleavage formation is explored in Appendix B of this thesis. The results of this exercise show that quartz grains in the

rocks from the Moretown Formation have overgrowths that are similar in geometry to the overgrowths Williams et al. (2001) found in the plagioclase grains of the same rocks. Quartz in rocks from the Mooselookmeguntic Pluton aureole show internal structures that are apparently related to pluton emplacement, but not clearly related to crenulation cleavage formation; they are therefore probably not suitable to study the mass transfer of quartz during crenulation cleavage formation.

1.3. Introduction to Seismic Anisotropy

Geophysicists use seismicity as a tool to investigate the structure and mineralogy of the deeper parts of the earth. When a seismic wave travels through a rock volume that has an anisotropic bulk stiffness, the wave velocity will have a directional dependence (i.e. it will travel faster or slower in certain directions). During deformation elastically anisotropic minerals are aligned and redistributed, causing the formation of a crystallographic preferred orientation which will cause an anisotropic seismic signal to be picked up by seismometers. Numerous detailed seismic studies have given valuable information on the distribution of velocities at deeper levels of the earth, providing information regarding processes like mantle-crust coupling and tectonic plate interactions (e.g., Christensen, 1985; Christensen and Mooney, 1995; Silver, 1996; Mooney, 2007; Karato, 2008). Most research regarding seismic anisotropy is focused on mantle kinematics and its correlation to the flow of elastically anisotropic olivine grains (e.g., Karato, 1987; Nicolas and Christensen, 1987; Silver, 1996; Savage, 1999; Mainprice et al., 2000; Tommasi et al., 2000; Montagner and Guillot, 2002; Mainprice, 2007; Karato et al., 2008), but crustal seismic anisotropy can affect the shear wave splitting values caused by mantle structures. In order to do so the degree of crustal anisotropy must be significant and appropriately oriented (e.g., Okaya et al., 1995; Godfrey et al., 2000).

1.3.1. Rock Microstructure

Causes for seismic anisotropy in the crust are (1) the presence of aligned fractures or cracks (in the upper 10-15km of the crust) (e.g., Crampin, 1981; Kaneshima et al., 1988), (2) the layering of isotropic or anisotropic material (e.g., Backus, 1962), and (3) the orienting of anisotropic minerals forming lattice and shape preferred orientations (LPO and SPO respectively) through deformation (e.g., Mainprice, 2007). The influence of this last factor is further explored in Chapter 3 of this thesis. In this chapter the modal abundances of quartz and muscovite, spatial distributions, and crystallographic and shape preferred orientations are systematically varied and the bulk elastic properties and seismic wave velocities are calculated.

1.3.2. Crenulation Cleavage

The influence of a specific rock microstructure, namely crenulation cleavage, on bulk elastic properties and seismic wave velocities is investigated in Chapter 4 of this thesis. The seismic anisotropy of a sample containing a well-developed crenulation cleavage is significantly lower than that of a sample containing a planar foliation or less-developed crenulation cleavage. These findings regarding the small-scale folds in the crenulation cleavage can be extrapolated to larger scale folds, implying that regions that have undergone deformation and folding might be less anisotropic than that the petrophysical measurements from schistose rock samples from those areas imply.

1.4. Geologic Setting

Although this thesis mainly deals with simplified, two-phase geometries that represent a crenulation cleavage fabric, Chapter 4 and Appendices deal with natural rock examples containing this fabric. The samples that are discussed in these parts are from the Moretown Formation in western Massachusetts and the Mooselookmeguntic Pluton aureole in western Maine. Crenulation cleavage can form in different geological settings, as is illustrated by these

rocks. The samples from the Moretown formation contain a crenulation cleavage that formed by regional strain, in a tectonic setting, whereas the samples from the Mooselookmeguntic Pluton aureole contain a crenulation cleavage that is formed within a strain gradient caused by pluton emplacement.

Both research areas are part of a series of north-south trending tectonostratigraphic units that make up the north-eastern part of the United States, and the northern part of the Appalachians (see Figure 1.2). Both sample suites show a gradient in crenulation cleavage formation, displaying different stages in crenulation cleavage development as described by Bell and Rubenach (1983). In the Moretown formation this gradient is present from limb (almost no development of crenulation cleavage) to hinge (strongly developed crenulation cleavage) of meter-scale folds (Williams et al., 2001; Scheltema, 2003). In the Mooselookmeguntic Pluton aureole one can also find this kind of a limb-hinge gradient, but more important is the gradient we find spatially in the aureole, from a faint deflection of the regional foliation approximately 3 km from the pluton to an intense, margin parallel foliation adjacent to the pluton (Johnson et al., 2006).

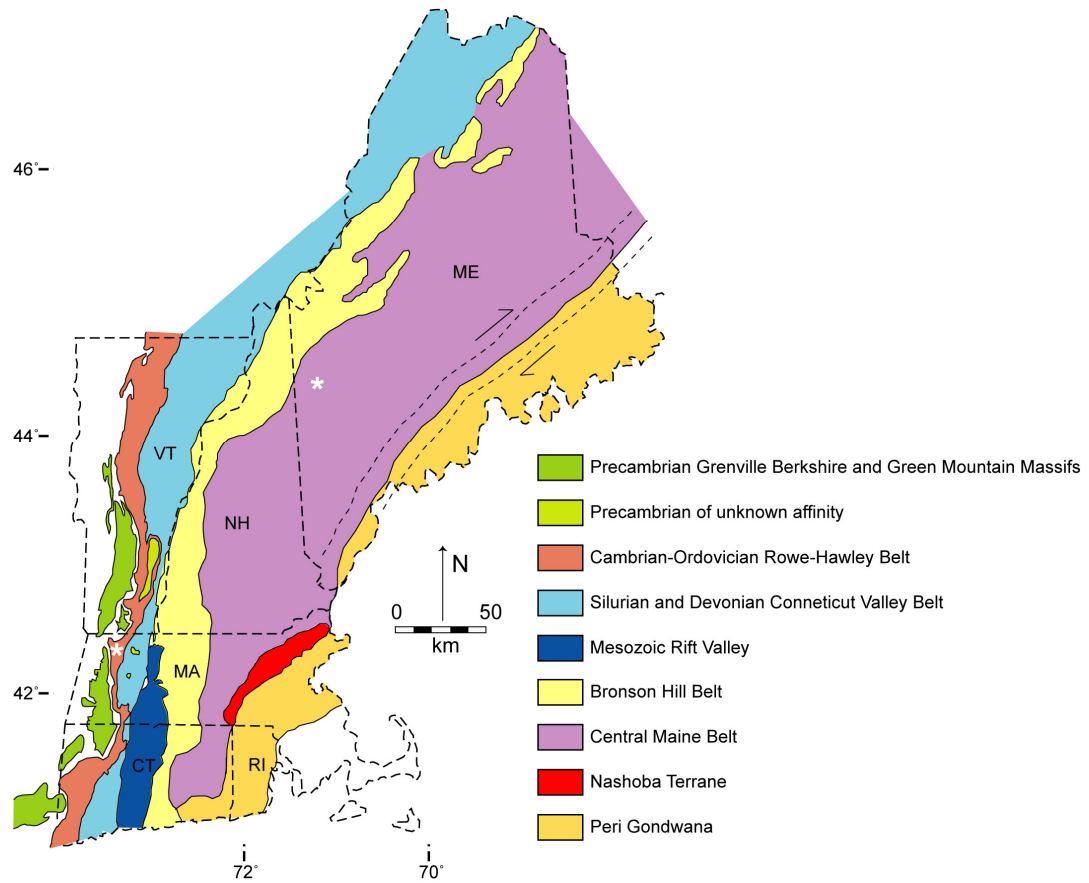


Figure 1.2. Tectonostratigraphic units of New England, USA. White asterisks indicate research areas (the Mooselookmeguntic Pluton aureole in western Maine and the Moretown Formation in western Massachusetts. Modified from Scheltma, 2003 and Tomascak et al., 2005.

Chapter 2

NUMERICAL MODELING OF CRENULATION CLEAVAGE DEVELOPMENT: A POLYMINERALIC APPROACH*

2.1. Chapter Abstract

The finite element method was used to investigate how the elastic interactions of quartz and muscovite minerals affect grain-scale stress and strain distributions at different stages of crenulation cleavage development. The polymineralic structure comprises individual grains that were each assigned their own 3D stiffness tensor and orientation. Gradients in mean stress and volumetric strain within quartz grains develop between the limbs and hinges of microfolds at the earliest stages of crenulation development, with higher values in the microfold limbs. These gradients decrease with development of the crenulation cleavage, as the microfold limbs become phyllosilicate-rich (P) domains and the hinges become quartz- and feldspar-rich (QF) domains. Crystallographic orientations of the quartz grains have a relatively minor affect on the mean stress and volumetric strain distributions.

Our findings are broadly consistent with both pressure solution and strain-driven dissolution models for crenulation cleavage development. However, because crenulation cleavage development typically involves metamorphic reactions, we favor a model in which dissolution is driven by those reactions, and mass-transfer leading to development of the mineralogically segregated fabric is driven by pore fluid pressure gradients that follow gradients in volumetric strain. Local concentrations of stress and strain across mineral interfaces may identify sites of enhanced reaction.

* *The content of this chapter is published in: Naus-Thijssen et al., 2010. Journal of Structural Geology, v.32, p. 330-341.*

2.2. Introduction

Although crenulation cleavage is the most common type of cleavage in multiply-deformed, intermediate to high-grade metapelitic rocks (Williams et al., 2001), its formation and role in strain partitioning across a range of scales is incompletely understood. Crenulation cleavage is characterized by phyllosilicate-rich (P) domains, in which phyllosilicates define the overall cleavage, separated by quartz- and feldspar-rich (QF) domains (Figure 2.1). Quartz grains in this fabric show little to no evidence for internal deformation or recrystallisation (Vernon and Clarke, 2008 and references therein). The characteristic mineralogical differentiation is therefore thought to result from dissolution of quartz and feldspar in the P-domains and precipitation of the dissolved material in the QF-domains (e.g., Gray and Durney, 1979; Schoneveld, 1979; Mancktelow, 1994). Alternatively, some percentage of the dissolved material may be removed from the local system (e.g., Bell et al., 1986; Wright and Henderson, 1992). There are two dominant hypotheses for crenulation cleavage formation. Pressure solution is most commonly invoked as the driving force for both dissolution and mass transfer from P-domains to QF-domains in both slaty cleavage (e.g., Sorby, 1863; Durney, 1972; Robin, 1979) and crenulation cleavage (e.g., Durney, 1972; Robin, 1979; Rutter, 1983). Pressure solution, sometimes referred to as dissolution or solution (-precipitation) creep or (stress-induced) dissolution and/or solution transfer, involves (1) the dissolution of material at grain boundaries that are subjected to a high normal stress, (2) diffusion of dissolved material down a chemical potential gradient induced by a gradient in normal stress, and (3) precipitation on open pore walls or within grain boundaries subjected to a lower normal stress. Strain driven dissolution, where material moves from regions of high dislocation density to regions of low dislocation density, has been cited as an alternative to stress-induced dissolution (Bell et al., 1986; Vernon, 2004; Passchier and Trouw, 2005).

The influence of folding in a single- or multilayered materials on stress and strain distributions, and how these distributions can be coupled to mass transfer, has been investigated numerically by a number of workers (e.g., Durney, 1978; Stephansson, 1974; Hobbs et al., 2000;

Zhang et al., 2000). In these studies, folding of homogeneous layers is considered. However, rocks typically contain two or more minerals with variable geometrical and crystallographic arrangements relative to one another. The elastic interactions of these individual minerals lead to marked heterogeneity in the spatial distributions of stress and strain during deformation (e.g., Tullis et al., 1991; Johnson et al., 2004). Thus, the question arises as to how this grain-scale spatial heterogeneity will influence the larger-scale (e.g., microfold half-wavelength) stress and strain gradients, and therefore the driving forces responsible for mass transfer during crenulation cleavage development. In order to examine grain-scale elastic interactions, we use the finite element method to evaluate instantaneous models containing hundreds of individual quartz and muscovite grains. Each grain is assigned its own crystallographic orientation and material-specific 3D stiffness tensor. The microstructure models are subjected to an elastic shortening strain of 1%. To evaluate how the spatial distributions and intensities of mechanical quantities change with fabric evolution, we consider three different stages of crenulation cleavage development (based on stage 2, 3 and 4 of Bell and Rubenach, 1983; see also Figure 2.2).

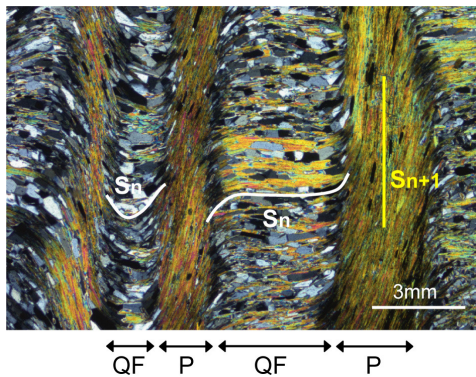


Figure 2.1. Photomicrograph of crenulation cleavage. Indicated are the P- (crenulation limbs) and QF- (crenulation hinges) domains and two generations of foliation, S_n and S_{n+1} . Sample from the Main Central thrust zone, Nepal Himalaya.

Below, we provide some background information on crenulation cleavage and its development. We then give background information and methodologies for our numerical experiments. Finally we discuss the results of our experiments and the implications for crenulation cleavage development. In summary, we find that mean stress and volumetric strain values in quartz grains vary systematically depending on domainal position within the crenulation

cleavage microstructure. The resulting gradients between P- and QF-domains are consistent with a pressure-solution mechanism of fabric formation, but they are also consistent with a formulation that emphasizes volumetric strains as opposed to stresses. The volumetric strain gradients are used as a proxy for how fluids will flow during fabric evolution, providing a quantitative basis for understanding mass transfer during crenulation cleavage development.

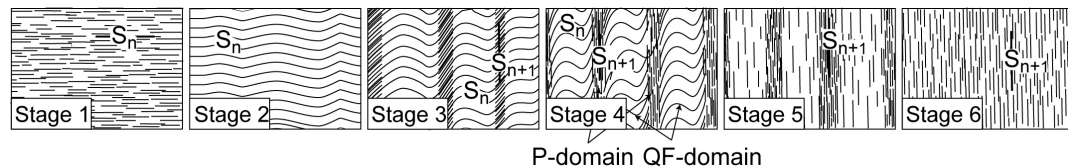


Figure 2.2. Six stages of crenulation cleavage development. At stage 1 the original S_n foliation is present, which becomes crenulated at stage 2. At stage 3 the crenulation process is accompanied by solution/precipitation facilitated metamorphic differentiation. At stage 4 new phyllosilicates begin to grow parallel to S_{n+1} . At stage 5 a spaced cleavage with no relic S_n in the QF-domains is formed that eventually becomes homogenized at stage 6. Modified from Bell and Rubenach (1983).

2.3. Background

2.3.1. General Observations

Crenulation cleavage has been observed and described since the mid-nineteenth century (e.g., Sharpe, 1849; Sorby, 1857, 1880), but it was not until the second half of the twentieth century that workers began to systematically investigate the variables that determine its morphology and microstructure (e.g., Cosgrove, 1976; Gray, 1977a,b). The wide range of crenulation cleavage morphologies can be broadly subdivided into two classes: discrete and zonal crenulation cleavage. Both classes are gradational into one another and can occur together in one crenulated fabric (Gray, 1977a). Discrete crenulation cleavage refers to a crenulated fabric in which there are thin, sharply defined cleavage discontinuities (resembling micro-faults or fractures) that truncate the pre-existing foliation. Zonal crenulation cleavage refers to a fabric in which the boundaries between the domains are gradational (e.g., Figure 2.1). The general morphology of crenulation cleavage, regardless of whether it is discrete or zonal, is determined by the degree of mechanical anisotropy in the pre-existing fabric and the orientation of the fabric

with respect to the maximum principal stress direction (e.g., Cosgrove, 1976; Gray, 1977b; Price and Cosgrove, 1990, p438). Crenulation cleavage folds may be symmetrical (like in our model) or asymmetrical (e.g., Figure 2.1), with the latter being the most common (Hobbs et al., 1976, p 218) owing to the dominance of limbs over hinges in regionally folded rocks.

2.3.2. Previous Modeling

The evolution of macro-, meso- and micro-scale folds, including the distributions of stress and strain within them, has been explored by theoretical (e.g., Biot, 1957, 1961; Ramberg, 1963; Johnson and Fletcher, 1994), analog (e.g., Ramberg, 1963; Means and Rogers, 1964; Means and Williams, 1972; Etheridge, 1973; Abbassi and Mancktelow, 1992) and numerical (e.g., Dieterich and Carter, 1969; Stephansson, 1974; Zhang et al., 2000; Hobbs et al., 2000) models.

In theoretical models, the formation of crenulation cleavage is divided into different stages. First, buckling instabilities are developed in an anisotropic medium, such as mineral fabrics or multi-layered rocks. This is followed by the development of crenulation cleavage planes that are related to the microbuckles and are formed and further developed by a dissolution-precipitation process and mineral redistribution (e.g., Williams, 1972; Cosgrove, 1976; Gray and Durney, 1979). Bell and Rubenach (1983) proposed a six-stage model of crenulation cleavage development based on observations of both matrix and porphyroblast inclusion trails (Figure 2.2). Stage 1 represents the initial homogeneous, planar foliation (S_n), which is gently crenulated in stage 2. At stage 3, solution- and precipitation-facilitated metamorphic differentiation occurs and a new foliation (S_{n+1}) begins to develop. At stage 4 new phyllosilicates grow parallel to S_{n+1} . At stage 5 a spaced cleavage develops in which the original fabric, S_n , is no longer visible. Eventually this spaced cleavage becomes homogenized at stage 6, resulting in a uniform, penetrative S_{n+1} schistosity.

In analog models with synthetic mica and artificial salt-mica schists conjugate shear zones with intervening microfolds that resemble crenulation cleavage structures were created (e.g., Means and Rogers, 1964; Means and Williams, 1972; Etheridge, 1973). In these experiments samples were compressed normal to the foliation to investigate the effects of strain rate, confining pressure and the role of water.

In numerical models single or multiple layers of elastic, viscous, elastic-viscous or elastic-plastic material containing small perturbations are embedded in a less competent matrix and subjected to shortening parallel to the layer(s) to investigate its/their behavior. These numerical models built upon theoretical models from Biot (e.g., Biot, 1957, 1959, 1961, 1964) and Ramberg (e.g., Ramberg, 1960, 1961, 1963) and analog models in which layers of materials like rubber sheets (e.g., Ramberg, 1961, 1963), plasticine (e.g., Cobbold et al., 1971) and wax (e.g., Abbassi and Mancktelow, 1992) were shortened. In multilayered systems asymmetric parasitic folds develop in the limbs, and symmetric folds develop in the hinge of larger scale folds, similar to crenulation cleavage (Frehner and Schmalholz, 2006). The ratio of competency, or viscosity, between the different layers, and the strain rate at which the material is deformed, are important parameters determining the wavelength and periodicity of the folds (e.g., Biot, 1957; Hobbs et al., 2000; Zhang et al., 2000). Within the folded layers, mechanical disequilibria develop in the form of heterogeneous stress and strain distributions, causing free-energy gradients along which materials can diffuse (Stephansson, 1974). These gradients promote movement of material from the limb zones to the hinge zones of the folds and the variations of mean stress found in experimentally formed folds are consistent with variations in mineral composition, bulk chemical composition, and grain size of folds found in nature (e.g., Stephansson 1974). More recent numerical models show a thermal-mechanical feedback, and explore the coupling of deformation to fluid flow and chemical reactions (Hobbs et al., 2008).

2.3.3. Mass Transfer

Whether all of the material that is dissolved in the P-domains is precipitated in the QF-domains, or whether it is partly or entirely removed from the local system, is still a matter of debate. Most geochemical studies suggest that there is little to no volume loss in either low grade slaty cleavage or crenulation cleavage in higher grade rocks (e.g., Mancktelow, 1994; Erslev, 1998; Saha, 1998; McWilliams, 2007). Most microtextural and strain studies, on the other hand, suggest that dissolved material is removed from the system. Based on measurements of strain markers, volume losses of 50% or more are proposed in some slates (e.g., Wright and Henderson, 1992; Goldstein et al., 1995, 1998) and similar amounts have been postulated during the development of crenulation cleavage (Bell et al., 1986). The geochemical studies are based on the assumption that certain elements are immobile, serving as constants when comparing the compositions of different cleavage domains. Phyllosilicates that are not in equilibrium are also a base for assuming crenulation cleavage rocks are not part of a fluid-dominated system, and mass transfer is limited to a local scale (McWilliams et al., 2007). It also remains uncertain how much deformation has occurred in the “undeformed” reference domains used in these studies, adding to the issue of local compositional variations in sedimentary protoliths. The structural studies are based on the assumption that the original shapes and sizes of strain markers are well known. It is not yet clear which type of study – geochemical or structural – provides the more reliable results (e.g., Vernon, 1998; Williams et al., 2001).

2.4. Numerical Modeling

2.4.1. Anisotropic Elasticity

Although elastic anisotropy is considered as a material property in some of the models mentioned in the previous section, grain-to-grain interactions and the redistribution of grains are not; these factors may play an important role in driving mass transfer during crenulation cleavage formation. Gray and Durney (1979) discussed how different fabric-derived factors, namely grain

shape, grain orientation, mineral solubility, grain boundary diffusion kinetics, grain contacts, and microfold wavelengths might affect crenulation cleavage differentiation. Below we investigate the influence of grain shape and orientation on microfolding and, in particular, crenulation cleavage development.

Because most minerals are elastically anisotropic, their shape and orientation influence the way in which they respond to an applied stress. This anisotropic behavior can be described (at low stress levels) with Hooke's law:

$$\sigma_{ij} = C_{ijkl} \varepsilon_{kl}, \quad (2.1)$$

where σ_{ij} is the stress, C_{ijkl} is the 4th rank elasticity tensor, and ε_{kl} is the strain (e.g., Nye, 1957). Assuming a 3D stress state, the elasticity tensor contains 81 elastic coefficients to link the stress tensor with the strain tensor. Each mineral has its own specific elasticity tensor. Due to the symmetry of the stress and strain tensors and the crystal symmetry of the minerals, the number of independent coefficients of the stiffness matrix (or elasticity tensor) can be simplified (Nye, 1957). Therefore, to describe the elasticity of muscovite, a monoclinic mineral, 13 independent elastic constants are needed, and quartz, a trigonal mineral, has 6 independent elastic constants (Figure 2.3).

| Quartz | Muscovite |
|---|--|
| $\begin{pmatrix} 86.6 & 6.7 & 12.6 & -17.8 & 0 & 0 \\ & (86.6) & (12.6) & (17.8) & 0 & 0 \\ & & 106.1 & 0 & 0 & 0 \\ & & & 57.8 & 0 & 0 \\ & & & & (57.8) & (-17.8) \\ & & & & & (39.95) \end{pmatrix}$ | $\begin{pmatrix} 184.3 & 48.3 & 23.8 & 0 & -2 & 0 \\ & 178.4 & 21.7 & 0 & 3.9 & 0 \\ & & 59.1 & 0 & 1.2 & 0 \\ & & & 16.0 & 0 & 0.5 \\ & & & & 17.6 & 0 \\ & & & & & 72.4 \end{pmatrix}$ |

Figure 2.3. Stiffness matrix (Voigt notation) for Quartz and Muscovite in GPa at room temperature and atmospheric pressure. Data obtained from Bass (1995).

Experimental data on the compressibility of minerals show that muscovite is three to four times more compressible along the c-axis than along the a-axis or b-axis (Guidotti et al., 2005). For example, a Na-rich muscovite at room temperature and ~3.5 GPa will compress 3.59% along its c-axis and only 0.83% and 1.05% along its a-axis and b-axis, respectively (Comodi and

Zanazzi, 1995). These numbers are sensitive to both temperature and composition. For quartz this difference is less pronounced: at the same conditions an α -quartz crystal will shorten 2.75% along its a-axes and 1.88% along its c-axis (Angel et al., 1997).

2.4.2. Method

In this study, the elastic interactions between individual muscovite and quartz grains and the influence of these interactions on stress and strain distributions within a rock are investigated by considering the crystallographic orientations and anisotropic elasticity of the individual grains. Simplified geometries, containing only quartz and muscovite grains, were created to represent three different stages of crenulation cleavage development (Figure 2.4; based on stages 2- 4 of Bell and Rubenach, 1983). The modal abundance of the two minerals is kept constant from stage to stage, implying that no material is lost during development. Although we have results for both symmetric and asymmetric crenulation cleavage, the results are similar so we only discuss the symmetric example.

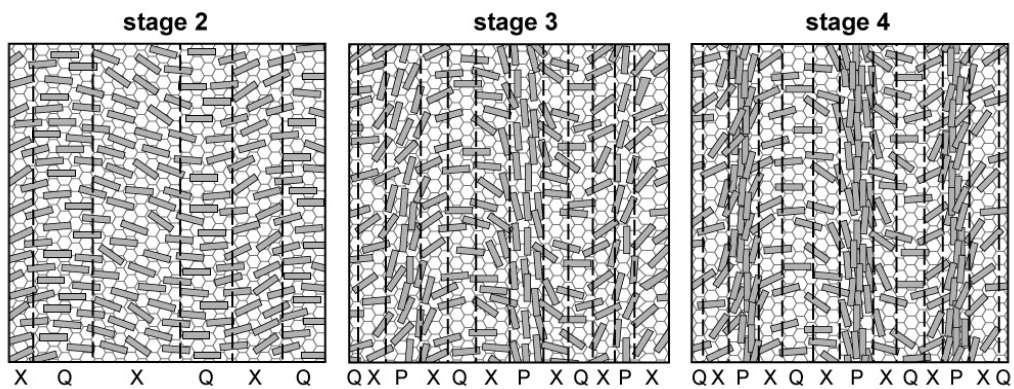


Figure 2.4. Model setup. The grey rectangles represent muscovite grains and the grey lines outline the quartz grains. The c-axes of the muscovite grains are oriented perpendicular to the long axis of the grain and are parallel to the plane of the paper. The quartz grains are oriented differently in different models: they are oriented randomly (model III), with the c-axes perpendicular to the plane of the paper (model I), or with the c-axes parallel to the shortening direction (model II). The dashed lines outline the structural domains P, X and Q.

OOF2 is a two-dimensional, object oriented finite element code developed by the National Institute of Standards and Technology (Langer et al., 2008; <http://www.ctcms.nist.gov/oof/oof2/>). The code uses image segmentation to divide an image into distinct sets of pixels that correspond to a homogeneous part of the image, i.e. the different grains (Reid et al., 2008). The different “pixel groups” are given their own material properties. In all models the muscovite grains are oriented with the c-axes parallel to the plane of the paper and perpendicular to the long dimension of the grain. Three variations of each of the three modeled stages are evaluated in order to examine the role of quartz-grain orientations on the solutions. In model I all quartz grains have the same orientation, with the c-axis (its least compliant axis) perpendicular to the plane of the paper. In model II all quartz grains have the same orientation, with the c-axis parallel to the shortening direction. In model III all the quartz grains have a random orientation. After defining the microstructure, a skeleton and mesh, composed of rectangular and triangular elements, are created (Figure 2.5) using an auto-meshing option that automatically refines a skeleton until it fits the microstructure following a predefined set of operations that are described in Langer et al. (2008) and Reid et al. (2008). Models I and II consist of at least 10000 elements and the models with the randomly oriented quartz consist of at least 16000 elements. Once the mesh is defined, the models are subjected to 1% horizontal shortening. The upper and lower boundaries are defined as free surfaces (Figure 2.5). Results are calculated in plane-strain, and values for mean stress and volumetric strain in response to the applied displacement at the boundaries are calculated and plotted.

For data analyses the model is divided into three different structural domains based on the orientations of the muscovite grains: P-, Q-, and X-domains (Figure 2.4). In the P-domains, the long dimension of the muscovite grains are all oriented close to vertical and perpendicular to the shortening direction as is consistent with the P-domains in natural examples. In the Q-domains, all muscovite grains are oriented sub-horizontally, parallel to the shortening direction. In the X-domains, the long dimension of the muscovite grains are all oriented at an angle with respect to

the shortening direction. The Q- and X-domains combined are equivalent to the QF-domains in natural examples.

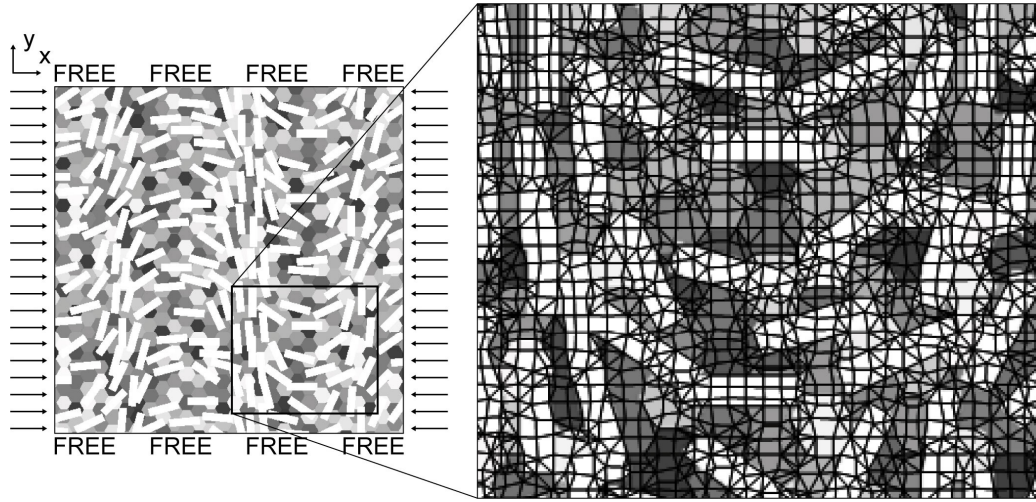


Figure 2.5. Boundary conditions. Each model is subjected to a horizontal shortening of 1%, the upper and lower boundaries are defined as free surfaces. The blowup image shows the mesh generated by OOF2.

2.4.3. Model Results

2.4.3.1. Maps. Figure 2.6 shows maps of the mean stress and the volumetric strain for the three stages of crenulation cleavage development, each subjected to a 1% horizontal shortening. This figure only shows the results for the model in which quartz grains are randomly oriented (model III); the effect of quartz orientation (the results of models I and II) will be discussed in section 2.5.1. The muscovite grains in the Q- and P- domains show the most dramatic response to the deformation. In all stages, the muscovite grains in the Q-domain accommodate the highest compressive stresses and the lowest negative volumetric strains. The muscovite grains in this domain are oriented with their least compliant axis (the c-axis) perpendicular to the shortening direction. In stage 3 and 4 the muscovite grains appear to act as stress beams, protecting the quartz grains from deformation in the Q-domains resulting in lower average mean stress and volumetric strain in quartz grains than in the P-domains. The highest negative volumetric strains are accommodated

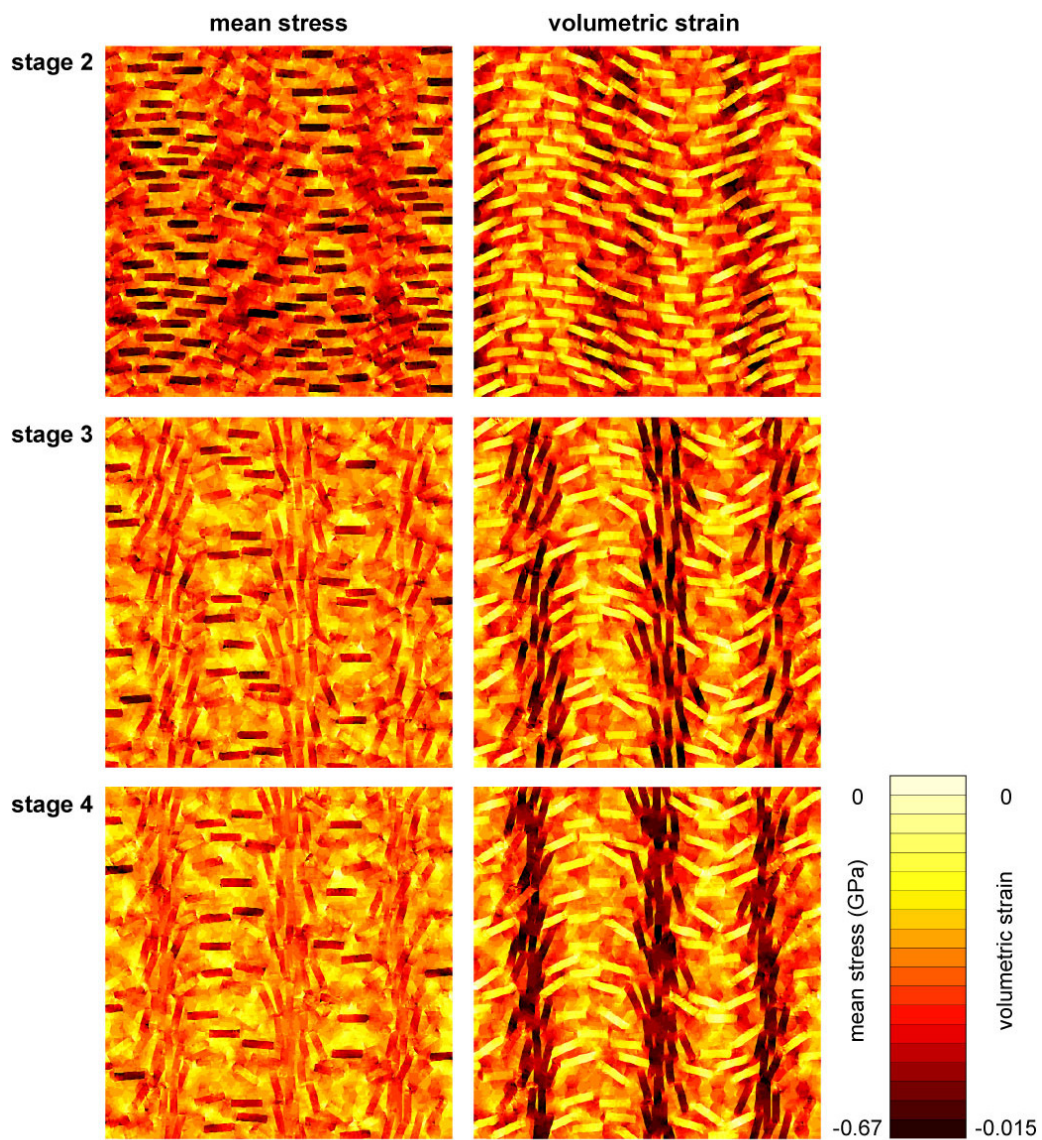


Figure 2.6. Contour maps of the mean stress and volumetric strain for the three different stages of the model with the randomly oriented quartz grains (model III). Negative stress is compressional.

by the micas in the P-domains where the muscovite grains are oriented with their least compliant axis parallel to the shortening direction. The micas in the X-domains accommodate mean stresses intermediate between those in the P- and Q-domains and similar to the amounts accommodated by the quartz grains; these micas also accommodate low negative volumetric strains. Although the interaction among differently oriented quartz grains leads to local heterogeneity, domain-scale differences in mean stress and volumetric strain are established with higher values in the P-domains than in the X- and Q-domains. The magnitude of these gradients will be discussed in the next (statistical analysis) section.

Mass transfer during crenulation cleavage development may be primarily driven by pore fluid pressure gradients, which we can approximate using gradients in the calculated volumetric strain field (e.g., Cox and Etheridge, 1989; Koons et al., 1998). To illustrate the general pattern of fluid flow, Figure 2.7 shows a vector plot in which arrows are oriented down gradient, parallel to the local maximum gradient in volumetric strain. Although interaction among the different grains influences the direction of flow and complicates the local flow pattern, the domain-scale gradients in volumetric strain noted above lead to bulk flow from the P- and X- domains into the Q-domains. In natural examples, pathways for fluid flow would follow grain boundaries and possibly intragranular fractures. Thus, a more precise calculation of fluid flux would need to consider the geometry of these pathways (e.g., Carlson and Gordon, 2004; Joesten, 1991), but would not change our general result.

2.4.3.2. Statistical Analysis of the Data. In order to quantify the mean stresses and volumetric strains, average values and their standard deviations are calculated and plotted for quartz grains within the 3 structural domains (Figure 2.8). The average values are calculated for only the quartz grains because quartz is the principle material that is dissolved, transferred, and precipitated. When comparing the models with the different orientations of quartz, model I accommodates the lowest mean stresses and highest negative volumetric strains, model II accommodates the highest mean stresses and lowest negative volumetric strains, and the model

with the randomly-oriented quartz grains (model III) shows intermediate values for mean stress and volumetric strain with respect to the other two models.

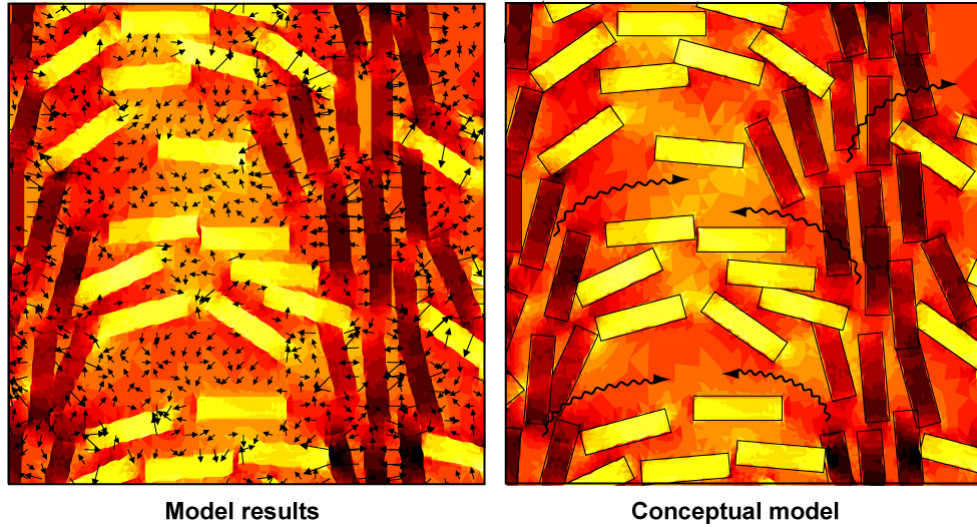


Figure 2.7. Detail of the volumetric strain map from stage 3, model I. The arrows in the left image indicate mass transfer within the quartz (arrows originating in muscovite grains were removed from this flow chart). The origin of each arrow is the point of measurement. Arrows point toward the low negative volumetric strain regions. The length of the arrow indicates the magnitude of the gradient (short is a small gradient, long is a large gradient). The image on the right schematically shows the bulk flow from the P-domains to the QF-domains. Coloring is the same as in Figure 2.6.

The skewness and kurtosis are calculated and plotted to give a measure of the variance of the datasets (Figure 2.9). The datasets for the mean stress are slightly negatively skewed and have the highest kurtosis in the Q-domains. The skewness for the datasets of the volumetric strain differs from domain to domain: it is negative in the P-domains and positive or less negative in the other domains. The kurtosis for the data of the volumetric strain shows a slightly similar pattern as that of the kurtosis of the mean stress, with higher values of kurtosis in the Q-domains with respect to the other domains.

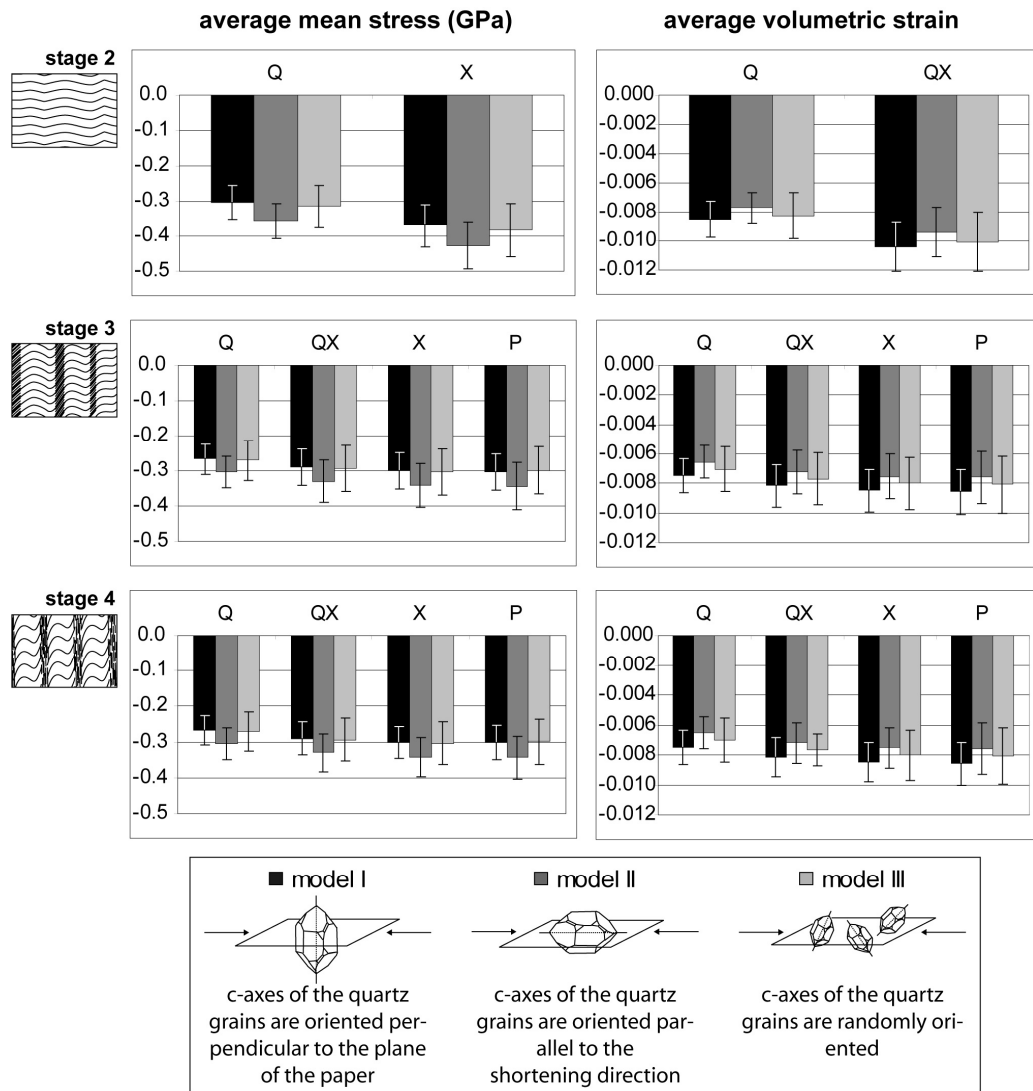


Figure 2.8. Average mean stress and average volumetric strain in the quartz grains per structural domain. The bars represent plus and minus 1 standard deviation. For each domain the results for model III fall in between the results for models I and II. The values for the average mean stress and average volumetric strain are the lowest in the Q-domain at each stage.

To give a better indication of the relative differences in mean stress and volumetric strain among the different domains the average values that are plotted in Figure 2.8 are normalized against the average values in the Q-domains for each separate model. The greatest gradients (between the Q- and X-domains at stage 2, and between the Q- and X-domains at stages 3 and 4) are plotted in Figure 2.10 and are largest at stage 2 for both the mean stress and the volumetric strain.

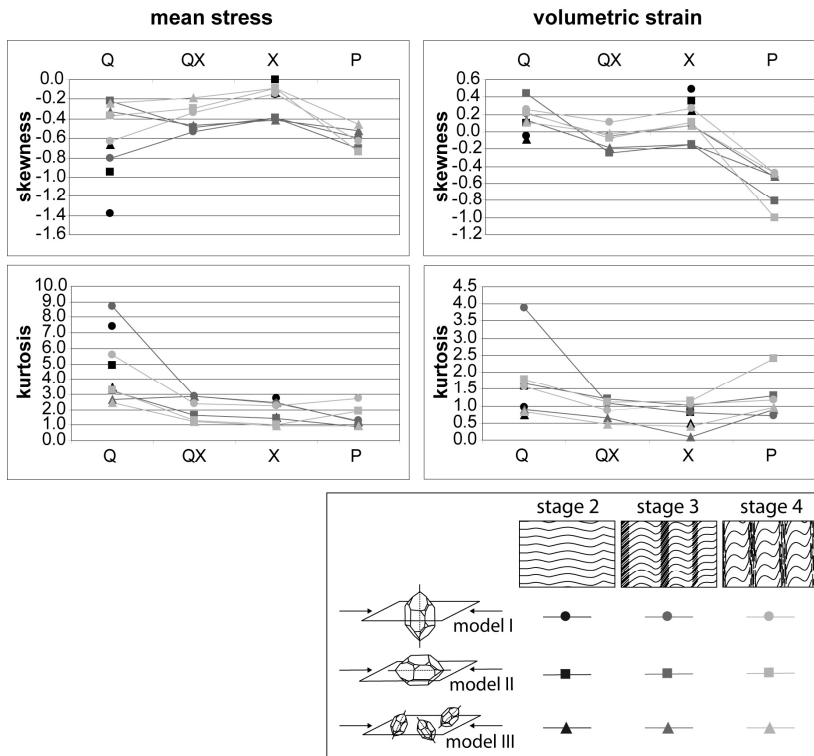


Figure 2.9. Skewness and kurtosis of the mean stress and volumetric strain datasets. The mean stress data have negative skewness and a higher value of kurtosis in the Q-domains with respect to the kurtosis in the other domains. The volumetric strain data shift from a negative skewness in the P-domains to a less negative or positive skewness in the Q-domains. The volumetric strain data also show a peak of kurtosis in the Q-domains.

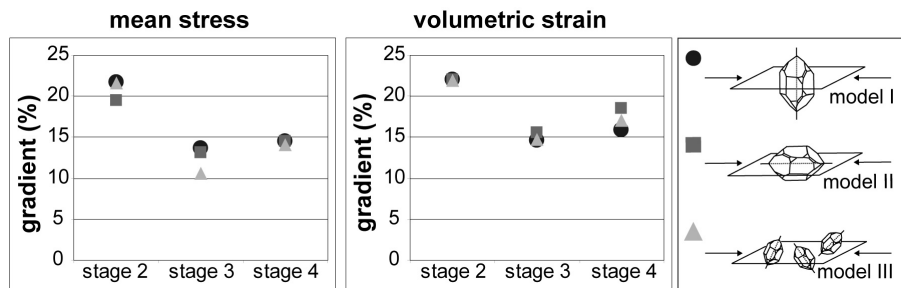


Figure 2.10. Gradients between Q- and X- (stage 2) or P- (stage 3 and 4) domains in %. The gradient decreases from the early stage 2 to the intermediate stage 3 of crenulation cleavage development. At stage 4 the gradient increases slightly.

2.5. Discussion

2.5.1. Model Results

A polymineralic approach has been used to model the incremental mean stress and volumetric strain distributions at three stages of crenulation cleavage development. We used finite element models composed of quartz and muscovite grains. The muscovite grains are all oriented with the c-axes parallel to the plane of the paper and perpendicular to the long dimension of the grain. A distinction is made between three models based on the orientation of the quartz grains in the model: in models I and II the quartz grains all have the same orientation, with the c-axis perpendicular to the plane of the paper, or parallel to the shortening direction (model I and model II respectively); in model III the quartz grains have a random orientation. Below we evaluate the influence of the orientation of the quartz grains, how the results differ from domain to domain and from stage to stage, and the distribution of the data.

2.5.1.1. Influence of the Orientation of the Quartz Grains. The results show that there are no large differences between the three models (I, II and III) arising from the variation in quartz orientation (Figure 2.8), confirming that the orientation and modal abundance of the muscovite grains plays the most important role in forming the overall stress and strain distributions in the developing crenulation cleavage fabric. The model containing randomly oriented quartz grains (model III) gives intermediate results for mean stress and volumetric strain. This is expected since the orientations of the quartz grains in the other two models represent the least compliant and one of the most compliant possible orientations for the quartz grains, relative to the applied shortening direction. In model III the quartz grains interact with one another creating a more heterogeneous pattern of stress and strain distribution, but the local high and low values appear to cancel each other out when calculating an average value per domain. Because the orientation of the quartz grains appears to play only a minor role in how mean stresses and volumetric strains are distributed, the results from model III will be used in the remainder of our discussion below.

2.5.1.2. Comparison of Different Domains and Stages. Muscovite is elastically highly anisotropic, being more compressible along its c-axis and less compressible along its a-axis and b-axis than along any direction in quartz. In the P-domains, where the phyllosilicates are mainly oriented with their most compressible axis (sub-) parallel to the shortening direction, the quartz will always be the stiffest material. Thus, quartz in any orientation will carry higher mean stresses than the muscovite. In the Q-domains, where the phyllosilicates are oriented with their least compressible axes (sub-) parallel to the shortening direction, they are stiffer than quartz grains in any orientation, and will therefore carry higher mean stresses. In the X-domains an intermediate situation develops. The strong anisotropy of muscovite leads to less volumetric strain accumulation in quartz grains in the Q-domains compared to the quartz grains in the P-domains. Thus, we conclude that the systematic variation in muscovite orientation from P- to Q-domains causes the mean stress and volumetric strain gradients in quartz between these domains.

In all stages of crenulation cleavage development the mean stresses and volumetric strains are highest in the quartz grains in the P-domains (X-domains in stage 2) and lowest in the quartz grains in the Q-domains. The average values between those domains differ by up to 22% for both the mean stress and the volumetric strain and they decrease with fabric evolution (Figure 2.10). At stage 2, P-domains have not yet developed, so more volumetric strain is accommodated in the quartz grains in the X-domains because there are no muscovite grains with their c-axes near-parallel to the shortening direction. As the fabric develops, muscovite grains rotate and recrystallize into more favorable orientations for strain in the P-domains, reducing the gradients at stage 3 relative to stage 2. At stage 4 there is modally less quartz in the P-domains and more quartz in the QX-domains than there is at stage 3, causing a slight increase in the gradients from stage 3 to stage 4.

2.5.1.3. Skewness and Kurtosis of the Data. The distributions (skewness and kurtosis) of the mean stress data show that most data points within the quartz in the different domains tend to have a low negative value (negative skewness) and less spread (peak of kurtosis) in the Q-

domains than in the other domains. The latter pattern is due to the geometry of the Q-domains, which contain relatively more quartz than muscovite grains. Because there are fewer interactions between the two minerals this leads to a more homogeneous mean stress in the quartz. A similar pattern in kurtosis, although less pronounced, is found in the distributions of the volumetric strain data. The interactions between the individual quartz grains, causing heterogeneity in the stress and strain distributions, cause a shift from negative skewness in volumetric strain distribution in the P-domains to a positive or less negative skewness in the Q- and X-domains. The orientations of the muscovite grains have an important effect on the skewness: volumetric strains in the quartz grains tend to be on the higher (less negative) side if the phyllosilicates are oriented with their most compliant axis parallel to the shortening direction, and on the lower (more negative side) if the phyllosilicates are oriented with their most compliant axis perpendicular to the shortening direction.

2.5.2. Implications for Crenulation Cleavage Development

The model results presented in this paper are based on instantaneous elastic interactions among quartz and muscovite grains at three different stages of crenulation cleavage development. No initial confining stresses are applied, and we do not consider time- and strain-dependent evolutionary processes such as grain boundary migration and dislocation creep, chemical reactions, and grain boundary diffusion and advection. Nevertheless, our results facilitate analysis of the stresses and strains that arise from elastic interactions of a polymineralic continuum, providing important constraints on the local and bulk stress and strain gradients that play a large role in establishing the characteristic mineralogical segregation associated with crenulation cleavage development.

The overall pattern of relatively high mean stresses in the quartz grains in the P-domains compared to those in the Q-domains is consistent with results derived from models in which homogeneous layers are folded (see section 2.4.1). These folding models show the development

of gradients in mean and normal stress between fold limbs and fold hinges, similar to those found in our results between P-domains and Q-domains in crenulation cleavage. Pressure solution has commonly been invoked in these folding models to relate the gradients in mean/normal stress to the transfer of quartz from the fold limbs to the fold hinges, not only in macro-scale folds, but also in smaller scale crenulations. Similarly, Cosgrove (1976) suggested that the high stresses in the muscovite minerals in the QF-domains relative to the P-domains of crenulation cleavage should lead to the opposite, with dissolution of phyllosilicates in the QF-domains and their precipitation in the P-domains.

The role of pressure in the dissolution of quartz has been questioned (e.g., Bjørkum, 1996; Meyer et al., 2006). Field observations (e.g., Weyl, 1959; Houseknecht, 1988) and experimental work (e.g., Rutter and Wanten, 2000; Anzalone et al., 2006; Meyer et al., 2006) indicate that the presence of phyllosilicates enhance the dissolution of quartz. Bjørkum (1996) found very thin layers of mica or illite between two quartz grains and hypothesized that these thin layers could be missed, leading to a mistaken interpretation of pressure solution between two adjoining quartz grains (Bjørkum, 1996; Oelkers et al., 1996). Meyer et al. (2006) showed experimentally that dissolution of quartz is enhanced if in contact with muscovite in wet conditions (not under dry conditions) but slows down after time, possibly because of the reprecipitation of dissolved quartz outside the contact junction. Experimental data from Niemeijer and Spiers (2002) on the other hand showed no acceleration of compaction rates of quartz if muscovite was added. They postulated that dissolved Al^{3+} is responsible for decrease in solubility, dissolution rates, and precipitation rates of quartz. So, even though field data imply that the dissolution of quartz is enhanced by the presence of phyllosilicates, experimental data are still inconclusive and more investigations are required to evaluate the physics and chemistry of this process.

Experiments on quartz (Green, 1972; Hobbs, 1968), halite (Sprunt and Nur, 1977; Bosworth, 1981), and plagioclase (Kramer and Seifert, 1991) have shown that when these

minerals are sufficiently strained, their solubility is enhanced due to an increase of dislocation density. Although Hirth and Tullis (1994) found similar results to Green (1972) for deformed quartz, they postulate that it is stress, and not the presence of a high dislocation density within the quartz, that causes the transition from α quartz to coesite. Bell et al. (1986) suggested that minerals like quartz and feldspars adjacent to phyllosilicates in rocks with crenulation cleavage, or metapelitic rocks in general, will be affected on their boundaries by shearing, increasing the dislocation energy, and enhancing the dissolution of those minerals. In this model, shear strain is accommodated by glide on the (001) planes in the phyllosilicates, whereas the quartz is plastically strained against the phyllosilicates on a variety of slip systems, generating a dislocation density gradient and eventually dissolves where the dislocation density is highest. However, the general lack of evidence for dislocation creep in quartz during crenulation cleavage development (Vernon and Clarke, 2008 and references therein) is difficult to reconcile with this model. Wintsch and Dunning (1985) calculated the energy stored in dislocations in quartz as a function of dislocation density and the effect of this increased energy on the activity of strained quartz and its solubility in pure H₂O. They found that the resulting increase in free energy is probably too small to play a significant geochemical role in rock deformation and hypothesized that where fluid/rock ratios are low, the aqueous activity of quartz might be significantly increased by the dissolution of quartz containing dislocation tangles, establishing a chemical potential gradient of SiO₂ and thus driving diffusive mass transfer, which is consistent with the results found in the experiments.

Figure 2.11 shows a schematic diagram of fluid flow during crenulation cleavage formation, based on models from Bell and Hayward (1991) and Worley et al. (1997). Bell and Cuff (1989) argued that the anastomosing geometry of foliation generates areas of compression and tension, driving fluids towards localities of dilatation that are accommodated by microfracturing. These dilatational sites are formed preferentially in the extensional regions (QF-domains), and are proposed to be the nucleation sites for porphyroblasts. Worley et al. (1997)

focused on the formation of discrete crenulation cleavage developed in chlorite- to garnet-zone schists. In order to explain the differences in mineralogy that they found in the different structural domains, they suggested that at early stages and chlorite zone conditions a zonal crenulation cleavage initially developed in response to microfolding and diffusive mass transfer at a local scale (less than half the wavelength of the crenulations). With progressive deformation a discrete crenulation cleavage evolved and these workers suggested that large-scale, buoyancy driven, advective flow occurred along the P-domains, in addition to grain-boundary diffusion on a smaller scale.

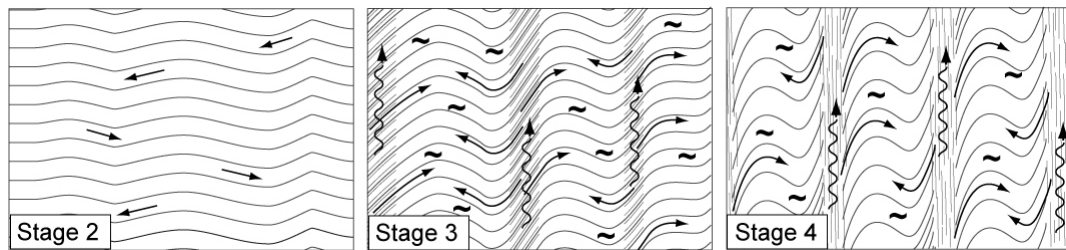


Figure 2.11. Schematic diagram of fluid flow at stages 2, 3 and 4 of crenulation cleavage development based on models of Bell and Hayward (1991) and Worley et al. (1997). The arrows indicate fluid flow from P- to QF-domains, the wavy-arrows indicate fluid flow within the P-domains and the ~ indicate microfractures in the quartz.

A number of workers have investigated the role of metamorphic reactions during crenulation cleavage development (e.g., Marlow and Etheridge, 1977; Worley et al., 1997; Williams et al., 2001). They found that muscovite changes its composition in the P-domains and that plagioclase changes its composition in both the P- and QF-domains during foliation formation. This indicates that metamorphic reactions play an important role during fabric development. It was implied that stress variations are not well assessed on the grain-size scale (Marlow and Etheridge, 1977) or are too small to drive dissolution and transportation of material, especially at elevated metamorphic grades (Williams et al., 2001). Both Marlow and Etheridge (1977) and Williams et al. (2001) suggested that metamorphic reactions are an important driving

force for dissolution and that volumetric strain heterogeneities, determined by the microstructure of the fabric, might drive the mass transfer.

Our modeling results allow an evaluation of mineral-scale stress and strain heterogeneities and show that bulk flow driven by fluid pressure gradients will transfer soluble material from the P-domains into the QF-domains (Figure 2.7). Because we do not consider mechanisms for viscous dissipation of elastic strain energy, the absolute values we obtained are not realistic for natural rocks. However, the relative values of stress and strain among the different domains are probably less susceptible to time-dependent decay and may be representative of natural conditions. Even though we do not find areas of dilatation in our models, the gradients in negative volumetric strain between the different structural domains (up to 22%) are probably sufficient to drive mass transfer, assuming that fluids are present and that pathways are available for fluid flow. Our results therefore support the suggestions of previous studies in which volumetric strain is considered to be important in mass transfer associated with crenulation cleavage. A model in which quartz is lost from the system (the modal abundance of quartz will decrease in the P-domains, but remain constant in the Q-domains) will generate different results from our isovolumetric model, but our general results pertaining to gradients in stresses and strains should still apply. Future work should examine time dependent evolution of crenulation cleavage in which crystal plasticity (processes such as grain boundary migration and dislocation creep), chemical reactions, and diffusion and advection coupled to grain boundary structures are considered.

Given the observations made by us and others, and the model results presented here, we suggest that the most reasonable model for crenulation cleavage development is one in which metamorphic reactions drive the dissolution of material and variations in volumetric strain are largely responsible for transport of components from the P- to the QF-domains. This bulk transport is responsible for the characteristic mineralogical differentiation of crenulation cleavage. At the grain-scale, our model shows that there are large variations in mean stress and

volumetric strain at grain interfaces, which are primarily controlled by the orientation of the phyllosilicate grains. These local variations may identify favorable sites for metamorphic reactions to initiate (de Ronde and Stünitz, 2007), but may also aid local diffusion and advection (Rutter, 1983; Etheridge and Hobbs, 1974).

2.6. Summary and Conclusions

We used finite element techniques to evaluate the elastic stress and strain distributions at three instantaneous stages of crenulation cleavage development. Each model comprises hundreds of quartz and muscovite grains, and each grain was assigned its own 3D stiffness tensor and orientation. Each stage was subjected to a shortening of 1%. Our main findings are as follows.

- (1) The orientation and distribution of muscovite grains are the primary factors determining how stress and strain are distributed within developing crenulation cleavage fabric. The orientations of the quartz grains are also important, but they play a subordinate role due to the extreme elastic anisotropy of the muscovite.
- (2) Elastic mismatches between muscovite and quartz grains cause large variations in mean stress and volumetric strain intensity and distribution. Owing to the different orientations of muscovite grains in the different domains, crenulation-scale gradients are established with relatively high values of stress and volumetric strain on quartz grains in the P-domains and relatively low values on quartz grains in QF-domains. These gradients decrease as the fabric evolves into a fully developed crenulation cleavage.
- (3) Although we cannot rule out either the pressure solution model or the strain-driven dissolution model, the evidence for metamorphic reactions in most crenulated rocks combined with our results support a model in which metamorphic reactions drive dissolution of material in the P-domains, and transportation to the QF-domains is driven by fluid-pressure gradients that follow gradients in volumetric strain.

Chapter 3

THE INFLUENCE OF MICROSTRUCTURE ON SEISMIC WAVE SPEED ANISOTROPY IN THE CRUST: COMPUTATIONAL ANALYSIS OF QUARTZ-MUSCOVITE ROCKS*

3.1. Chapter Abstract

We study the influence of microstructural variables on seismic wave speed anisotropy in crustal rocks. The bulk elastic properties and corresponding wave velocities are calculated for synthetic rock samples with varying amounts of muscovite and quartz, different muscovite and quartz grain orientations and varying spatial distributions of the muscovite grains to investigate the sensitivity of seismic wave speed anisotropy on these characteristics. The asymptotic expansion homogenization method combined with finite element modeling is used to calculate bulk stiffness tensors for representative rock volumes and the wave velocities are obtained from these tensors using the Christoffel equation. The aim of this paper is to 1) demonstrate how wave speeds computed from the rigorous asymptotic expansion homogenization method compare with those generated using stiffness tensors derived from commonly applied analytic estimates, and 2) explore how different microstructural variables influence seismic wave speeds.

Our results show that the muscovite grain orientations have a significant influence on the wave speeds. Increasing the modal fraction and alignment of muscovite grains leads to greater seismic anisotropy of the rock. The P-wave speed at an incidence angle of 45° between the foliation and seismic wave path is dependent on all tested microstructural variables, with the orientation distribution of muscovite grains having the largest effect. This so-called P45 effect is an important measure of wave-speed anisotropy and here we provide the first analysis of its

* *The content of this chapter is accepted for publication: Naus-Thijssen et al., Geophysical Journal International, in press.*

sensitivity to microstructural variables. Although we have explicitly considered only muscovite grains in this study, the methodology and observations are expected to apply in general to other phyllosilicates.

3.2. Introduction

The distribution and spatial orientations of elastic anisotropy in Earth's crust and mantle carry valuable information about gradients in thermal, mechanical and kinematic parameters arising from mantle-crust coupling and tectonic plate interactions (e.g., Silver, 1996; Karato, 2008). Causes for seismic anisotropy are 1) the presence of aligned fractures or cracks in the upper 10-15km of the crust (e.g., Crampin, 1981; Kaneshima et al., 1988), 2) the layering of isotropic material (e.g., Backus, 1962), and 3) the development of mineral lattice- and shape-preferred orientations (LPO and SPO respectively) during progressive accumulation of strain (e.g., Mainprice and Nicolas, 1989; Mainprice, 2007). Measurements of shear-wave splitting in global tomographic studies are commonly attributed to anisotropy in the mantle (e.g., Silver, 1996; Savage, 1999). Mantle anisotropy is considered to reflect the development of LPO in anisotropic olivine grains as a function of mantle kinematics (e.g., Karato, 1987; Nicolas and Christensen, 1987; Silver, 1996; Savage, 1999; Mainprice et al., 2000; Tommasi et al., 2000; Montagner and Guillot, 2002; Mainprice, 2007; Karato et al., 2008).

Crustal anisotropy can affect the shear wave splitting values caused by mantle structures. In order to do so the degree of crustal anisotropy must be significant and appropriately oriented (e.g., Okaya et al., 1995; Godfrey et al., 2000). Seismic anisotropy in the continental crust has been observed in numerous seismological studies, and many workers seek to relate the observed seismic anisotropy to crustal deformation and metamorphism (e.g., Okaya et al., 1995; Weiss et al., 1999; Godfrey et al., 2000; Okaya and Christensen, 2002; Okaya and McEvelly, 2003; Vergne et al., 2003; Ozacar and Zandt, 2004; Shapiro et al., 2004; Sherrington et al., 2004; Lloyd and

Kendall, 2005; Champion et al., 2006; Mahan, 2006; Mainprice, 2007; Xu et al., 2007; Lloyd et al., 2009; Readman et al., 2009).

Petrophysically determined data are commonly used to interpret velocity structures, and numerous velocity measurements have been made for rocks that form important constituents of Earth's crust and upper mantle (e.g., Birch, 1960, 1961; Simmons, 1964; Christensen, 1965, 1966; Ji et al., 2002). Another method for calculating bulk properties of polycrystalline rocks requires the measurement of crystallographic orientations of minerals in a polished thin section. Whereas earlier workers made crystallographic measurements using optical or x-ray techniques, Electron Backscatter Diffraction (EBSD) techniques are rapidly growing in popularity (e.g., Mauler et al., 2000; Bascou et al., 2001; Lloyd and Kendall, 2005; Valcke et al., 2006; Lloyd et al., 2009). Once the crystallographic data for a sample are processed, a variety of methods can be used to calculate a bulk elastic tensor, the most common and straight forward of which are the Voigt and Reuss bounds (e.g., Mainprice and Humbert, 1994). Several means of these two bounds have been proposed, including the arithmetic mean or Voigt-Reuss-Hill (VRH) average (Hill, 1952), the geometric mean (Matthies and Humbert, 1993) and generalized mean (Ji et al., 2004). These analytical means are often close to experimentally derived values, but the disadvantage of using them is that they do not explicitly account for grain shapes, grain distributions or grain to grain interactions, and as such have no real physical justification. In addition to the analytical methods described above, several rigorous theoretical methods have been proposed that take into consideration the elastic interaction of the individual grains with the background medium, including the self-consistent (e.g., Hill, 1965; Willis 1977; Mainprice 1997) and differential effective medium (e.g., Bruner, 1976) methods. Mainprice and Humbert (1994) have demonstrated that the self-consistent model yields wave speeds that are virtually identical to those obtained using the geometric mean. The theoretical methods are generally considered to be computationally too involved for practical application (Mainprice, 2007), and the VRH average is mostly used in the Earth sciences' literature to calculate the effective elastic properties of rock

aggregates (e.g., Valcke et al., 2006; Lloyd and Kendall, 2005; Tatham et al., 2008; Lloyd et al., 2009).

In this paper we present a method that accounts not only for the modal fraction of the constituent minerals and their individual crystallographic orientations (texture of the microstructure), but also the spatial arrangement of the grains (stereology of the microstructure). Bunge et al. (2000) estimated that the stereological parameters may contribute up to 25% of the maximum texture influence. The numerical method we present in Section 3.3.2 is based on asymptotic expansion homogenization (AEH) and finite element (FE) analysis for the computation of the bulk stiffness for polymineralic rocks.

Section 3.3 first provide background information on the determination of homogenized elastic constants of rock microstructures via common analytic estimates and bounds. This is followed by a review of the more rigorous AEH method and its FE implementation. A more extensive review of this method can be found in Section 3.7. We also give background information on the determination of the three wave speed velocities in an unbounded rock media given a propagation direction, and describe the measures of seismic anisotropy. Section 3.4 provides details of how the synthetic microstructures were created. Section 3.5 compares wave speeds calculated from the analytic- and AEH-derived stiffnesses and presents the findings from a quartz-muscovite rock parametric study. Microstructural characteristics that can contribute to the bulk elastic properties of a polymineralic rock are 1) the modal abundances, 2) the crystallographic and geometric orientations, 3) the spatial arrangements, and 4) the shapes of its constituent minerals. Because natural rock samples show considerable variability in these characteristics we will assess their influence on elastic rock properties and seismic wave velocities by systematically varying 1) the modal abundance, 2) crystallographic orientation and 3) spatial distribution of a simplified, computer generated, synthetic microstructure containing only quartz and muscovite grains. The bulk stiffness tensor is computed from the generated rock microstructure, which then is used to calculate seismic wave velocities and measures of seismic

anisotropy such as P-delay, shear wave splitting, percentage anisotropy of the P- and S-waves and the normalized P-wave velocity in the diagonal (45°) direction.

3.3. Background

We consider polycrystalline rocks consisting of quartz and mica grains with a simplified microstructure, similar to that depicted in Figures 3.1b and 3.1c. Each location within the microstructure has a phase and orientation description, so that a microstructure is created in which each mineral has its own, single crystal, stiffness tensor relative to its principal crystallographic axes that is transformed to a common sample frame using the Bond matrix (Bond, 1943).

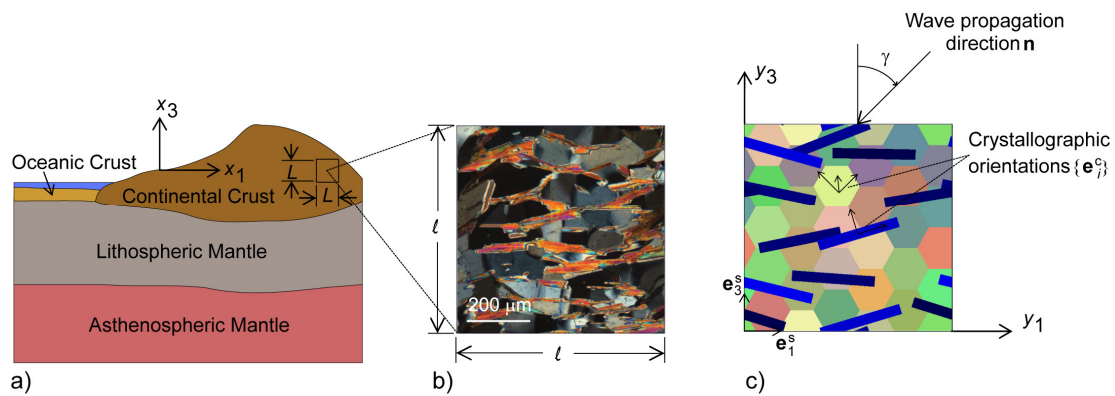


Figure 3.1. Correlation between the large scale structure and the microstructure. (a) Schematic of large scale structure and relation between macro-scale L and micro-scale l . (b) Photomicrograph of a quartz-muscovite schist in cross-polarized light. The grey grains are quartz and the bright colored grains are muscovite grains. (c) Representative synthetic quartz-muscovite microstructure. γ is the incidence angle, \mathbf{e}_i^S and \mathbf{e}_i^C indicate the reference orientations for the sample and crystal respectively. The macro-scale is being analyzed using x coordinates and the micro-scale is analyzed using y coordinates.

3.3.1. Analytic Bounds and Estimates

In treating the bulk elastic properties of heterogeneous materials, the general goal is to compute an effective or bulk elastic stiffness tensor that relates the average strains to the average stresses in the material. Several averaging schemes have been proposed for polycrystalline aggregates, the best known being the Voigt and Reuss methods (Voigt, 1928; Reuss, 1929). The Voigt method assumes that the strains are the same amongst all grains in the aggregate, and the stresses in each grain are obtained using Hooke's law for an anisotropic material. The Voigt average stiffness tensor \mathbf{C}^V , which relates the average stresses to the average strains, can be expressed in integral form as

$$\mathbf{C}^V = \frac{1}{|\mathbf{Y}|} \int_{\mathbf{Y}} \mathbf{C} d\mathbf{Y}, \quad (3.1)$$

where \mathbf{C} is the spatially varying stiffness tensor in the sample coordinate frame and $|\mathbf{Y}|$ is the volume or area of the microstructural domain over which the integration is performed. Conversely, the Reuss bound \mathbf{C}^R assumes that the stress is constant throughout the entire microstructural domain and averages the compliances

$$\mathbf{C}^R = \left(\frac{1}{|\mathbf{Y}|} \int_{\mathbf{Y}} \mathbf{S} d\mathbf{Y} \right)^{-1}, \quad (3.2)$$

where $\mathbf{S} = (\mathbf{C})^{-1}$ is the spatially varying compliance tensor in the sample frame. The Voigt and Reuss estimates represent the respective upper and lower bounds of the effective elastic stiffnesses (Mainprice and Humbert, 1994; Bunge et al., 2000). Mainprice and Humbert (1994) showed that the difference between the bounds increases with increasing anisotropy. Various averages that lie between the two bounds have been proposed. Hill (1952) observed that the arithmetic mean of the two bounds, which is computed as the average of \mathbf{C}^V and \mathbf{C}^R , commonly gives values close to experimental results. Despite the lack of a physical justification, this arithmetic mean, or Voigt-Reuss-Hill average, is still considered to be a useful estimate (e.g.

Mainprice and Humbert, 1994). The geometric mean (Matthies and Humbert, 1993) imposes the constraint that homogenized elastic stiffnesses should be equal to the inverse of the homogenized elastic compliances. The geometric mean \mathbf{C}^G is calculated as follows:

$$\mathbf{C}^G = e^{\left[\frac{1}{|Y|} \int_Y \ln(\mathbf{C}) dY \right]}, \quad (3.3)$$

where $e^{(\cdot)}$ and $\ln(\cdot)$ denote the matrix exponential and matrix logarithm, respectively (e.g. Higham, 2008).

3.3.2 Asymptotic Expansion Homogenization Formulation with Finite Element Implementation

All estimates presented in the previous section depend only on the relative volume fraction and crystallographic orientation of mineral grains that make up the rock, and do not take the elastic interplay among the different grains into account. Interaction between neighboring grains result in intra-grain heterogeneous stress and strain fields that may be resolved by solving the three-dimensional elastic equilibrium equations at the microscale while enforcing the continuity of displacements and tractions across grain boundaries. Asymptotic expansion homogenization (AEH) is one such structure-based approach for the comprehensive micromechanical analysis of heterogeneous materials. An important difference between AEH and the averaging methods described in the introduction is that AEH has explicit physical meaning; it provides a macroscale solution that arises from the intricacies of the microstructure, so it captures the effects of the grain distributions and resulting grain-scale interactions. AEH has a strong mathematical basis (Bensoussan et al., 1978) and has been extensively validated and successfully used to analyze fiber- and particle-reinforced composite materials (e.g., Guedes and Kikuchi, 1990; Fish and Wagiman, 1992; Vel and Goupee, 2010).

The AEH method simultaneously considers two distinct scales, namely the characteristic length L of the large scale structure of interest and the width ℓ of the polycrystalline sample (Figure 3.1a). When the rock is subjected to a displacement or stress, the resulting internal stresses and strains will be distributed heterogeneously throughout the microstructure (e.g., Tullis et al., 1991; Johnson et al., 2004; Naus-Thijssen et al., 2010). If the microstructural geometry is periodic, the resulting stresses and strains will vary rapidly on the scale of the periodicity (Sanchez-Palencia, 1981; Goupee and Vel, 2010). Accordingly, all macroscale field variables are defined to have a periodic dependence on the microstructure. As long as the macroscale is much larger than the microscale (greater than 3 orders of magnitude), the bulk elastic properties of the rock can be evaluated using AEH. Although real rocks do not necessarily exhibit a strictly periodic microstructure, the synthetic microstructures considered in the present work are periodic. Terada et al. (2000) have demonstrated that, for a given sample volume, periodic boundary conditions yield more accurate bulk stiffnesses than either displacement or traction boundary conditions even when the sample volume does not exhibit actual periodicity at the microscale. This is due largely to the boundary effects associated with displacement or traction boundary conditions. Thus, assuming a periodic microstructure, while not necessarily true for a given rock sample, leads to the most accurate results.

When a polycrystalline sample is subjected to small deformations in the linear elastic regime, the microscale displacement fluctuations at any point \mathbf{y} within the sample will be proportional to the average macroscopic strains. The AEH method introduces 18 location-dependent proportionality constants $\chi_i^{kl}(\mathbf{y})$ (also known as characteristic functions) that relate the 3 components of the microscale displacement fluctuations at a point in the sample to the 6 average macroscopic strains. The characteristic functions are continuous functions of the sample coordinates \mathbf{y} due to the assumed continuity of displacements across grain boundaries. The microscale strains are related to the average macroscale strains through the characteristic

functions, and the corresponding spatially-varying microscale stresses are obtained using Hooke's law for anisotropic materials. Satisfaction of the 3-D elastic equilibrium equations results in a system of partial differential equations for the characteristic functions $\chi_i^{kl}(\mathbf{y})$ which are solved numerically. The resulting characteristic functions have first order correlation to all microstructural features including the size, shape, elastic stiffnesses, crystallographic orientation and spatial arrangement of the grains. The bulk elastic stiffnesses are obtained using the characteristic functions and the spatially-varying stiffnesses in the sample frame through volume or area integrations as follows

$$C_{ijkl}^{AEH} = \frac{1}{|Y|} \int_Y \left(C_{ijkl} + C_{ijpq} \frac{\partial \chi_p^{kl}}{\partial y_q} \right) dY. \quad (3.4)$$

The AEH formulation for the bulk stiffness tensor thus consists of two terms in the integrand. The first term is the traditional Voigt bound. The second term, involving the 18 characteristic functions, may be viewed as a correction to the Voigt bound that takes into account the precise grain scale interactions.

The characteristic functions $\chi_i^{kl}(\mathbf{y})$ are computed using standard FE techniques (e.g. Cook et al., 2002). The entire sample domain is discretized using six-noded triangular elements with quadratic shape functions (e.g. Cook et al., 2002). A FE mesh that conforms to the grain boundaries is used to model the complex heterogeneous microstructure (e.g. see Figure. 3.2(d)). The partial differential equations for the characteristic functions lead to a linear system of equations for the nodal values which are solved using periodic conditions on the four boundaries of the sample domain. The characteristic function values at an arbitrary point in the sample domain can be inferred from the nodal values and the shape functions. The characteristic functions $\chi_i^{kl}(\mathbf{y})$, once computed, can be used to obtain the effective stiffnesses using eq. 3.4. In addition, it is possible to compute the grain-scale distributions of the strains and stresses for

prescribed macroscopic deformation using the characteristic functions. Details of the AEH method and the finite element implementation are presented in Section 3.7.

The AEH formulation is applicable to three-dimensional microstructures. However, due to the inherent uncertainty in microstructural topology in the third dimension, and the high computational cost involved in meshing and solving a full 3D model, we concern ourselves here with 2D microstructures for which the grain boundaries are projected into the third dimension (y_2 coordinate direction). Since none of the desired field variables χ_i^{kl} vary as a function of the y_2 coordinate, a 2D FE mesh in the $y_1 - y_3$ plane is sufficient for obtaining all the non-zero elastic constants in the 3D homogenized stiffness tensor C_{ijkl}^{AEH} as long as all three degrees of freedom are retained at each node.

3.3.3. Wave Propagation and Measures of Seismic Anisotropy

The wavelengths of seismic waves propagating through Earth's crust are much larger than the rock's microstructure. Therefore it is valid to study wave speeds in unbounded regions in which the rock is represented by an equivalent homogenized media. We use the Christoffel equation (Christoffel, 1877) to derive the three wave speeds:

$$\left[C_{ijkl}^H n_j n_l - \rho^H V^2 \delta_{ik} \right] a_k = 0 \quad (3.5)$$

in which C_{ijkl}^H is the homogenized stiffness tensor obtained using either the AEH method or one of the analytical averaging schemes described in Section 3.3.1, n_i are the components of the unit vector that defines the wave propagation direction, ρ^H is the homogenized density, V is the wave speed, and a_i are the displacement amplitudes. The Christoffel equation represents an eigenvalue problem with eigenvalues $\rho^H V^2$ and corresponding eigenvectors a_k . The solution of (3.5) yields three real eigenvalues, and hence, three real wave speeds V (e.g. Auld, 1990), one quasi P-wave denoted by V_p and two quasi S-waves denoted by V_{S1} and V_{S2} ($V_{S1} \geq V_{S2}$). The quasi P-wave

corresponds to the longitudinal mode of vibration. It has the largest displacement component along the propagation direction amongst the three modes. The two remaining waves are termed the quasi-shear modes and they correspond to transverse modes of vibration with displacement vectors approximately orthogonal to the propagation direction \mathbf{n} .

An elastically anisotropic rock will exhibit different P- and S-velocities when the propagation direction \mathbf{n} of the incoming seismic wave is changed. Therefore we plotted our velocity data against a varying incidence angle γ . The incidence angle is the angle between the propagation direction and the y_3 axis in the $y_1 - y_3$ plane (Figure 3.1b).

Besides the P- and S-velocities, we also calculate how the P-delay ($\Delta t_p(\gamma)$) and the shear wave splitting ($\Delta t_s(\gamma)$) vary with changing γ . The P-delay measures the delay in time required by a P-wave to travel a unit distance relative to a reference P-wave velocity, in our case the V_p^{\max} , as a function of incidence angle:

$$\Delta t_p(\gamma) = \frac{1}{V_p(\gamma)} - \frac{1}{V_p^{\max}}. \quad (3.6)$$

The shear wave splitting measures the difference in arrival times for the two S-waves per unit propagation distance, as a function of incidence angle:

$$\Delta t_s(\gamma) = \frac{1}{V_{s2}(\gamma)} - \frac{1}{V_{s1}(\gamma)}. \quad (3.7)$$

In order to quantify and compare multiple microstructural variables (e.g., modal abundance, crystallographic orientations) in one figure, parameters independent of the incidence angle are necessary. The percentage anisotropy for the P- and S-waves (Birch, 1960) and the normalized $V_p(45^\circ)$ percentage (Okaya and Christensen, 2002) are such parameters. The percentage anisotropy of the two waves is calculated using

$$A = \frac{(V^{\max} - V^{\min})}{0.5(V^{\max} + V^{\min})} \times 100\%, \quad (3.8)$$

where V^{\max} and V^{\min} are the maximum and minimum values from either the P or S wave velocities calculated over the entire range of angles γ . Crustal foliated rocks can be highly seismically anisotropic (e.g., 30% A_p and 35% A_s , Johnson and Christensen, 1995; 20.5% A_p and 37.4% A_s , Okaya and Christensen, 2002; 16.6% A_p and 23.9% A_s , Lloyd et al., 2009).

Okaya and Christensen (2002) showed that the P-wave velocity measured at an incidence angle of 45° deviates from the elliptical hexagonal behavior that generally is used to infer the P-wave velocity at this incidence angle. In other words, when $V_p(45^\circ)$ is assumed to be the average of the measured $V_p(0^\circ)$ and $V_p(90^\circ)$ in place of actual petrophysical measurements, the bulk stiffness tensor thus obtained can be inaccurate thereby leading to erroneous non-axial wave speeds. Okaya and Christensen (2002) called this phenomenon the P45 effect and characterized it through the parameter v_{p45} which is defined as

$$v_{p45} = \frac{(V_p(45^\circ) - V_p(0^\circ))}{(V_p(90^\circ) - V_p(0^\circ))} \times 100\% \quad (3.9)$$

3.4. Creation of the Synthetic Rock Microstructures

In order to systematically investigate the role of different microstructural variables we build simplified rocks made up of 1) different amounts of quartz and muscovite, with 2) varying crystallographic orientations, and 3) varying spatial distributions of the muscovite grains. All created microstructures are periodic in both the y1 and y3 direction, as is assumed in the AEH method.

Quartz is a trigonal mineral (e.g. Nye, 1985) with mild elastic anisotropy and muscovite is a monoclinic mineral with strong elastic anisotropy as can be inferred from their stiffness tensors (quartz - Hearmon, 1979; muscovite – Vaughan and Guggenheim, 1986):

$$\mathbf{C}^{Quartz} = \begin{bmatrix} 86.6 & 6.7 & 12.6 & -17.8 & 0 & 0 \\ & 86.6 & 12.6 & 17.8 & 0 & 0 \\ & & 106.1 & 0 & 0 & 0 \\ & & & 57.8 & 0 & 0 \\ Sym. & & & & 57.8 & -17.8 \\ & & & & & 39.95 \end{bmatrix} \quad (3.10)$$

$$\mathbf{C}^{Muscovite} = \begin{bmatrix} 184.3 & 48.3 & 23.8 & 0 & -2 & 0 \\ & 178.4 & 21.7 & 0 & 3.9 & 0 \\ & & 59.1 & 0 & 1.2 & 0 \\ & & & 16.0 & 0 & 0.5 \\ Sym. & & & & 17.6 & 0 \\ & & & & & 72.4 \end{bmatrix} \quad (3.11)$$

both in GPa and derived at room temperature and atmospheric pressure. In our microstructure models the quartz grains are represented by 30 similarly-sized hexagons and the muscovite grains are represented by rectangles of length $a = 0.4\ell$ and thickness $b = 0.05\ell$ (see Figure 3.2). We tested 4 different orientations for the quartz grains: three in which the c-axis (or least compliant axis) of the quartz grains is parallel to the three different orthogonal coordinate axes (y_1 , y_2 and y_3) and one in which all quartz grains are oriented randomly. The muscovite grains are oriented with their c-axes parallel to the plane of the paper and perpendicular to the long dimension of the grains; the a- and b-axes are oriented randomly. The muscovite grains are overlaid at random locations over the grid of hexagons until the desired muscovite modal fraction (ϕ_{Ms}) is achieved, as shown in Figure 3.2b. The muscovite grains are oriented with a mean angle of zero degrees with respect to the y_1 axis plus or minus a given 1σ standard deviation angle (α). The geometry in Figure 3.2b has a ϕ_{Ms} of 0.2 and α of 10° . A sample synthetic microstructure with a higher

muscovite volume fraction φ_{Ms} of 0.6 and α of 10° is shown in Figure 3.2c. Once the desired microstructure is created the image is meshed as described in section 3.3.2.

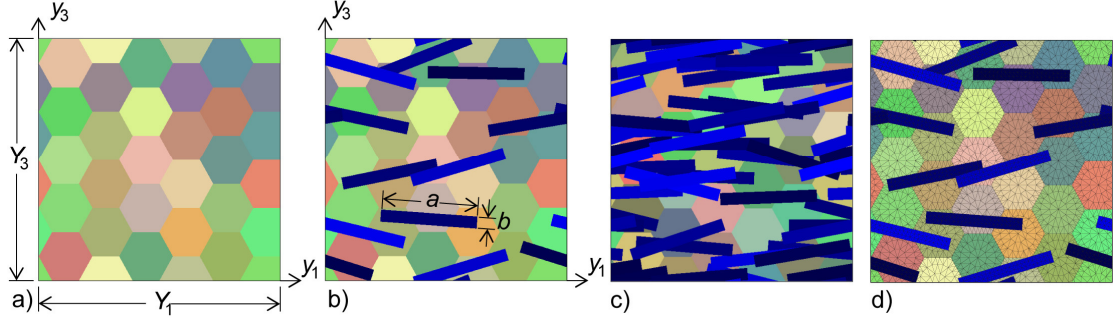


Figure 3.2. Construction of the microstructure. (a) Base cell of sample synthetic microstructure showing the grid of quartz crystals, the different colors indicate different orientations. (b) Completed synthetic microstructure with rectangular muscovite grains yielding a muscovite modal fraction of 0.2 and $\alpha= 10^\circ$. The different colors of blue indicate different orientations for the a- and b-axes for the muscovite grains. (c) Sample synthetic microstructure with a muscovite modal fraction of 0.6 and $\alpha= 10^\circ$ and (d) AEH finite element mesh corresponding to the microstructure in (b).

3.5. Results and Discussion

We used the AEH method, with an FE implementation, to study the influence of different microstructural variables on seismic wave speed anisotropy in a simplified quartz-muscovite rock sample. We also compared the results to values calculated with the more commonly used Voigt and Reuss bounds. A detailed FE convergence study was performed to ensure that the AEH results presented in the tables and figures are accurate. Depending on the complexity of the microstructure, a mesh consisting of anywhere from 1,000 to 9,000 elements was necessary to obtain wave speeds that are accurate to 3 significant digits. A representative FE mesh is shown in Figure 3.2d for the sample microstructure depicted in Figure 3.2b.

Two out of the eighteen characteristic functions $\chi_k^{pq}(\mathbf{x}, \mathbf{y})$ required to compute the homogenized stiffness tensor are shown in Figures 3.3a and 3.3b for the sample microstructure depicted in Figure 3.2b. The characteristic functions $\chi_1^{11}(\mathbf{y})$ and $\chi_1^{13}(\mathbf{y})$ represent the fluctuation in the displacement component u_1 for unit average normal strain \bar{e}_{11} and unit average

shear strain $\bar{\gamma}_{13}$, respectively. The other 16 characteristic functions likewise exhibit intricate spatial variations due to the complex elastic interaction among individual grains with different crystallographic orientations.

Calculation of the bulk elastic stiffness does not require deformation of the sample. However, in order to show that the AEH method can be used to calculate the grain-scale distributions of stresses and strains during deformation, the microstructure from Figure 3.2b is subjected to an average shear strain $\bar{\gamma}_{13}$ of 0.1% at atmospheric confining pressure. The characteristic functions are used to obtain the microstructural shear strains and stresses shown in Figures 3.3(c), (d), and the bulk stiffness tensor. The muscovite grains experience a larger shear strain than the quartz grains due to their low shear moduli, and as a result, quartz grains off the tips of the muscovite grains show concentrations of shear stress.

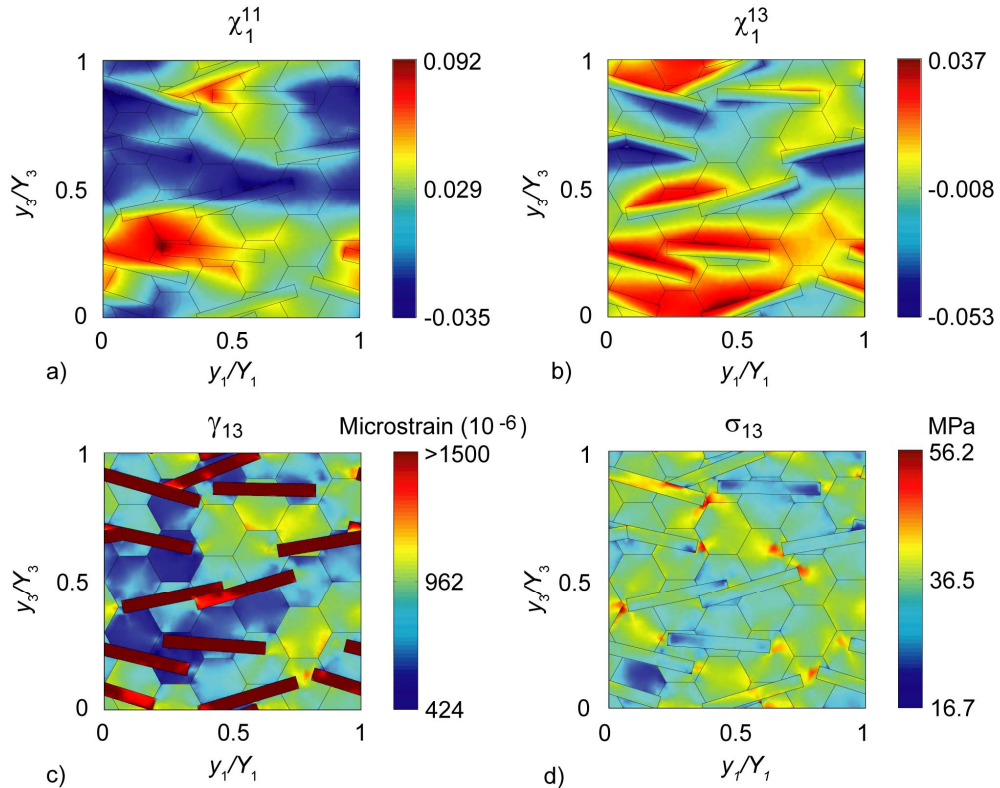


Figure 3.3. Characteristic functions and shear strain and stress for the microstructure shown in Figure 3.2b. (a) Characteristic function χ_1^{11} , (b) characteristic function χ_1^{13} , (c) the microstructural shear strain γ_{13} , and (d) microstructural shear stress σ_{13} .

As is evident from Figure 3.3, the elastic stiffness tensors, modal fractions, crystallographic orientations and spatial arrangement of the grains throughout the model domain cause non-uniform displacement and strain fields. The resulting homogenized stiffness tensor reflects these grain-scale elastic interactions. All homogenized stiffness tensors, which are used to calculate the wave speeds, are generated via an ensemble average of 100 distinct synthetic microstructural domains with similar modal fractions and distribution statistics. This is done in lieu of meshing and analyzing a single large microstructure since it is computationally more efficient to analyze several smaller microstructures and it gives the same homogenized stiffness tensor (e.g. Vel and Goupee, 2010).

3.5.1. Comparison of AEH and Analytic Estimates

In order to illustrate the importance of a method that includes the spatial arrangements of grains, instead of just the modal fraction of the constituent minerals and their individual crystallographic orientations, a comparison is made between results calculated with both the AEH method and the analytical averages described in section 3.3.1 of some simple two mineral (quartz and muscovite) microstructures. We build three models in which the modal fraction of muscovite (0.2) and the orientations of both the muscovite ($\alpha=0^\circ$) and quartz (c-axis // y2) crystals are kept constant, but the distribution of the muscovite grains is varied. In the first model the muscovite grains are grouped horizontally in a band, in the second model the grains are stacked vertically in a band, and in the third model the muscovite grains are distributed randomly (see Figure 3.4 for these microstructures). Because the Voigt and Reuss bounds and their means are only based on the modal fractions and orientations of the constituent minerals their results are the same for each model. The results calculated with the AEH method are dependent on the arrangement of the grains, and so differ from model to model. Figure 3.4 shows the P- and S- wave velocities, P-delay, and shear wave splitting versus the incidence angle for the three different microstructures.

The P-wave velocities calculated with the AEH method for the different models are very similar to the means for incidence angles 30-60 degrees. The sample with the vertically stacked muscovite grains gives AEH results closest to the geometric mean. The model with the horizontally clustered muscovite grains is closest to the Reuss bound at low incidence angles ($<30^\circ$), and closest to the Voigt bound at higher incidence angles ($>60^\circ$).

The S1-wave velocities calculated with the AEH method for the different models show the largest variety at incidence angles below 55° . Below this incidence angle the results from the model with the vertically stacked grains is best estimated by the geometric mean, and the model with the horizontally clustered micas is best estimated by the Reuss average. Above this incidence angle the AEH results for the different models are very similar and range from being closest to the geometric mean result at 55° , to being closest to the Reuss result at 90° . The S2-wave velocities are very similar for the entire range of incidence angles. They vary in being closest to the result calculated using the Reuss bound ($\sim 0^\circ$), the Voigt bound ($\sim 40^\circ$), and the means ($\sim 25^\circ$ and $\sim 90^\circ$).

The resulting P-delay curves show a large variety at incidence angles below 30° . The P-delay difference between the model with the vertically stacked muscovite grains and the model with the banded, horizontal mica grains is 0.005 seconds, or 20% at $\gamma=0^\circ$. The resulting shear wave splitting curves show the largest variety at an incidence angle of approximately 25° , where there is a difference between the models is 0.015 seconds, or 18%.

Overall the velocities of the P- and S- waves all fall within the Voigt and Reuss bounds, which is as expected. But the results show a non-systematic deviance from the bounds and their means. These results show that, when changing the distribution of grains within a microstructure, the P-delay and S-wave splitting can change significantly. This change in values is not captured by the analytical methods.

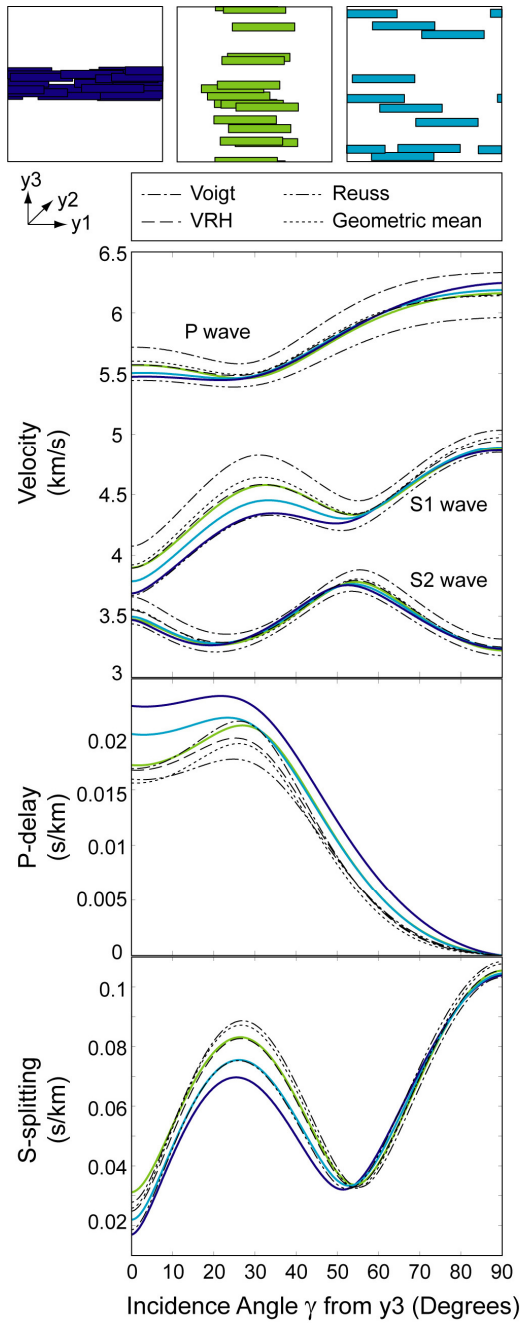


Figure 3.4. P- and S-velocities, P-delay and shear wave splitting calculated for three separate microstructural models shown at the top of the figure. Each model has the same modal fraction of muscovite (0.2), and the same muscovite ($\alpha=0^\circ$) and quartz orientations (c-axis // y_2), but a different distribution of muscovite grains. Results for the AEH-FE method are microstructure dependent, and therefore color-coded for each of the models. Results for the Voigt and Reuss bounds, and geometric and arithmetic means, are not microstructure dependent and therefore identical for each model.

3.5.2. Sensitivity Analysis of Modal Abundances, Orientations and Spatial Distribution

A comprehensive parametric study is performed on the synthetic quartz-muscovite rock to assess the roles of modal fraction and crystallographic orientation. In order to show the influence of both minerals we modeled rocks with no muscovite at all (pure quartz), to a rock consisting of almost pure muscovite. Pure quartz or muscovite rocks are relatively rare in nature, but provide useful end-members for the modeling. Similarly, uniform quartz c-axis orientations are not found in nature, but provide useful end-member configurations. The AEH method is used for our analyses, and the resulting bulk stiffness tensors are used to determine seismic wave velocities and the anisotropy measures as defined in Section 3.3.3. The microstructural symmetry of the model rocks allows the full incidence-angle behavior to be evaluated over the range $\gamma = 0$ -90 degrees.

Figure 3.5 shows the V_p , V_{S1} and V_{S2} velocities, the P-delay and shear wave splitting versus the incidence angle for different quartz-grain orientations at different ϕ_{Ms} . In order to isolate the effects of ϕ_{Ms} and quartz orientation, α is held constant at 0° . For pure quartz ($\phi_{Ms} = 0$), the rock behaves nearly isotropic if the quartz grains are oriented randomly, as expected. When the quartz c-axes are parallel to y_2 , the V_p curve displays a fairly isotropic behavior as well, due to the trigonal symmetry of quartz: the strong axis of the material is oriented perpendicular to the plane of the paper ($//y_2$). The three a-axes all have the same compliance and are all oriented parallel to the plane of the paper (y_3 - y_1), which is the plane in which the incidence angle is taken, leading to very similar velocities at the different incidence angles. The velocity profiles become progressively more similar as muscovite is added owing to its strong elastic anisotropy. For the no muscovite cases, the V_{S1} and V_{S2} values are very similar at either incidence angle 32° or 59° , depending on the quartz orientation. With increasing ϕ_{Ms} these “crossover” locations move closer to one another to eventually occur at about 37° when 90% of the model consists of muscovite. As

expected, the P-delay and shear-wave splitting values increase with increasing muscovite. The greatest P-delays occur at $\gamma=0^\circ$ where the wave propagates sub-parallel to the compliant direction of muscovite (c-axis), and the greatest shear splitting occurs at $\gamma=90^\circ$ where the wave propagates sub-parallel to the stiff directions of muscovite (a- and b-axes).

Figure 3.6 shows the V_P , V_{S1} and V_{S2} velocities, the P-delay and shear splitting versus the incidence angle for different α values at three different φ_{Ms} . In order to isolate the effects of φ_{Ms} and α , the quartz grains are randomly orientated leading to an effectively isotropic matrix. As in Figure 3.5, increasing φ_{Ms} leads to larger variations in the V_P , V_{S1} and V_{S2} curves, which give rise to greater peak P-delay and shear-wave splitting values. Conversely, a progressive increase in α reduces the bulk anisotropy, which manifests as diminished P-delay and shear-wave splitting values for most γ . Another effect of increasing isotropy, caused either by decreasing φ_{Ms} or increasing α , is that the γ at which V_{S1} and V_{S2} achieve similar values decreases. This can be seen clearly in the shear-wave splitting curves where the $\Delta t_S = 0$ s/km occurs at an ever smaller incidence angle when either φ_{Ms} is decreased or α is increased.

Figure 3.7a shows A_P as a function of φ_{Ms} for microstructures with different quartz orientations and α . When the quartz grains are oriented randomly or with c-axes parallel to y_1 or y_2 , A_P increases with increasing φ_{Ms} . If the c-axes of quartz grains are oriented parallel to y_3 the anisotropy decreases until φ_{Ms} is approximately 15 to 22%, depending on α , and then increases with increasing φ_{Ms} . This dip in A_P is largely due to the alignment of the stiff axis of the quartz with the compliant axis of the muscovite. Because of this alignment the initial anisotropy that is caused by the stiff axis of quartz being parallel to y_3 is progressively overwhelmed by the more anisotropic muscovite, which ultimately dominates the bulk anisotropy. Increasing α has the predicted effect of decreasing A_P across the range of φ_{Ms} . As stated in Section 3.3.3, petrophysically determined A_P values in foliated crustal rocks can be as high as 30%. Our results

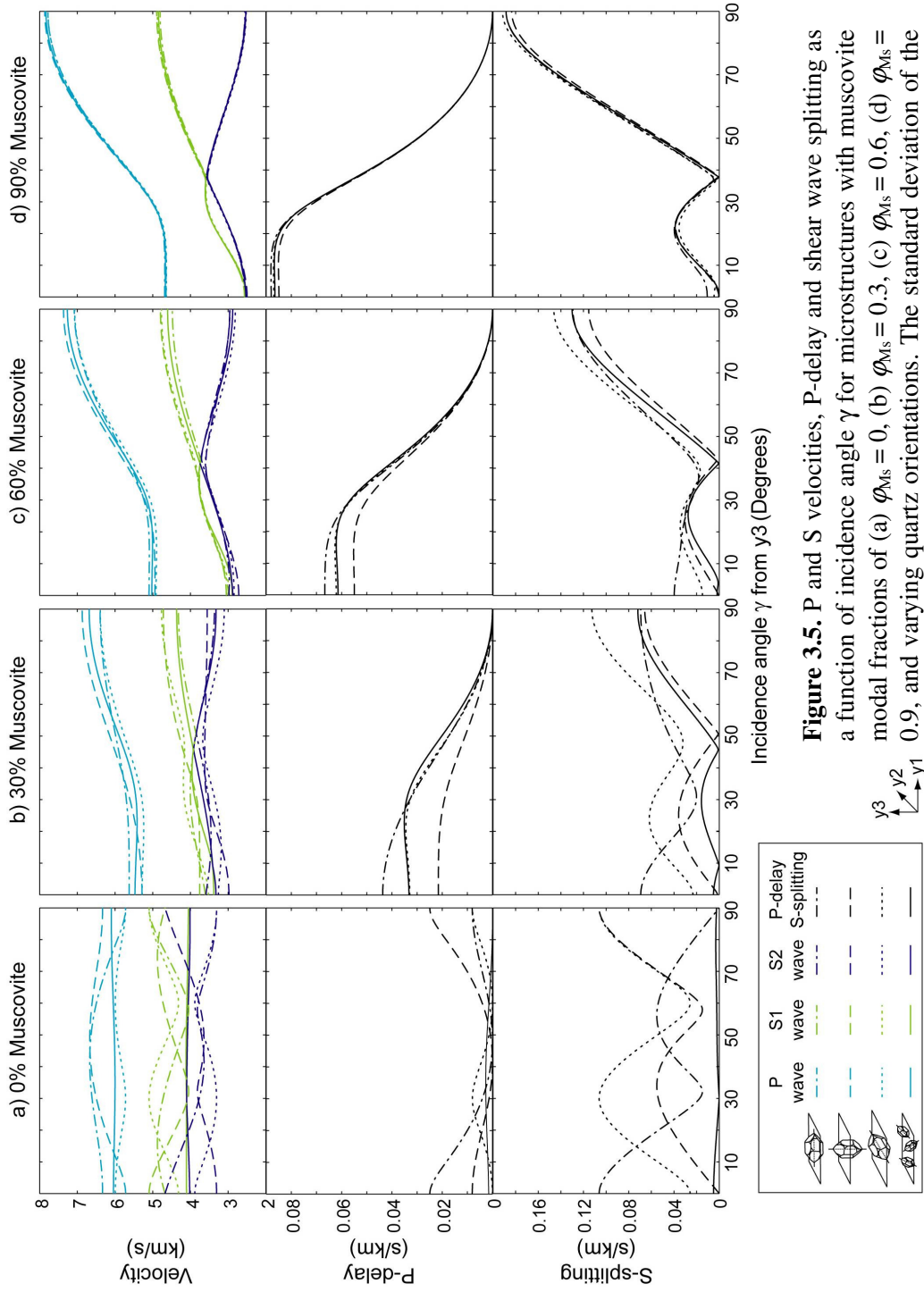


Figure 3.5. P and S velocities, P-delay and shear wave splitting as a function of incidence angle γ for microstructures with muscovite modal fractions of (a) $\varphi_{Ms} = 0$, (b) $\varphi_{Ms} = 0.3$, (c) $\varphi_{Ms} = 0.6$, (d) $\varphi_{Ms} = 0.9$, and varying quartz orientations. The standard deviation of the muscovite orientation distribution is 0° for all plots. The axis of the quartz crystal shown in the legend is its c-axis and is oriented parallel to y_1 , y_3 , and y_2 , or oriented randomly in the plots. All results are calculated using the AEH-FE method.

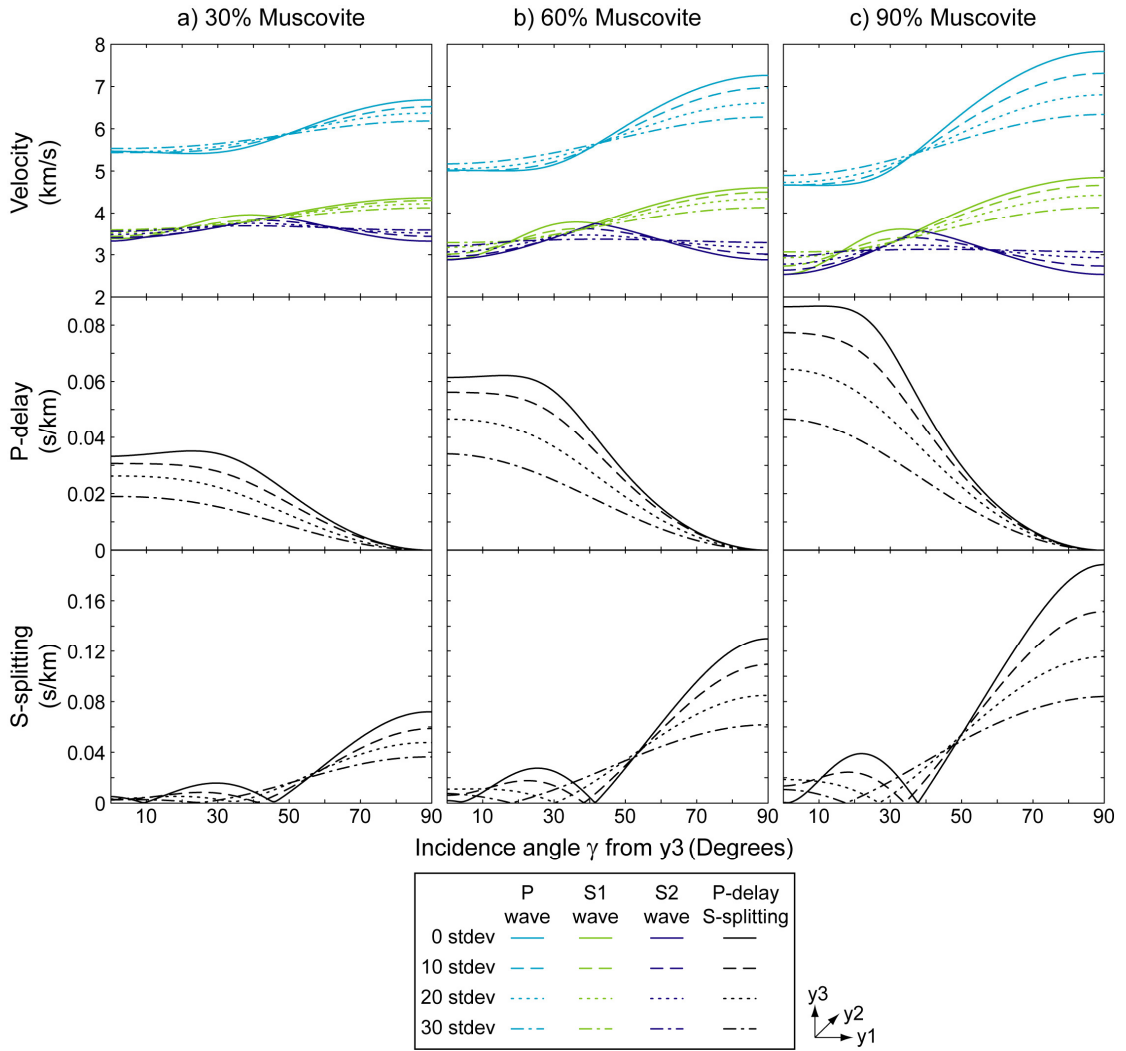


Figure 3.6. P and S velocities, P-delay and shear-wave splitting as a function of incidence angle γ for microstructures with muscovite modal fractions of (a) $\varphi_{Ms} = 0.3$, (b) $\varphi_{Ms} = 0.6$, (c) $\varphi_{Ms} = 0.9$, and varying muscovite orientation distributions ($\alpha=0-30$). The quartz is randomly oriented for all plots. All results are calculated using the AEH-FE method.

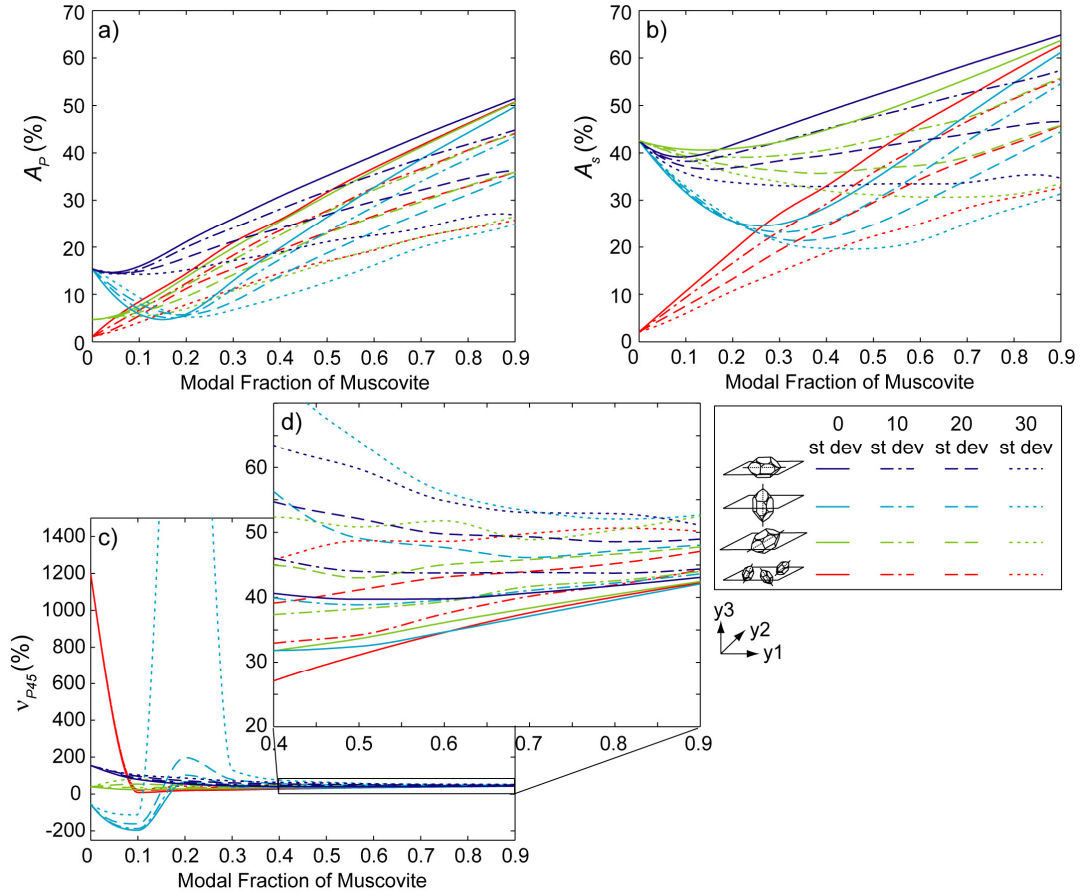


Figure 3.7. Percentage anisotropy of (a) the P-wave, (b) percentage anisotropy of the S-waves, and (c)-(d) $V_P(45^\circ)$ as a function of the modal fraction of muscovite. All results are calculated using the AEH-FE method.

show A_P values as high as 50%, but only for rocks consisting almost entirely of strongly aligned muscovite, which are only rarely represented in continental crust.

Figure 3.7b shows the same information as Figure 3.7a for A_S . Similar trends are apparent between A_P and A_S , but the crystallographic orientations of quartz clearly have a larger effect on the A_S than on the A_P . For example, when the c-axes of the quartz grains are oriented parallel to any of the reference-frame axes, A_S is 43% for $\phi_{Ms}=0$. When the quartz c-axes are aligned with y_3 , between 26 and 45% muscovite is required, depending on α , for muscovite to overwhelm the effects of the quartz anisotropy. When the quartz c-axes are aligned with y_1 or y_2 this percentage ranges from 9 to 64%. As stated in Section 3.3.3, petrophysically determined A_S values in

foliated crustal rocks can be as high as 37%. Our results show A_S values greater than 60%, but only for rocks consisting almost entirely of strongly aligned muscovite.

The results plotted in Figures 3.7a and b demonstrate that the orientation of matrix grains in mica-rich rocks can play an important role in the bulk elastic behavior, particularly at low φ_{Ms} . Although the single-point-maximum quartz crystallographic orientations used here are extreme, it is evident that strongly aligned crystallographic orientations in minerals such as quartz and feldspar in schists can have an important effect on seismic anisotropy measures in mica-rich rocks.

Figures 3.7c and 3.7d show v_{P45} versus φ_{Ms} for different quartz grain orientations and α values. When φ_{Ms} is less than approximately 33%, the percentage magnitudes of v_{P45} are very high ($\gg 100\%$). These high values reflect the fact that the denominator in the v_{P45} calculation is the difference between $V_P(0^\circ)$ and $V_P(90^\circ)$, and at φ_{Ms} values less than approximately 33%, this difference is very small. For the microstructures containing the lower and intermediate amounts of muscovite, the quartz orientation seems to play a major role on v_{P45} . With greater φ_{Ms} , however, this influence starts to diminish and α begins to play a more important role as increasing α leads to increasing v_{P45} . This is supported by the V_P curves for $\varphi_{Ms} = 0.6$ in Figure 3.6, where although $V_P(0^\circ)$ and $V_P(45^\circ)$ are approximately the same for all α shown, $V_P(90^\circ)$ diminishes significantly with increasing α . This trend maintains the numerator in equation (3.9), whereas the denominator diminishes with increasing α , thus increasing v_{P45} .

The causes for the P45 effect described in section 3.3.3 are still incompletely understood. Okaya and Christensen (2002) reported that rocks of broadly similar mineralogy and microstructure (schists) had very different v_{P45} values. Our results show that all the microstructural variables we investigated (φ_{Ms} , α , and quartz orientation) can influence the v_{P45} , with the orientation of muscovite (α) having the largest effect.

3.6. Conclusions

The effects of specific microstructural characteristics on seismic wave-speed anisotropy of crustal rocks have been explored. We studied simplified microstructures consisting of quartz and muscovite with variable modal fractions and crystallographic orientations. The homogenized elastic stiffnesses were obtained via the AEH method and were subsequently utilized to calculate the wave speed velocities via solution of the Christoffel equation.

The analyses performed in this work leads to the following conclusions:

- 1) When comparing the wave velocities obtained using AEH with those obtained using the Voigt and Reuss bounds or geometric and arithmetic mean estimates, no systematic trend has emerged between the AEH results and these other methods. The AEH results fall between the two bounds, but even though the geometric and arithmetic means seem to provide reasonable estimates, they generally over- or under-estimate actual velocities and measures of anisotropy such as P-delay and shear-wave splitting. Our results show that grain-to-grain interactions are important in determining the bulk elastic stiffness of a material, and thus the AEH method provides a more robust result than the physically meaningless means of the Voigt and Reuss bounds.
- 2) At minimal to low modal muscovite, the orientation of quartz grains plays a significant role on the shape of the V_P , V_{S1} and V_{S2} trends as a function of the incidence angle γ . When the quartz grains are oriented randomly, the bulk rock exhibits quasi-isotropic seismic wave speed behavior. If the quartz grains in the matrix have a strong crystallographic preferred orientation, the wave speeds show a more complicated dependence on the incidence angle.
- 3) For microstructures in which the stiff (c-) axes of quartz are aligned with the compliant (c-) axes of muscovite, A_P and A_S values initially diminish as φ_{Ms} increases only to rise again at a specific φ_{Ms} . The initial anisotropy introduced by the quartz alignment is progressively overwhelmed by the more anisotropic muscovite, which ultimately dominates the bulk anisotropy.

4) The normalized $V_p(45^\circ)$ value, V_{p45} , is not strongly affected by quartz orientation for moderate and high muscovite modal fractions. Increasing α generally increases V_{p45} for $0.33 < \phi_{Ms} < 0.9$. In addition, certain combinations of muscovite modal fraction, standard deviation of muscovite grain orientation, and quartz grain orientations can give rise to very high V_{p45} values.

3.7. Details of the Asymptotic Expansion Homogenization Method (Appendix to paper)

The AEH method simultaneously considers two distinct scales, namely the characteristic length L of the large scale structure of interest and the width ℓ of the sample. The two length scales are related by a scaling parameter ε which is defined as the ratio of the width of the sample to the characteristic dimension of the large scale structure, i.e., $\varepsilon = \ell/L$. The AEH method assumes a clear separation between the two scales, i.e. $\varepsilon \ll 1$. In addition, the microstructure is assumed to be periodic and a microscopic coordinate \mathbf{y} is used to identify points within the microscale sample. In the present work, L is of the order of several meters to hundreds of meters and the sample size ℓ is of the order of millimeters. The corresponding ratio ε is of the order 10^{-3} to 10^{-5} which is in keeping with the assumption of the AEH method.

In the AEH formulation, the displacements u_i of a point in a heterogeneous sample is decomposed into a macroscopic displacement component that represents the average displacement of the entire sample and a superimposed fluctuating component due to the elastic interaction between the grains as

$$u_i = \bar{u}_i + \varepsilon \hat{u}_i(\mathbf{y}), \quad (3.12)$$

where \bar{u}_i represent the average macroscale displacements and $\hat{u}_i(\mathbf{y})$ represent the microscale displacement fluctuations which are proportional to the scaling parameter ε .

Assuming linear elastic behavior, the microscale displacement fluctuations at a point within the sample will be proportional to the average macroscopic strain. This link between the

two scales is expressed mathematically in the following manner (Bensoussan et al., 1978; Sanchez-Palencia, 1981, 1983)

$$\hat{u}_i(\mathbf{y}) = \chi_i^{kl}(\mathbf{y}) \bar{e}_{kl}, \quad (3.13)$$

where $\chi_i^{kl}(\mathbf{y})$ are position dependent proportionality constants (referred to as the characteristic functions in the main text) that relate the six average macroscopic strains \bar{e}_{kl} to the three microscale displacement fluctuations at a point in the sample. Summation is implied over the repeated indices k and l in (3.13). The eighteen characteristic functions $\chi_i^{kl}(\mathbf{y}) = \chi_i^{lk}(\mathbf{y})$ are continuous functions of the sample coordinates \mathbf{y} due to the assumed continuity of displacements across grain boundaries. The strains at a point within the sample are related to the average macroscopic strains via the characteristic functions as,

$$e_{kl}(\mathbf{y}) = \bar{e}_{kl} + \frac{1}{2} \left(\frac{\partial \chi_k^{pq}}{\partial y_l} + \frac{\partial \chi_l^{pq}}{\partial y_k} \right) \bar{e}_{pq}, \quad (3.14)$$

The corresponding stresses at a point in the sample are related the average macroscopic strains using Hooke's law for anisotropic materials,

$$\sigma_{ij}(\mathbf{y}) = C_{ijkl}(\mathbf{y}) e_{kl}(\mathbf{y}), \quad (3.15)$$

where $C_{ijkl}(\mathbf{y})$ are the spatially-varying elastic stiffnesses in the sample coordinate frame. The stresses are substituted into the three-dimensional equilibrium equations of elasticity to obtain the following system of partial differential equations for the characteristic functions,

$$\frac{\partial}{\partial y_j} \left[C_{ijpq}(\mathbf{y}) \frac{\partial \chi_p^{kl}(\mathbf{y})}{\partial y_q} \right] = - \frac{\partial C_{ijkl}(\mathbf{y})}{\partial y_j}. \quad (3.16)$$

which are solved using periodic boundary conditions. This equation shows that the characteristic function is only dependent on the spatial distribution of the elastic stiffnesses from the microstructural domain. The effective elastic stiffnesses C_{ijkl}^{AEH} of the sample are obtained through volume or area integration as

$$C_{ijkl}^{AEH} = \frac{1}{|Y|} \int_Y \left(C_{ijkl} + C_{ijpq} \frac{\partial \chi_p^{kl}}{\partial y_q} \right) dY. \quad (3.17)$$

The partial differential equations for the characteristic functions $\chi_i^{kl}(\mathbf{y})$ are solved using the finite element method (e.g. Cook et al., 2002). The localization functions χ_i^{kl} are discretized using finite element shape functions as

$$\chi_i^{kl} = N_a(\mathbf{y}) d_{ai}^{kl}; \quad k, l = 1, 2, 3, \quad a = 1, 2, \dots, K, \quad (3.18)$$

where N_a is the finite element shape function for node a , d_{ai}^{kl} are the nodal constants for the localization functions and K is the number of nodes in the microstructure analysis domain. Substitution of the approximation (3.18) into the weak, or variational form (e.g. Hughes, 2000) of (3.16) results in the following coupled system of linear algebraic equations which are solved to obtain the nodal constants d_{ai}^{kl} ,

$$\mathbf{K} \mathbf{d}^{kl} = \mathbf{F}^{kl}, \quad (3.19)$$

where \mathbf{K} is a global stiffness matrix and \mathbf{F}^{kl} is a load, or global vector, both of which depend on the spatial distribution of the elastic stiffnesses (Vel and Goupee, 2010). The nodal values of the eighteen characteristic functions $\chi_i^{kl}(\mathbf{y})$ are obtained by solving (3.19) for different combinations of k and l . A detailed description of the finite element implementation of the AEH method can be found in Guedes and Kikuchi (1990).

Chapter 4

THE INFLUENCE OF CRENULATION CLEAVAGE DEVELOPMENT ON THE BULK ELASTIC PROPERTIES AND SEISMIC WAVE VELOCITIES OF PHYLLOSILICATE-RICH ROCKS*

4.1. Chapter Abstract

The anisotropy of seismic wave propagation is strongly influenced by the mineralogy and microstructure of rocks. Phyllosilicates are elastically highly anisotropic and are therefore thought to be important contributors to seismic anisotropy in the continental crust. Crenulation cleavage is one of the most common microstructural fabrics found in multiply-deformed, phyllosilicate-rich crustal rocks. We calculated the bulk elastic properties and resulting wave velocities for rock samples that preserved three different stages of crenulation cleavage development: an initial planar foliation, a moderately-developed crenulation cleavage, and a well-developed crenulation cleavage. Mineral orientation maps were obtained using electron backscatter diffraction and calculations were made using asymptotic expansion homogenization combined with the finite element method. We discuss the difficulties involved with sample preparation and data acquisition of phyllosilicate-rich rock samples. We compared our results to more conventional methods for calculating an aggregate stiffness matrix from a mineral orientation map, namely Voigt and Reuss averages. These averages do not account for grain-scale interactions and therefore deviate from the results calculated using asymptotic expansion homogenization. We show that rocks characterized by the planar foliation and the moderately developed crenulation cleavage are highly anisotropic, with a P-wave anisotropies up to 30.9% and S-wave anisotropies up to 34.2%, whereas the rock characterized by the well developed crenulation cleavage are only

** The content of this chapter will be submitted for publication by the end of February 2011 with Earth and Planetary Science Letters: Naus-Thijssen et al.*

mildly isotropic, with a P-wave anisotropy of 15.5% and S-wave anisotropy of 10.7%. Progressive development of the fabric also causes the orientations of P- and S-wave velocity maxima and S-wave polarization directions to change markedly. Despite the high anisotropy imparted by a planar schistosity, the variety of folds and fabrics typically found in phyllosilicate-rich rocks within larger-scale crustal volumes will tend to mute the anisotropy, possibly to the point of appearing nearly isotropic.

4.2. Introduction

Seismology is an essential tool for examining the structure and mineralogy of deeper parts of the Earth, and can provide valuable information regarding mantle-crust coupling and tectonic plate interactions (e.g., Silver, 1996; Savage, 1999; Karato et al., 2008). Numerous seismological investigations have recorded shear-wave splitting and P-wave delays, which are attributed to anisotropy in the mantle and, to a lesser extent, the crust. Anisotropy in seismic wave velocities can be caused by: (1) the presence of aligned fractures in the upper 10-15km of the crust (e.g., Crampin, 1981; Kaneshima et al., 1988), (2) the layering of material (e.g., Backus, 1962), and (3) the development of mineral lattice- and shape-preferred orientations (LPO and SPO, respectively) during the progressive accumulation of strain (e.g., Mainprice, 2007). Crustal structures such as folds and shear zones contain LPOs and SPOs that reflect the strain and metamorphism accompanying their formation. Knowing how these structures influence the seismic signal is important for interpreting seismic velocity data.

One of the most common fabrics in multiply-deformed, meta-pelitic, crustal rocks is crenulation cleavage (e.g., Williams et al., 2001), which is characterized by phyllosilicate-rich (P-) domains separated by quartz- and feldspar-rich (QF-) domains. Bell and Rubenach (1983) distinguished 6 stages of crenulation cleavage development (Figure 4.1). To investigate the influence of this important microstructure on seismic anisotropy in the crust we selected 3 areas within two different thin sections from the Moretown Formation in Western Massachusetts

showing different stages of crenulation cleavage development. These three areas are equivalent to stages 1, 3 and 4 of the Bell and Rubenach sequence (Figure 4.2).

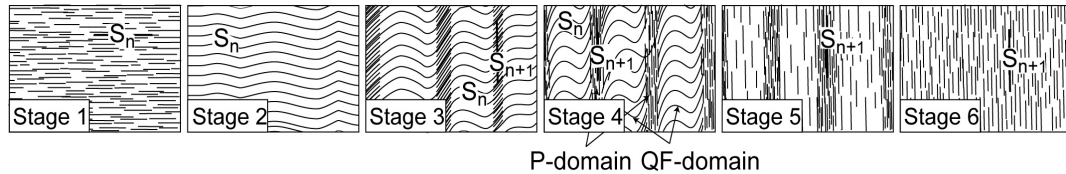


Figure 4.1. Six stages of crenulation cleavage development. At stage 1 the original S_n foliation is present, which becomes crenulated at stage 2. At stage 3 the crenulation process is accompanied by solution/precipitation-facilitated metamorphic differentiation. At stage 4 new phyllosilicates begin to grow parallel to S_{n+1} . Stage 5 represents a spaced cleavage with no relic S_n in the QF-domains, and eventually this fabric becomes “homogenized” at stage 6. The sample maps shown in Figures 4.3-4.5 are characterized by stages 1, 3, and 4 of crenulation cleavage development. Modified from Bell and Rubenach (1983).

We use crystallographic orientation maps to derive seismic wave velocities. Optical or x-ray techniques can be applied to obtain crystallographic orientation data from polished thinsections, but electron backscatter diffraction (EBSD) is a method that has gained popularity over recent years (e.g., Mauler et al., 2000; Bascou et al., 2001; Lloyd and Kendall, 2005; Valcke et al., 2006). Several methods can be used to calculate the bulk stiffness properties from these orientation data. The Voigt and Reuss averages are the simplest and best-known averaging techniques for obtaining estimates of the effective elastic properties of polymineralic samples (Mainprice, 2007). Although the means of these bounds appear to give reliable results in many cases, they are mathematical averages that have no additional physical significance. The shapes and spatial distributions of grains contribute to the elastic properties of a bulk rock sample (e.g., Bunge et al., 2000; Wendt et al., 2003; Naus-Thijssen et al., in press), but are not taken accounted for when using these averages. In order to account for these microstructural features we use a numerical method based on asymptotic expansion homogenization (AEH) and finite element (FE) analysis (e.g., Guedes and Kikuchi, 1990; Fish and Wagiman, 1992; Vel and Goupee, 2010;

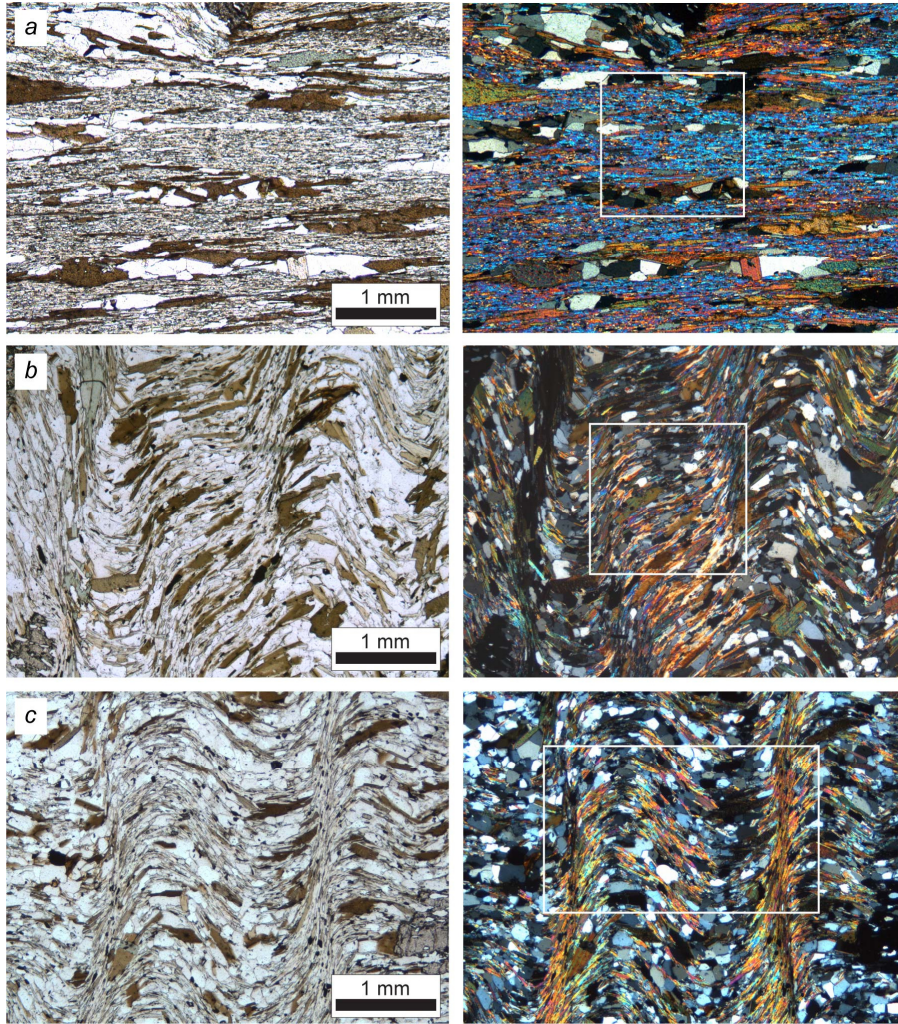


Figure 4.2. Photomicrographs (in plane and crossed polarized light) of sample areas *a*, *b*, and *c*. The box indicates the region from which the EBSD mineral orientation map is derived. The modal mineralogy of map *a* is 43.5% muscovite, 14.6% biotite, 28.3% quartz, and 13.6% plagioclase. The modal mineralogy of map *b* is 47.6% muscovite, 17.9% biotite, 23.1% quartz, and 11.4% plagioclase. The modal mineralogy of map *c* is 41.1% muscovite, 11% biotite, 34.3% quartz, and 13.6% plagioclase.

Naus-Thijssen et al., in press) to calculate the bulk stiffness tensor of the above-mentioned samples with different stages of crenulation cleavage development.

After describing the sample locality, we discuss the difficulties in obtaining reliable EBSD mineral orientation maps for phyllosilicate-rich rocks. We then present the homogenized stiffness tensors and the wave velocities for different stages of crenulation cleavage development and compare them to the stiffnesses and wave velocities calculated based on the Voigt and Reuss

averages. There are some differences between the analytical and AEH-FE results that reflect the fact that the AEH-FE method explicitly accounts for the microstructural contribution to the stiffness, but overall the velocity profiles show that the pervasive planar foliation and stage-3 crenulation cleavage have a much stronger anisotropy than the stage-4 crenulation cleavage. Finally, we discuss some implications of our findings for the interpretation of seismic anisotropy.

4.3. Samples

Amphiboles and micas are thought to control middle- to lower-crustal seismic anisotropy (Kitamura, 2006; Mahan, 2006; and references therein). We chose to investigate a microstructure, namely crenulation cleavage, in which micas defines the overall fabric of the rock. For this study we have selected two samples from the Moretown Formation in western Massachusetts, USA, that show a range of crenulation cleavage development. The Moretown Formation is interpreted to be a forearc basin that was thrust onto Laurentia during the Ordovician, Taconic orogeny (Hatch and Stanley, 1988). The formation is characterized by interbedded schist and quartzite to greywacke layers, ranging in thickness from centimeters to meters. During the Acadian orogeny the dominant regional foliation was folded into upright to steeply-dipping westward verging folds (F3), with amplitudes of meters up to tens of meters (Hatch and Stanley, 1988; Williams et al., 2001). The F3 folds display a crenulation cleavage that is absent or only weakly developed on fold-limbs, becoming progressively better developed toward the fold hinges. We selected one sample from an F3 fold limb, and one from an F3 fold hinge. Map *a* is obtained from the fold limb sample and shows a pervasive planar foliation. Maps *b* and *c* are both obtained from the fold hinge sample, map *b* shows a moderately developed stage-3 crenulation cleavage, and map *c* shows a well-developed stage-4 crenulation cleavage (Figure 4.2). All maps have a similar modal mineralogy (Figure 4.2).

4.4. EBSD Orientation Mapping

Current methods for collecting crystallographic orientation data from (phyllosilicate-rich) rocks are: (1) optical microscopy employing a universal stage, (2) EBSD, (3) X-ray texture goniometry (van der Pluijm, 1994; Valcke et al., 2006), and (4) neutron diffraction (Ivanka et al., 2005). All four methods have been shown to give similar results (Ullemeyer et al., 2000). Ullemeyer et al. (2000) discussed the advantages and disadvantages of each method and concluded that the X-ray texture goniometry and neutron diffraction methods are more suitable for determining bulk rock textures (and thus ideal for calculating anisotropic physical properties of rocks) and that the single grain (universal stage and EBSD) methods are advantageous for the investigation of local fabrics and fabric-forming mechanisms. For this study we require a pixel-based microstructural map with each pixel representing a phase and an orientation (three Euler angles), therefore EBSD is the most appropriate method for our purposes.

EBSD is a scanning electron microscope technique that can be used for both phase identification and the analysis of crystallographic orientations in a sample. Electrons bombarding the sample diffract through the crystal lattice, generating a number of bands on a phosphor screen that each correlate to a set of lattice planes, with a width that correlates to the lattice spacing (Venables and Harland, 1973; Dingley, 1984; Adams et al., 1993; Goldstein et al., 2003). The bands together form an electron backscatter diffraction pattern (EBSP) that is characteristic of the phase and orientation of the crystal. EBSPs can be collected automatically over a predefined grid allowing the linkage of EBSD data to spatial position within a sample and thus creating a mineral orientation map.

Over the past ten years, the use of EBSD to obtain mineral orientation data in rock samples has increased markedly (Prior et al., 2009). The geologic literature is dominated by data from quartz, olivine, calcite, garnet, and pyroxenes. These minerals are relatively easy to index, have been shown to give reliable data, and are of particular interest in rock deformation studies (Prior et al., 2009). Phyllosilicates, on the other hand, are prone to misindexing and indexing

biased towards particular orientations, giving potentially unreliable LPO data (Valcke et al., 2006). The indexing problems are related to difficulties regarding sample preparation and their low crystal symmetry. Despite these issues, EBSD has recently been used successfully on phyllosilicate-rich rocks (Žák et al., 2008; Lloyd et al., 2009).

4.4.1. Sample Preparation

EBSD requires a sample surface free of mechanical defects. The difference in hardness between minerals makes polishing multiphase samples challenging. In a schist, for example, the phyllosilicates are softer than the surrounding quartz and feldspar grains. When using an automated polishing routine with a slurry on a rotating cloth lap pad, the phyllosilicate material is removed more quickly causing the grains to lose contact with the lap surface. When the grains lose contact, slurry material will accumulate in the gaps, causing the phyllosilicates to etch instead of polish while the harder minerals continue to polish. We polished our samples with progressively finer grades of diamond suspension down to 3 μm and alumina suspension down to 0.3 μm . For all of these stages we noticed that less relief was created when using flat polishing pads. We used the flat polishing pads for all stages except the final two (1 μm and 0.3 μm with alumina suspension). These were completed using a pad with a short nap, which appeared to give the phyllosilicates a better polish, despite the added relief. After the mechanical polishing stages, the samples were manually polished for several minutes with a 0.02 μm colloidal silica suspension.

The polishing routine described above was iteratively developed based on the quality of EBSPs. This procedure gave the best quality patterns when manually collecting EBSPs from biotite and muscovite grains, as well as providing the best Hough image quality maps when collecting automated data. The Hough image quality is a value that measures the contrast within an EBSD pattern. It is calculated by averaging the heights of the most prominent detected peaks

in the Hough transform. It is a good indicator of grain boundaries, and a qualitative indicator of localized plastic deformation (e.g., Wilkinson, 1991; Schwarzer et al., 2009). The image quality is influenced by atomic number, lattice condition, microscope settings and surface condition (i.e. quality of polish).

4.4.2. Data Acquisition

EBSD measurements were obtained using the EDAX-TSL EBSD detector on the Tescan Vega II Scanning Electron Microscope at the University of Maine's Department of Earth Sciences. Chemical analysis was performed simultaneously using EDAX Genesis Energy Dispersive Spectroscopy (EDS). The diffraction patterns were background corrected and processed using EDAX-TSL OIM Data Collection 5 software. The patterns were recorded at a working distance of 25mm, using 20 kV acceleration voltage and ~11nA beam current, with the uncoated sample tilted 20° to the incident beam. The maps were collected with a square grid at a step size of 2 μm. The minimum and maximum band detection numbers for indexing were set to 8 and 11, in order to maximize indexing results for the phyllosilicates. During the data acquisition the Hough peaks of each measured point were saved, making it possible to re-evaluate the orientation data. Hough peaks represent the bands in an EBSP and are computationally more economical to save than the entire pattern.

4.4.3. Data Processing

Post-acquisition processing of data is necessary to accurately identify phases, optimize the quality of the orientation data, and prepare the dataset for numerical analysis. The procedure we used involves a data filter based on chemistry, the optimization of indexing by customizing the structure file, and a cleanup routine based on confidence index (CI) of each point. We first use the algorithm of Nowell and Wright (2004) to identify phases from the compositional data. Indexing based on Hough peaks is then restricted to determining only the orientation of a mineral,

not its identity. Misindexing is mainly an issue for lower symmetry minerals. These minerals have a more continuous spectrum of inter-band angles inherent in their structure. Because of this, they can fit more than one set of lattice planes, causing higher levels of misindexing. When indexing low symmetry phases it is crucial to have an accurate structure file to index the derived patterns/Hough transforms. In an effort to optimize the structure files for muscovite and biotite, we hand-collected 20 to 30 EBSPs per phase per sample and determined what structure file from the TSL supplied structure files and American Mineralogical Crystal Structure database (<http://rruff.geo.arizona.edu/AMS/amcsd.php>) gave the best fits to our patterns. The structure files in these databases are obtained by X-ray diffraction and are not necessarily ideal for EBSD indexing, making refinement necessary. The best fitting structure files were refined by manually adding or removing appropriate lattice planes used in the indexing.

Due to locally poor polishing and other misindexing issues, EBSD maps typically are not 100% indexed. The presence of cracks or trace phases that are not included in the analysis also contribute to a map with non-indexed pixels. Because the derived maps are meshed to perform the AEH-FE analysis, these mis- or non-indexed points must be filled in a way that makes the resulting map as representative for the sample as possible. The cleanup routine we used to achieve this relies on the CI of the indexed points. TSL-OIM software uses a voting procedure to calculate the best indexing solution for a pattern. The CI compares the number of votes of the first two solutions, making it a measure of how likely it is that the first ranked solution is correct. A higher CI should therefore correspond to a better result. In some cases, however, the number of votes for the first two solutions can be exactly the same (usually due to pseudosymmetry), leading to a CI of 0, but not necessarily be a bad index.

After accounting for pseudosymmetry, by using a higher number of detected bands and using a pseudosymmetry cleanup routine, we apply the Grain CI Standardization routine, which changes the CI of all the points in a grain (a grain can be defined based on a minimum grain size (5 μ m diameter) and the grain tolerance angle (10 degrees)) to the maximum CI found among all

points belonging to the grain. This routine enables a point with a low CI, but an orientation similar to that of the surrounding measurements, to be distinguished from a point with a low CI where no correlation exists between that point and its neighbors. Next, a filtering routine replaces the orientation and CI of points with low CI values (lower than 0.03) with the orientation and CI of neighboring points with a high CI, and replaces single points with a low CI and significantly different orientation than its neighboring points with the orientation of the neighboring points. After this the resulting grains are filtered for pseudosymmetry and Grain CI Standardization again, followed by an iterative dilation routine to fill in the remaining gaps. The dilation routine acts on points that do not belong to grains but have neighboring points that do. If the majority of neighbors of such a point belong to the same grain it will change the orientation of that point to match that of the majority grain. If there is no majority grain, the orientation of the point is changed to match any of the neighboring points. In section 4.6 we show how each part of the cleanup routine changes the EBSD dataset and how the LPOs of the different phases are influenced from step to step.

4.5. Calculation of Bulk Elasticity Data

4.5.1. Voigt and Reuss Bounds

Several methods can be used to calculate the seismic properties of a rock aggregate from crystal orientation measurements. The Voigt and Reuss averages are the simplest and best-known averaging techniques for obtaining estimates of the effective elastic properties of polycrystalline samples (Mainprice, 2007). The Voigt and Reuss calculations assume, respectively, constant elastic strain and constant elastic stress among all grains in a composite material, leading to an averaged stiffness tensor that provides an upper and lower bound (Voigt, 1928; Reuss, 1929). The bounds become increasingly separated with increasing anisotropy (Mainprice and Humbert, 1994). Several means of the two bounds have been proposed, including the arithmetic mean or VRH average (Hill, 1952), the geometric mean (Matthies and Humbert, 1993), and generalized

mean (Ji et al., 2004). Comparisons between values obtained petrophysically and those calculated from grain-scale orientation data show that, depending on the rock type and fabric, the measured values are closest to either the Voigt (e.g., Peselnick et al., 1974; Seront et al., 1993) or both the Voigt and Reuss estimates (e.g., Barruol and Kern, 1996). Mainprice and Humbert (1994) found that the VRH and geometric mean estimates are very similar and both yield similar results to the more computationally intensive self-consistent methods (see also below).

Theoretical methods have been proposed that do take into consideration the elastic interaction of the individual grains with the background medium, including the self-consistent (e.g., Hill, 1965; Willis, 1977) and differential effective medium (e.g., Bruner, 1976) methods. Reviews and comparisons of a variety of theoretical methods can be found in Mainprice (1997), Wendt et al. (2003), and references in both. In general these methods are considered to be computationally too involved for practical application (Mainprice, 2007).

Mainprice (1990) developed a software program (ANIS_ang_PC, available online at ftp://www.gm.univ-montp2.fr/mainprice//CareWare_Unicef_Programs/) that calculates the bulk elastic properties based on the single-crystal elastic constants and the crystallographic orientation data for each mineral weighted according to its modal content. The software calculates the Voigt and Reuss bounds and their geometric and arithmetic means, based on an EBSD-derived input file. This software is widely used in the geological community to calculate seismic properties from different rock types and structures (e.g., Lloyd and Kendall, 2005; Valcke et al., 2006; Tatham et al., 2008; Lloyd et al., 2009), and in these cases the VRH is used as the averaging method.

We used ANIS_ang_PC to calculate the Voigt, Reuss and VRH averages for our three sample maps and calculated wave velocities from them using the Christoffel equation (Christoffel, 1877). We then compared these results to those obtained using the AEH-FE method. The comparison of the different methods is done in 2D velocity plots. 3D velocity plots were also created (also using Mainprice's software), but only for the AEH-FE results.

4.5.2. AEH-FE Method

A polycrystalline sample that is subjected to small deformations in the linear elastic regime will experience microscale displacement fluctuations that are proportional to the average macroscopic strains at any point (x, y) within the sample. The AEH method relates the 3 components of the microscale displacements at a point in the sample to the 6 average macroscopic strains using 18 location-dependent characteristic functions $\chi_i^{kl}(x, y)$. Because it is assumed that there is continuity of displacement across grain boundaries the characteristic functions are continuous functions. The 3D elastic equilibrium equations at the microscale, in conjunction with Hooke's law for anisotropic materials yield a system of partial differential equations for the characteristic functions $\chi_i^{kl}(x, y)$ which are solved using the finite element method (e.g., Cook et al., 2002). The entire EBSD map is discretized using a finite element mesh that conforms to the grain boundaries. Six-noded triangular elements with quadratic shape functions are used to obtain accurate results (Cook et al., 2002). Once the characteristic functions have been determined, the bulk elastic stiffnesses (C_{ijkl}^{AEH}) are obtained through volume or area (Y) integration as,

$$C_{ijkl}^{AEH} = \frac{1}{|Y|} \int_Y \left[C_{ijkl}(x, y) + \sum_{p,q=1}^3 C_{ijpq}(x, y) (\nabla \chi^{kl})_{pq} \right] dY \quad (4.1)$$

where C_{ijkl} are the components of the fourth-order stiffness tensor in the sample frame that are obtained from the single-crystal elastic stiffnesses and Euler angles through tensor transformation (Bond, 1943). The AEH expression for the bulk stiffness tensor consists of two terms in the integrand: the first term is the traditional Voigt bound and the second term, involving the 18 characteristic functions, is a correction to the Voigt bound that takes into account the grain scale interactions. For our calculations we project the grain boundaries of the 2D microstructures into the third dimension (the z coordinate direction).

The AEH-FE method has a strong mathematical basis and has been extensively validated in engineering and computational mechanics (Guedes and Kikuchi, 1990; Sanchez-Palencia, 1983; Vel and Goupee, 2010). A more detailed description of the method in a geological context can be found in Naus-Thijssen et al. (in press). The method assumes that the microstructural geometry is periodic. Although EBSD maps are not truly periodic, it is important to note that regardless whether the map is periodic at the microscale or not, periodic boundary conditions yield more accurate bulk stiffnesses than either displacement or traction boundary conditions (Terada et al., 2000; Jiang and Jasiuk, 2001).

The EBSD mineral orientation maps we used in this study are large (403,860, 563,250, and 577,289 data points for maps *a*, *b*, and *c* respectively) and contain considerable detail. The accuracy of a FE calculation depends on the quality of the FE mesh. In order to achieve a fine enough mesh for our calculations while simultaneously maintaining computational efficiency, the EBSD maps were subdivided into multiple smaller maps. The bulk stiffness of the entire sample was calculated by averaging the stiffnesses of the smaller maps. For our calculations, maps *a* and *b* were divided into 16 (4x4) separate maps and map *c* was divided into 18 (6x3) separate maps. Sensitivity analysis on the influence of subdividing a map as opposed to calculating the stiffnesses from the full map shows that the differences are negligible (see Appendix A).

4.5.3. Single Crystal Properties

All methods for obtaining the bulk stiffness of a rock sample depend on the elastic behavior of the individual constituent minerals. Phyllosilicates are highly elastically anisotropic. Muscovite for example is three times stiffer when compressed along its *a*- and *b*-axes versus its *c*-axis. Muscovite commonly has a monoclinic crystal symmetry that is defined by 13 independent elastic moduli. The elastic moduli C_{11} , C_{22} , C_{66} , and C_{12} are primarily dependent on the strong covalent bonding within the layers, whereas the remaining moduli (C_{33} , C_{44} , C_{55} , C_{13} , C_{15} , C_{23} ,

C_{25} , C_{35} , and C_{46}) are governed by the weaker interlayer bonds and are thus more sensitive to changes in temperature and pressure (McNeil and Grimsditch, 1993). All layer silicates are pseudo-hexagonal, and in early elasticity studies muscovite was treated as hexagonal with the x_3 elasticity axis being normal to the layering, and the x_1 axis parallel to one of the tetrahedral chain directions within the sheet (e.g. Aleksandrov and Ryzhova, 1961). However, most muscovites are monoclinic, with a few polytypes in the triclinic, orthorhombic, and trigonal systems. For our calculations, we used the matrix for muscovite provided by Vaughan and Guggenheim (1986). Because there is no stiffness tensor available for biotite that is based on a monoclinic crystal structure, we used a single crystal stiffness tensor that is based on hexagonal crystal symmetry in our calculations (Aleksandrov and Ryzhova, 1961). Quartz has a hexagonal structure with its c -axis parallel to x_3 and one of the a -axes parallel to x_1 . We used the single crystal data for quartz derived by McSkimin et al. (1965). The plagioclase An_{09} single crystal data used in our calculations (Aleksandrov et al., 1974) is based on a monoclinic system. All these single crystal properties were determined under ambient conditions. The single crystal elastic properties vary with changes in pressure and temperature, but data are not available for many minerals (Lloyd and Kendall, 2005; Mainprice et al., 2000).

4.6. Results

4.6.1 Cleanup Procedure

Obtaining reliable EBSD maps from phyllosilicate-rich rocks is challenging, not only because of difficulties in obtaining a good polish on the micas, but also because of misindexing issues. Because of these difficulties, considerable post-processing is required to generate a map that is useful for bulk elasticity calculations. In order to investigate the degree to which post-processing affects and possibly changes the EBSD data we compare mineral orientation maps and pole figures after different steps of post-processing. Figure 4.3 shows the orientation maps and a series of pole figures of (a) the raw EBSD data (these data are already filtered based on

composition), (b) the EBSD data after applying pseudosymmetry, the Grain CI Standardization routine and filtering out the low CI data points based on measurements from neighboring points, and (c) the final, cleaned EBSD data (after applying pseudosymmetry and Grain CI standardization again, followed by an iterative dilation routine) of map *a*. Figures 4.4 and 4.5 show the orientation maps and pole figures of the cleaned EBSD data of maps *b* and *c* respectively. Because of the variety of phyllosilicate orientations in map *c* we chose to display pole figures with both the orientations of all the points from the sample, and just the points from the P-domains of the crenulation cleavage.

The pole figures in figure 4.3 show that the cleanup routines eliminate scattered measurements and do not markedly change the overall orientations. The c^* -axes of the biotite and muscovite grains in these maps are oriented perpendicular to the foliation planes, as expected. Quartz and plagioclase (not shown) exhibit extremely weak LPOs in all three maps.

4.6.2. Calculation of Bulk Elastic Properties

We calculated the bulk elastic properties of three EBSD mineral orientation maps with different stages of crenulation cleavage development. The same EBSD orientation map data were used as input for both the ANIS_Ang_PC and AEH-FE analysis. The first calculates the Voigt and Reuss bounds based on modal mineralogy, whereas the latter uses a mesh for the finite element analysis. Meshing of the microstructure may lead to slight variations in calculated modal percentages, but sensitivity analysis regarding the mesh indicates that the variation is negligible (see Appendix A). The results for the C_{11} , C_{12} , C_{13} , C_{22} , C_{23} , C_{33} , C_{44} , C_{55} , and C_{66} stiffness moduli calculated with the different methods are shown in Figure 4.6. The Voigt and Reuss bounds indicate the maximum and minimum values of the stiffness and the VRH and AEH-FE values fall between the two bounds, as expected. From the calculated tensors, the wave velocities at incidence angles from 0 to 180 degrees (0 degrees is parallel to the y-axis in the maps, 90 degrees is parallel to the x-axis) were calculated and plotted in Figure 4.7.

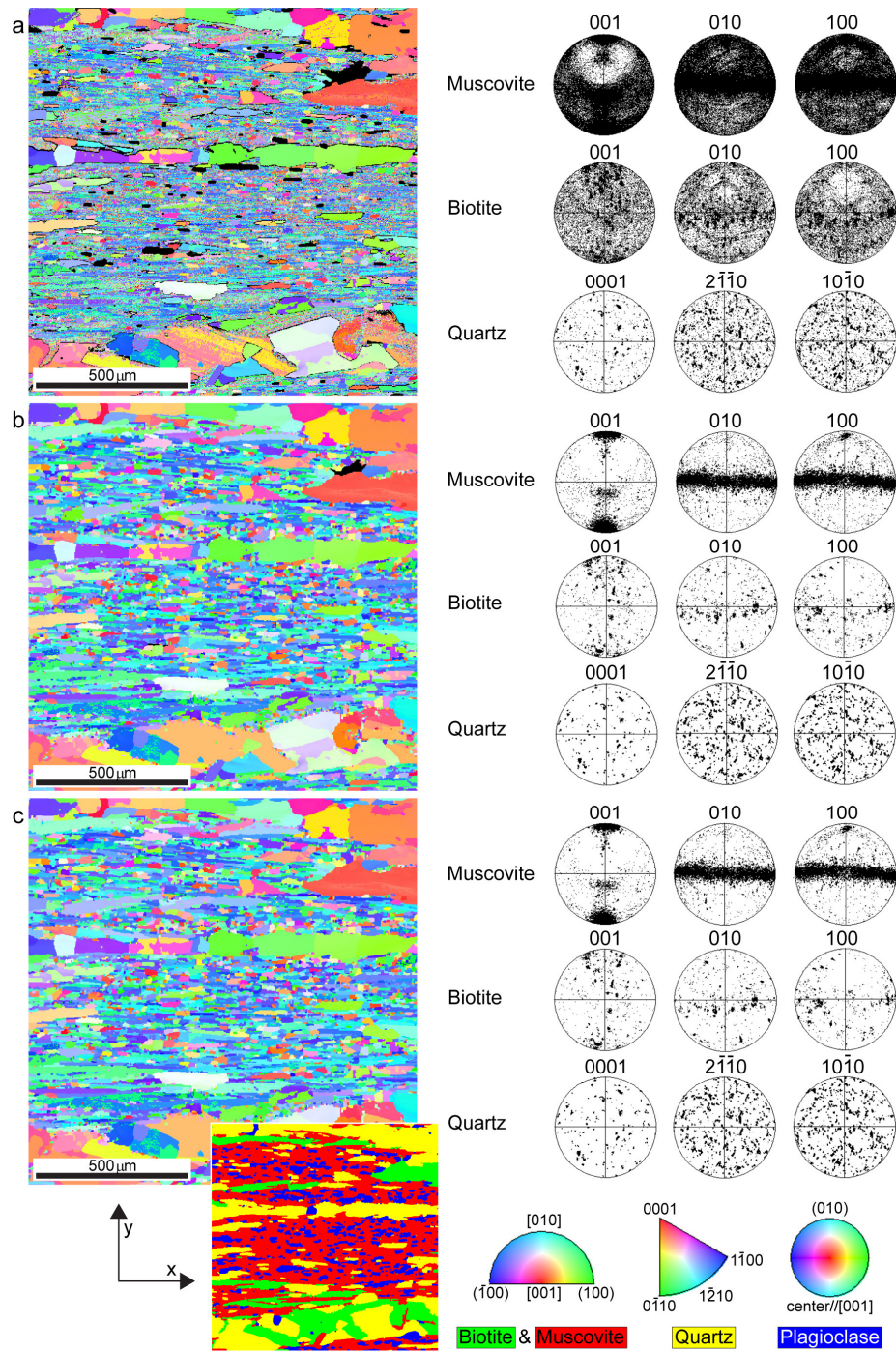


Figure 4.3. EBSD orientation maps and equal area, lower hemisphere pole figures of the main axes of biotite (c^* , b , a^*), muscovite (c^* , b , a^*), and quartz (c , a , and m) for map a . The inverse pole figure orientation map (left) and pole figures (right) of: (a) the raw EBSD data; (b) the EBSD data after applying pseudosymmetry, the Grain CI Standardization routine and filtering out the low CI data points based on measurements from neighboring points; and (c) the final, cleaned EBSD data (after applying pseudosymmetry and Grain CI standardization again, followed by an iterative dilation routine). The inset in map c shows a phase map of the cleaned data.

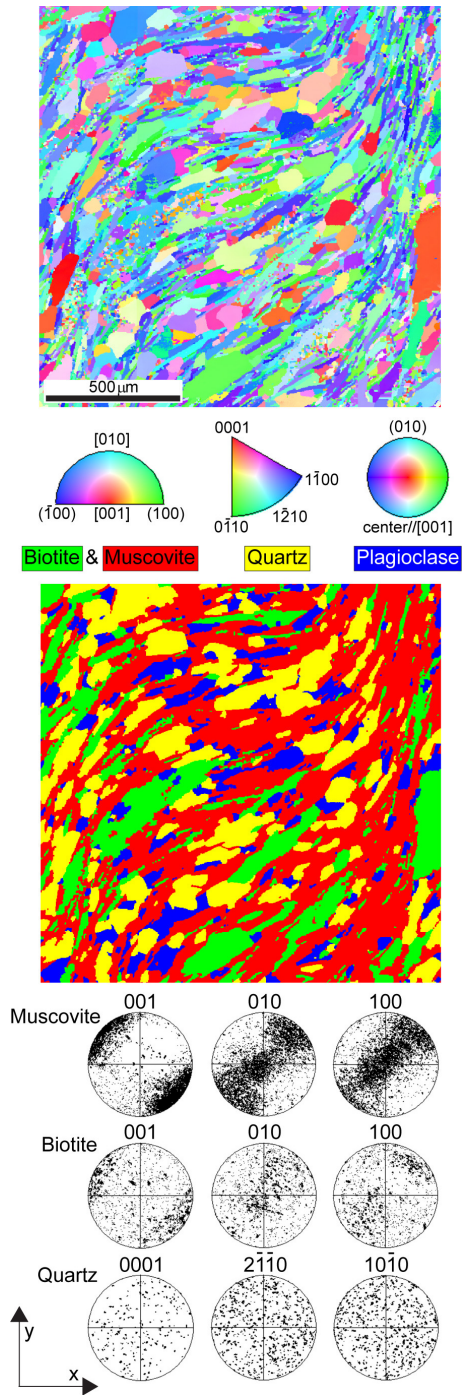


Figure 4.4. Cleaned EBSD data for map *b*. From top to bottom: the inverse pole figure orientation map; the phase map; and equal area, lower hemisphere pole figures of the main axes of biotite (c^* , b , a^*), muscovite (c^* , b , a^*), and quartz (c , a , and m).

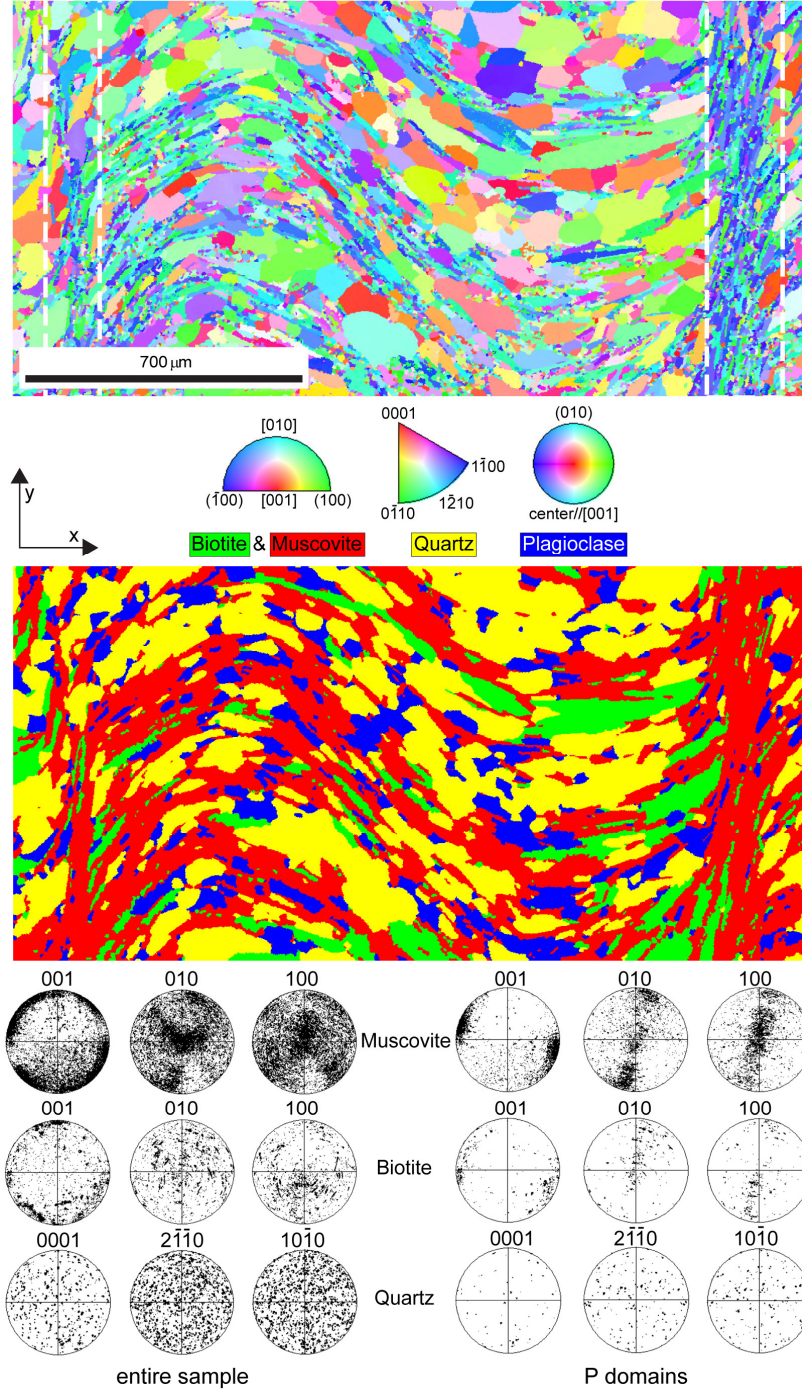


Figure 4.5. Cleaned EBSD data for map *c*. From top to bottom: the inverse pole figure orientation map; the phase map; and equal area, lower hemisphere pole figures of the main axes of biotite (c^* , b , a^*), muscovite (c^* , b , a^*), and quartz (c , a , and m). Pole figures are plotted for the entire map and for just the P-domains as outlined in the orientation map.

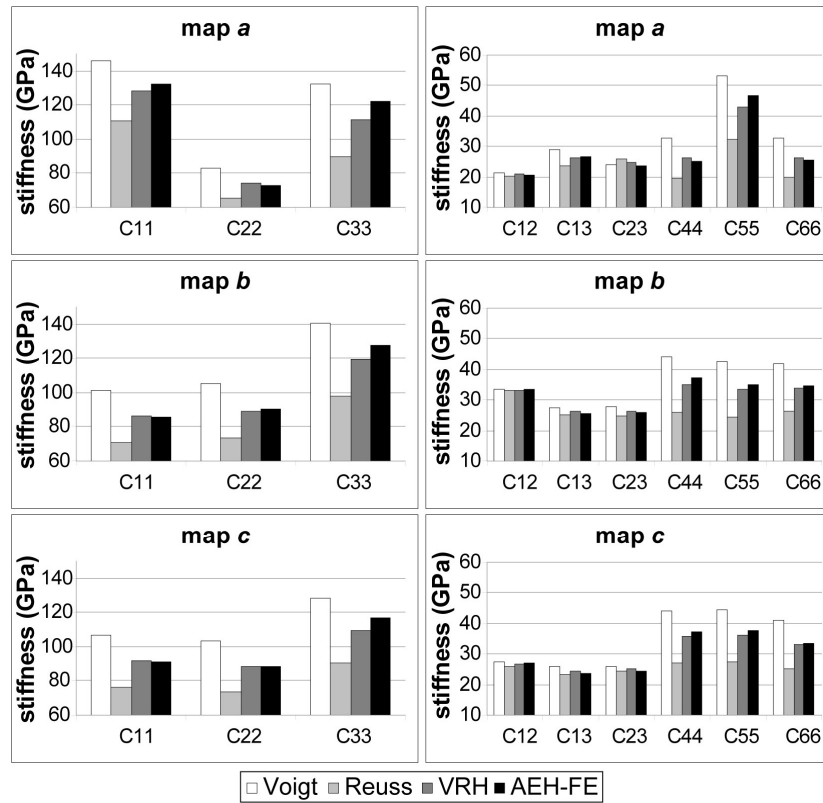


Figure 4.6. Comparison of the Voigt, Reuss, VRH, and AEH-FE stiffness components for the three mapped areas shown in Figures 4.3-4.5.

Map *a* shows a wide range of velocities at the different incidence angles, indicating strong seismic anisotropy. Map *b* gives a very similar result, but is slightly less anisotropic. Map *c* on the other hand gives very flat velocity curves indicating very weak bulk anisotropy. For all maps the VRH and AEH-FE solutions are slightly different. The difference is most marked in the anisotropic samples. The 3D P-wave velocities, percentage anisotropy of the S-waves, and the polarization planes of the fastest S-wave of the AEH-FE results for all maps are presented in Figure 4.8. The P-wave maxima evolve from lying in the equatorial plane of the velocity plot to an orthogonal orientation with progressive stages of crenulation cleavage development. Shear wave maxima and fast polarization directions diverge from the trajectories of bulk principal strain

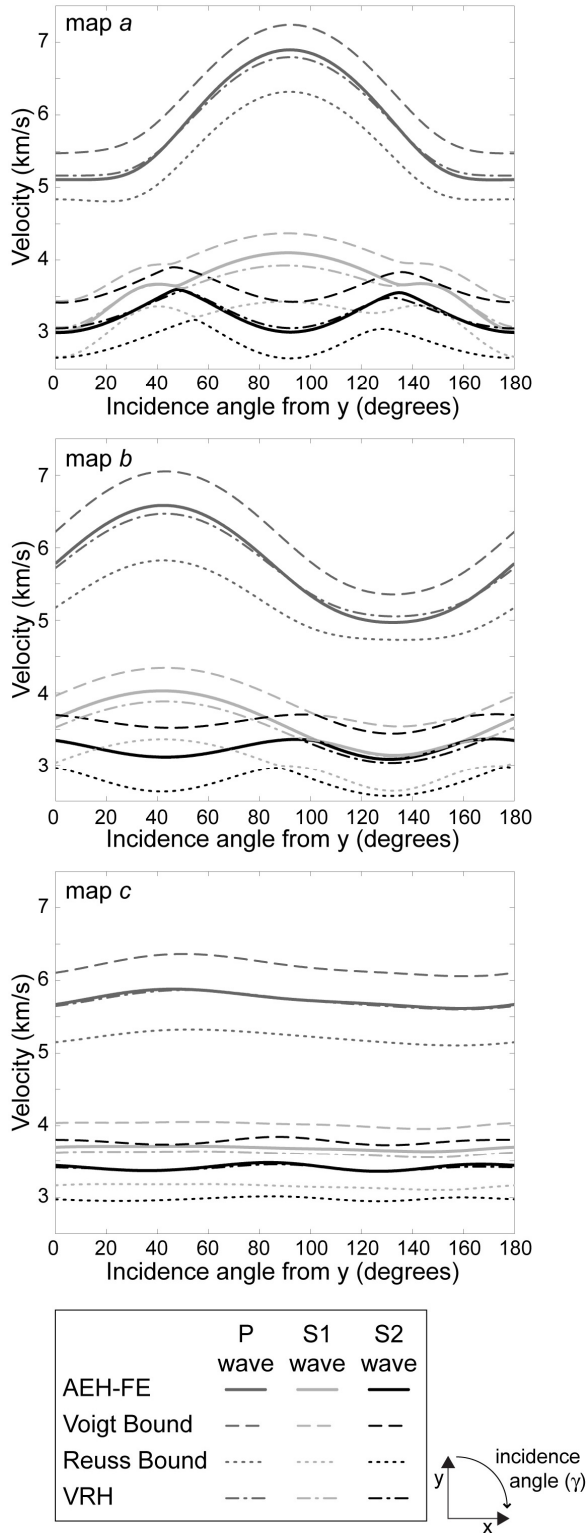


Figure 4.7. P and S velocities for the three mapped areas shown in Figures 4.3-4.5.

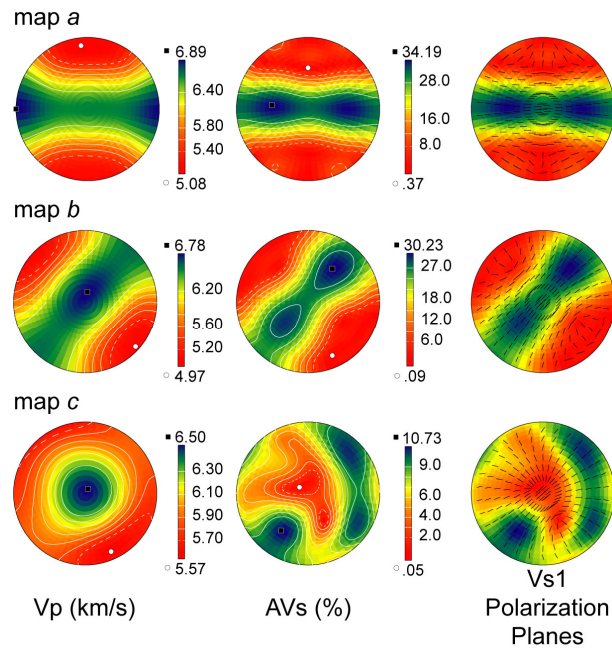


Figure 4.8. 3D velocity plots for the three mapped areas shown in Figures 4.3-4.5. From left to right, the P-wave velocities, percentage anisotropy of the S-waves, and the polarization planes of the fast S-wave (V_{s1}) with the AVs (=S-wave anisotropy) as the background. All plots are lower hemisphere. Corresponding maximum P- and S-wave anisotropies are shown in Table 4.1.

Table 4.1. Percentage maximum anisotropy for the P- and S- waves for the three mapped areas based on the 3D velocity calculations. The shaded values indicate the analytical results that are closest to the AEH-FE results. The final two lines show the differences between the two analytical means and the AEH-FE results.

| | sample a | | sample b | | sample c | |
|--|------------|------------|------------|------------|------------|------------|
| | $AV_P(\%)$ | $AV_S(\%)$ | $AV_P(\%)$ | $AV_S(\%)$ | $AV_P(\%)$ | $AV_S(\%)$ |
| AEH-FE | 30.3 | 34.19 | 30.9 | 30.23 | 15.5 | 10.73 |
| Voigt Bound | 28.3 | 26.21 | 28.4 | 24.97 | 12.6 | 8.54 |
| Reuss Bound | 27.4 | 32.8 | 22.8 | 31.99 | 12.5 | 10.66 |
| VRH | 27.8 | 28.77 | 25.9 | 27.61 | 12.5 | 8.95 |
| Geometric mean (GM) | 29.5 | 31.9 | 28.2 | 31.15 | 14.1 | 10.03 |
| $ (\text{AEH} - \text{VRH})/\text{AEH} *100$ | 8.3 | 15.9 | 16.2 | 8.7 | 19.4 | 16.6 |
| $ (\text{AEH} - \text{GM})/\text{AEH} *100$ | 2.6 | 6.8 | 8.7 | 3.0 | 9.0 | 6.5 |

axes or kinematic flow lines. The 3D velocity data show as well that maps *a* and *b* are much more anisotropic than map *c*, but map *c* is more anisotropic than can be gathered from the 2D plots of Figure 4.7. This is due to the lineation that developed in the crenulation cleavage sample and that does not lie in the x-y plane. The maximum percentage anisotropy for the P- and S-waves based on the 3D velocity plots are shown in Table 4.1. In this table we also included the values calculated using the geometric mean as an averaging method. The anisotropy values calculated using the VRH method all fall between the values calculated using the Voigt and Reuss bounds. However, the anisotropy values calculated using the AEH-FE method lie outside the Voigt and Reuss bounds in all but one instance. The geometric mean values are closer to the AEH-FE values than the VRH results are. The difference in percentage is up to 19.4% for the VRH results versus up to only 9% for the geometric mean results. However, for some cases the Voigt or Reuss average gives values that are closest to the AEH-FE result, illustrating that the variations among the AEH-FE and analytical methods are non-systematic.

4.7. Discussion

4.7.1. Sample preparation and Cleanup Procedure

The use of EBSD mineral orientation maps in studying seismic behavior of rocks is becoming easier with more workers having access to the necessary equipment, which is becoming increasingly faster and provides increasingly higher-resolution data. High symmetry minerals such as olivine and quartz are easy to index and give reliable orientation data. Phyllosilicates are more problematic, partly because of difficulties polishing the samples and partly because of the low symmetry crystal structure. With our polishing routine and post-processing procedure we were able to derive EBSD mineral orientation maps from phyllosilicate-rich rocks that are useful for calculating bulk elastic properties. Figure 4.3 shows the raw EBSD data for map *a* and how the cleanup routine affected the data. The cleanup routines eliminated scattered measurements and did not markedly change the orientation data. The c^* -axes of the biotite and muscovite grains

in the maps are oriented perpendicular to the foliation plane, as expected. Overall biotite was the most difficult mineral to index, giving the lowest CI values (commonly below 0.03) and in some cases patchy grains. The patchy grains overall had similar c^* -axis orientations, but varying a^* - and b -axis orientations, and could not be removed using the pseudosymmetry or other cleanup routines so they remain in the final maps. Also, even though most grains in the samples show no evidence for internal deformation, some of the larger biotite grains do (birds-eye extinction is visible when using light-microscopy), possibly causing some of the patchy orientations. Grains oriented with their c^* -axis roughly in the z -direction (perpendicular to the map plane) gave the best results (higher CIs and not patchy).

4.7.2. Calculation of Bulk Elastic Properties

The AEH-FE method was used to calculate bulk elastic stiffnesses and wave velocities from EBSD orientation maps derived from two phyllosilicate-rich samples with different stages of crenulation cleavage formation. The same orientation maps were used to calculate the Voigt and Reuss bounds and VRH average with ANIS_ang_PC. Both the AEH-FE derived data and the VRH solutions are bounded by the Voigt and Reuss bounds, but the two datasets show non-systematic variations in their stiffnesses and wave velocities (Figure 4.7). The percentage anisotropy appears to be underestimated by the Voigt, Reuss, geometric mean, and VRH methods in almost all cases (Table 4.1). Although previous workers have shown that bulk elastic properties of rocks derived with different types of theoretical analysis (including the Voigt and Reuss bounds and their averages) give comparable results to petrophysically derived data (e.g., Barruol and Kern, 1996; Wendt et al., 2003), the ultimate test for determining the accuracy of the AEH-FE method is to compare its results to experimental velocity measurements from the same rocks, although petrophysical data has its limitations as well. The AEH-FE and VRH velocities are within 5% of each other, which is the same accuracy found between experimental data and calculations based on the VRH model. However, the differences in P- and S-wave anisotropy that

arise from the relatively small velocity differences vary up to 19.4% (Table 4.1) and are probably large enough to justify the additional computation involved. A limitation of either method remains that the properties are calculated based on sparse single crystal data that are derived at room temperature and atmospheric pressure. Because the AEH-FE method is relatively easy to use and not as computationally involved as some theoretical methods (Mainprice, 2007), and explicitly accounts for the microstructural heterogeneity in a sample, it is the preferred method to use for evaluating anisotropic rocks such as schists.

4.7.3. Geological Implications

We studied the seismic behavior of three areas within two thin sections representing stages 1, 3, and 4 of crenulation cleavage development. Crenulation cleavage is a common microstructure in multiply-deformed crustal rocks, and thus an important structure to consider when interpreting crustal seismic data. The maps with the planar foliation and transitional crenulation cleavage show strong seismic anisotropy. In contrast, the map with the fully developed crenulation cleavage has a strong foliation (as illustrated by the pole figures of the P-domains of that map), but folding of the phyllosilicate-defined fabric in the QF-domains results in strongly muted bulk anisotropy. Similarly, Meltzer and Christensen (2001) demonstrated using petrophysics that quartzofeldspathic gneisses from the Nanga Parbat – Haramosh massif have different seismic anisotropies based on the orientations of the phyllosilicates. They found that in a thin section in which the biotites are segregated, elongated, and aligned parallel to one another the percentage anisotropy of the P wave is 12.5%, whereas the P-wave anisotropy in a sample with biotite grains that are more disseminated, equidimensional, and oriented at oblique angles is 2.72%. Their samples were compositionally very similar to one another, having an average modal mineralogy of 17% quartz, 54% plagioclase and 24% mica. Even though their rocks are less anisotropic because they contain less mica, they do show how fabrics and thus seismic wave velocities can vary from sample to sample in an Earth volume. Lloyd et al. (2009) also reported

variation in wave speed anisotropy in gneisses from the Nanga Parbat Massif, comparing single foliation rocks (C-planes) to rocks with multiple foliations (S-C fabrics). They used EBSD mapping to derive seismic properties of the rock. Their calculations gave maximum P- and S-anisotropies of 16.6% and 23.9% for the single foliation gneisses, versus only 5.8% and 7.5% respectively for the mixed foliation gneisses.

In addition to diluting the maximum value of seismic anisotropy, the development of crenulation cleavage has a profound effect on the geometry of the wave-speed distributions in relation to the kinematic reference frame. The P-wave maxima evolve from lying in the equatorial plane of the equal-area velocity plot to an orthogonal orientation parallel to the axes of the crenulations. Shear wave maxima and fast polarization directions diverge substantially from the trajectories of bulk principal strain axes or kinematic flow lines. The development of crenulation cleavage in a large crustal volume may thus lead to wave-speed geometries that appear to be at odds with a known or suspected kinematic reference frame, or may lead to the an incorrect interpretation of the kinematic reference frame. Lloyd et al. (2009) made similar observations in relation to S-C fabric development, concluding that variations in the orientations of fast polarization directions for shear waves deduced for different levels in the continental lithosphere may be difficult to interpret in terms of depth-varying deformation kinematics and tectonic decoupling.

The F3 folds from the Moretown formation show a well developed axial planar crenulation cleavage in the hinges, but a planar foliation in the limbs (Figure 4.9). This is typical of folded metapelitic schists, and our results indicate that the bulk seismic anisotropy of folded terranes will be determined by some combination of contribution from the limbs and contribution from the hinges of the folds. Depending on the shape and tightness of the larger-scale folds, it might be possible that the anisotropic limbs on opposite sides of the folds effectively cancel one another out, similar to the smaller-scale crenulations in the stage-4 map. In such an instance,

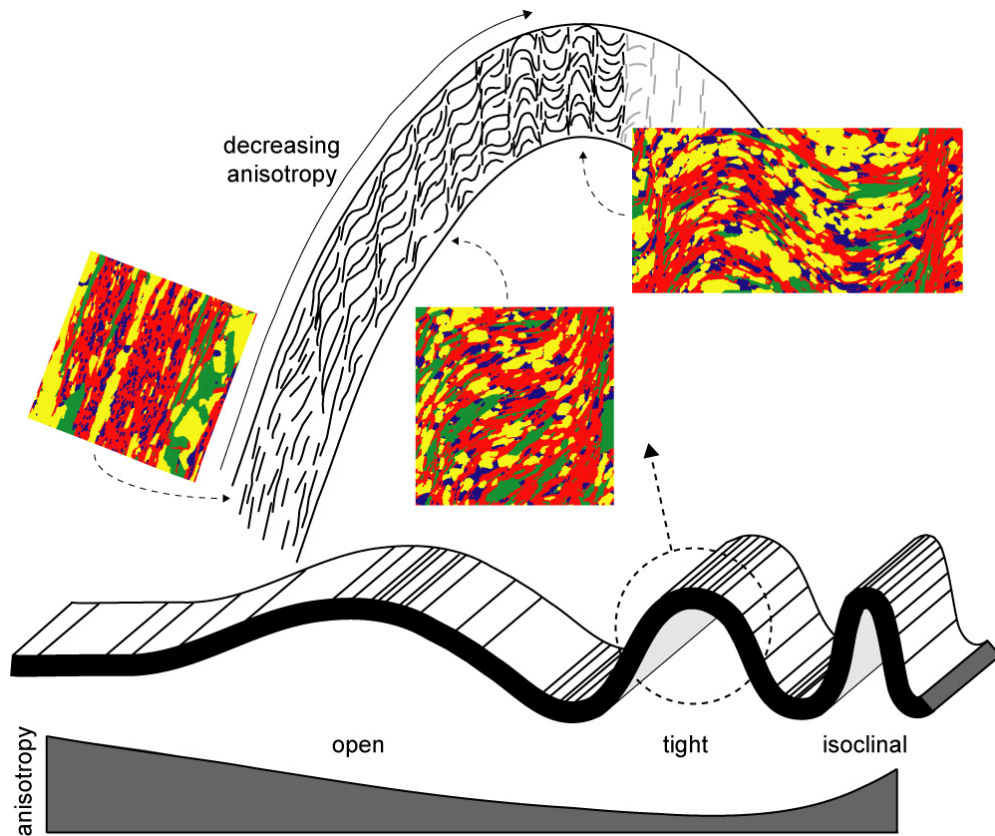


Figure 4.9. Influence of structure on seismic anisotropy from micro- to macroscale. The results regarding the influence on seismic anisotropy of the different structures related to crenulation cleavage at a microscale can be extrapolated to the meso- and macroscale as schematically shown in this figure (see explanation in text).

large crustal volume occupied by highly anisotropic rocks may appear nearly seismically isotropic. Projecting our results from the microscale folds to the meso- and macroscale shows a decrease in seismic anisotropy with increasing tightness of the fold, from gentle, to open, to close (Figure 4.9). Once the fold interlimb angle reaches a certain value, an increase of anisotropy is expected as the fold tightens, but with a velocity symmetry plane at right angles to the original, unfolded rock.

Significant teleseismic shear wave splitting is observed in the Southern Alps in New Zealand (e.g., Savage et al., 2007). This S-wave splitting is usually linked to deformation in the

mantle caused by the oblique continental collision that occurs in this region (e.g., Savage et al., 2007). Rock samples from the crust in the region are highly anisotropic, contributing to the idea that crustal rocks enhance the anisotropic seismic signal of the mantle (Okaya et al., 1995; Godfrey et al., 2000). Pulford et al. (2003) found that the crustal anisotropy of the Southern Alps is much smaller than expected and hypothesized that multiple stages of deformation caused the bulk crust to appear seismically isotropic. Bleibinhaus and Gebrande (2006) also recognized that large scale folding in the Swiss Alps altered the regional-scale symmetry and thus seismic responses. Our results are consistent with the work of both Bleibinhaus and Gebrande (2006) and Pulford et al. (2003), and show that when interpreting crustal seismic velocities it is important to consider variations in fabric within the geological volume being sampled.

4.8. Summary and Conclusions

We studied the seismic behavior of three phyllosilicate-rich areas within two samples that preserved different stages of crenulation cleavage development. Crystallographic orientation data from these rocks were obtained using EBSD mapping and these data were used to calculate bulk stiffness tensors and wave velocities. We show that EBSD orientation data can be collected, and orientation maps can be created from phyllosilicate-rich rocks when care is given to both the polishing of the samples and post-processing of the data. The bulk elastic properties and wave velocities calculated with the AEH-FE method are similar to those calculated from the VRH average, but the P- and S-wave anisotropies vary between the two methods by up to 19.4%. The geometric mean of the Voigt and Reuss bounds appears to give a more accurate result than the VRH average, compared to anisotropies calculated using the AEH-FE method. Because of the variations in anisotropy between the AEH-FE method and analytical methods, and because the latter methods have no explicit physical basis and do not account for microstructural features such as spatial distributions and grain shapes, the AEH-FE method is preferred. All three mapped areas have similar modal mineralogy and all show a strong foliation, but the large variation in

orientation of the phyllosilicates in the well-developed crenulation cleavage map leads to a strongly muted anisotropy compared to the mapped areas with the planar foliation and moderately developed crenulation cleavage. Development of crenulation cleavage also leads to a marked rotation of wave-speed elements such as the directions of P-wave maxima and fast S-wave polarization relative to the kinematic reference frame, which may complicate the interpretation of bulk kinematics from seismic wave-speed data. The development of large-scale folds in the continental crust may have similar effects and implies that care must be taken when interpreting seismic velocities within the crust.

REFERENCES

- Abbassi M.R., Mancktelow N.S., 1992. Single layer buckle folding in non-linear materials - I. Experimental study of fold development from an isolated initial perturbation. *Journal of Structural Geology* 14, 85-104.
- Adams B.L., Wright S.I., Kunze K., 1993. Orientation imaging: The emerge of a new microscopy. *Metallurgical Transactions A24*, 819-831.
- Aleksandrov K.S., Alchikov U.V., Belikov B.P., Zaslavski B.I., Krupnyi A.I., 1974. Velocities of elastic waves in minerals at atmospheric pressure and increasing precision of elastic constants by means of EVM. *Izvestiya Academia Science USSR Geological Series* 10, 15-24.
- Aleksandrov K.S., Ryzhova T.V., 1961. The elastic properties of rock-forming minerals, II: Layered silicates. *Bulletin Academia Science USSR Geophysical Series* 12, 871-875.
- Angel R.D., Allen D.R., Miletich R., Finger L.W., 1997. The use of quartz as an internal pressure standard in high-pressure crystallography. *Journal of Applied Crystallography* 30, 461-466.
- Auld, B.A., 1990. *Acoustic Fields and Waves in Solids*, vol 2, 2nd ed. Robert E Krieger Publishing Co, Malabar, FL, 432 p.
- Barruol G., Kern H., 1996. Seismic anisotropy and shear-wave splitting in lower-crustal and upper-mantle rocks from the Ivrea Zone - experimental and calculated data. *Physics of the Earth and Planetary Interiors* 95, 175-194.
- Bascou J., Barruol G., Vauchez A., Mainprice D., Egydio-Silvo M., 2001. EBSD-measured lattice-preferred orientations and seismic properties of eclogites. *Tectonophysics* 342, 61-80.
- Bass J.D., 1995. Elasticity of minerals, glasses, and melts. In: Ahrens T.J. (Ed.), *Mineral Physics and Crystallography; A Handbook of Physical Constants*, AGU reference shelf 2. American Geophysical Union, Washington, D.C., 45-63.
- Backus G.E., 1962. Long-wave elastic anisotropy produced by horizontal layering. *Journal of Geophysical Research* 67, 4427-4441.
- Bell T.H., Rubenach M.J., 1983. Sequential porphyroblast growth and crenulation cleavage development during progressive deformation. *Tectonophysics* 92, 171-194.
- Bell T.H., Rubenach M.J., Fleming P.D., 1986. Porphyroblast nucleation, growth, and dissolution in regional metamorphic rocks as a function of deformation partitioning during foliation development. *Journal of Metamorphic Geology* 4, 37-67.
- Bell T.H., Cuff C., 1989. Dissolution, solution transfer, diffusion versus fluid flow and volume loss during deformation or metamorphism. *Journal of Metamorphic Geology* 7, 425-447.

- Bell T.H., Hayward N., 1991. Episodic metamorphic reactions during orogenesis: the control of deformation partitioning on reaction sites and reaction duration. *Journal of Metamorphic Geology* 9, 619-640.
- Bensoussan, A., Lions, J.L., Papanicolaou, G., 1978. *Asymptotic Analysis for Periodic Structures*. North-Holland Publishing Co., Amsterdam, 724 p.
- Beran, M.J., 1968. *Statistical continuum theories*. John Wiley and Sons Interscience, New York, 424 p.
- Beran, M.J., Mason, T.A., Adams, B.L., Olsen, T., 1996. Bounding elastic constants of an orthotropic polycrystal using measurements of the microstructure, *Journal of the Mechanics and Physics of Solids* 44, 1543-1563.
- Biot M.A., 1957. Folding instability of a layered viscoelastic medium under compression. *Proceedings of the Royal Society of London A* 242, 444-454.
- Biot M.A., 1959. On the instability and folding deformation of a layered viscoelastic medium in compression. *Journal of Applied Mechanics* 26, 393-400.
- Biot M.A., 1961. Theory of folding of stratified viscoelastic media and its implications in tectonics and orogenesis. *Geological Society of America Bulletin* 72, 1595-1620.
- Biot M.A., 1964. Theory of internal buckling of a confined multilayered structure. *Geological Society of America Bulletin* 75, 563-564.
- Birch, F., 1960. The velocity of compressional waves in rocks to 10 kilobars, part 1, *Journal of Geophysical Research* 65, 1083-1102.
- Birch, F., 1961. The velocity of compressional waves in rocks to 10 kilobars, part 2, *Journal of Geophysical Research* 66, 2199-2224.
- Bjørkum P.A., 1996. How important is pressure in causing dissolution of quartz in sandstones. *Journal of Sedimentary Research* 66, 147-154.
- Bleibinhaus F., Gebrande H., 2006. Crustal structure of the Eastern Alps along the TRANSALP profile from wide-angle seismic tomography. *Tectonophysics* 414, 51-69.
- Boggs S., Kwon Y.I., Goles G.G., Rusk B.R., Kringsley D., Seyedolali A., 2002. Is quartz cathodoluminescence color a reliable provenance tool? A quantitative examination. *Journal of Sedimentary Research* 72, 408-415.
- Boggs S.J., Kringsley D., 2006. *Application of Cathodoluminescence Imaging to the study of sedimentary Rocks*. Cambridge University Press.
- Bond, W.L., 1943. The mathematics of the physical properties of crystals, *Bell System Technical Journal* 22, 1-72.
- Bosworth W., 1981. Strain-induced preferential dissolution of halite. *Tectonophysics* 78, 509-525.

- Bruner W.M., 1976. Comments on "Seismic velocities in dry and saturated cracked solids". *Journal of Geophysical Research* 81, 2573-2576.
- Bunge H.J., Kiewel R., Reinert T., Fritsche L., 2000. Elastic properties of polycrystals - influence of texture and stereology. *Journal of the Mechanics and Physics of Solids* 48, 29-66.
- Carlson W.D., Gordon C.L., 2004. Effects of matrix grain size on the kinetics of intergranular diffusion. *Journal of Metamorphic Geology* 22, 733-742.
- Champion, M.E., White, N.J., Jones, S.M., Priestley, K.F., 2006. Crustal velocity structure of the British Isles; a comparison of receiver functions and wide-angle seismic data, *Geophysical Journal International*, 166, 795–813.
- Christensen, N.I., 1965. Compressional wave velocities in metamorphic rocks at pressures to 10 kilobars, *Journal of Geophysical Research*, 70, 6147-6164.
- Christensen, N.I., 1966. Shear wave velocities in metamorphic rocks at pressures to 10 kilobars, *Journal of Geophysical Research* 71, 3549-3556.
- Christensen N.I., 1985. Measurements of dynamic properties of rock at elevated temperatures and pressures. In: Pincus H.J. & Hoskins E.R. (Eds.), *Measurements of Rock Properties at Elevated Pressures and Temperatures*, ASTM STP 869. American Society for Testing and Materials, Philadelphia, 93-107.
- Christensen N.I., Mooney W.D., 1995. Seismic velocity structure and composition of the continental crust: A global view. *Journal of Geophysical Research* 100, 9761-9788.
- Christoffel E.B., 1877. *Über die Fortpflanzung von Stößen durch elastische feste Körper*. *Annali di Matematica Pura ed Applicata* 8, 193-243.
- Cobbold P.R., Cosgrove J.W., Summers J.M., 1971. Development of internal structures in deformed anisotropic rocks. *Tectonophysics* 12, 23-53.
- Comodi P., Zanazzi P.F., 1995. High-pressure structural study of muscovite. *Physics and Chemistry of Minerals* 22, 170-177.
- Cook R.D., Malkus D.S., Plesha M.E., Witt R.J., 2002. *Concepts and Applications of Finite Element Analysis*, 4th ed. John Wiley & Sons, Inc., Hoboken, NJ.
- Cosgrove J.W., 1976. The formation of crenulation cleavage. *Journal of the Geological Society of London* 132, 155-178.
- Cox S.F., Etheridge M.A., 1989. Coupled grain-scale dilatancy and mass transfer during deformation at high fluid pressures: examples from Mount Lyell, Tasmania. *Journal of Structural Geology* 11, 147-162.
- Crampin S., 1981. A review of wave motion in anisotropic and cracked elastic-media. *Wave Motion* 3, 343-391.

- Demars, C., Pagel, M., Deloule, E., Blanc, P., 1996. Cathodoluminescence of quartz from sandstones: Interpretation of the UV range by determination of trace element distributions and fluid-inclusion P-T-X properties in authigenic quartz. *American Mineralogist* 81, 891-901.
- Desai C.S., Abel J.F., 1972. *Introduction to the Finite Element Method*. Van Nostrand Reinhold Company, New York.
- Dieterich J.H., Carter N.L., 1969. Stress-history of folding. *American Journal of Science* 267, 129-154.
- Dingley D.J., 1984. Diffraction from sub-micron areas using electron backscatter diffraction in a scanning electron microscope. *Scanning Electron Microscopy* 2, 269-575.
- Drugan W.J., Willis J.R., 1996. A micromechanics-based nonlocal constitutive equation and estimates of representative volume element size for elastic composites. *Journal of the Mechanics and Physics of Solids* 44, 497-524.
- Dupee M.E., 2005. Porphyroblast kinematics and crenulation cleavage development in the aureole of the Mooselookmeguntic Pluton, Western Maine. MSc. Thesis, University of Maine, Orono, Maine, USA.
- Durney D.W., 1972. Solution-transfer, an important geological deformation mechanism. *Nature* 235, 315-317.
- Durney D.W., 1978. A theory of mass-transfer-buckling deformation in finite amplitude sinusoidal multilayers. In: Easterling K.E. (Ed.), *Proceedings of the interdisciplinary conference held at the University of Lulea, Sweden, Sept 1978.* , 393-405.
- Dutrow B., Norton, D., 1995. Evolution of fluid pressure and fracture propagation during contact metamorphism. *Journal of Metamorphic Geology* 13. 677-686.
- Erslev E.A., 1998. Limited, localized nonvolatile element flux and volume change in Appalachian slates. *The Geological Society of America Bulletin* 110, 900-915.
- Etheridge M.A., 1973. Experimentally produced slaty and crenulation cleavages during a single deformation. *Journal of the Geological Society of Australia* 20, 223-227.
- Etheridge M.A., Hobbs B.E., 1974. Chemical and deformational controls on recrystallization of mica. *Contributions to Mineralogy and Petrology* 43, 111-124.
- Evans J., Hogg A.J.C., Hopkins M.S., Howarth R.J., 1994. Quantification of quartz cements using combined SEM, CL, and image analysis. *Journal of Sedimentary Research* A64, 334-338.
- Fish J., Wagiman A., 1992. Multiscale finite element method for a periodic and nonperiodic heterogeneous medium. In: *Adaptive, Multilevel, and Hierarchical Computational Strategies*, vol.157. American Society of Mechanical Engineers, Applied Mechanical Division, 95-117.

- Frehner M., Schmalholz S.M., 2006. Numerical simulations of parasitic folding in multilayers. *Journal of Structural Geology* 28, 1647-1657.
- Gaft M., Reisfeld R., Panczer G., 2005. *Luminescence Spectroscopy of Minerals and Materials*. Springer Verlag, Berlin.
- Godfrey N.J., Christensen N.I., Okaya D.A., 2000. Anisotropy of schists: Contribution of crustal anisotropy to active source seismic experiments and shear wave splitting observations. *Journal of Geophysical Research* 105, 27991-28007.
- Goldstein A., Pickens J., Klepeis K., Linn F., 1995. Finite strain heterogeneity and volume loss in slates of the Taconic Allochthon, Vermont, USA. *Journal of Structural Geology* 17, 1207-1216.
- Goldstein A., Knight J., Kimball K., 1998. Deformed graptolites, finite strain and volume loss during cleavage formation in rocks of the taconic slate belt, New York and Vermont, USA. *Journal of Structural Geology* 20, 1769-1782.
- Goldstein J., Newbury D., Joy D., Lyman C., Echlin P., Lifshin E., Sawyer L., Michael J., 2003. *Scanning Electron Microscopy and X-Ray Microanalysis*, 3rd edition. Kluwer Academic.
- Götze J., Plötze M., Habermann D., 2001. Origin, spectral characteristics and practical applications of the cathodoluminescence (CL) of quartz - a review. *Mineralogy and Petrology* 71, 225-250.
- Goupee A.J., Vel S.S., 2010. Multiscale thermoelastic analysis of random heterogeneous materials. Part II: Direct micromechanical failure analysis and multiscale simulations. *Computational Materials Sciences* 48, 39-53.
- Gray D.R., 1977a. Morphological classification of crenulation cleavage. *Journal of Geology* 85, 229-235.
- Gray D.R., 1977b. Some parameters which affect the morphology of crenulation cleavages. *Journal of Geology* 85, 763-780.
- Gray D.R., Durney D.W., 1979. Crenulation cleavage differentiation: implications of solution-deposition processes. *Journal of Structural Geology* 1, 73-80.
- Green II H.W., 1972. Metastable growth of coesite in highly strained quartz. *Journal of Geophysical Research* 77, 2478-2482.
- Guedes J.M., Kikuchi N., 1990. Preprocessing and postprocessing for materials based on the homogenization method with adaptive finite element methods. *Computer Methods in Applied Mechanics and Engineering* 83, 143-198.
- Guidotti C.V., Sassi F.P., Comodi P., Zanazzi P.F., Blencoe J.G., 2005. Slaty cleavage: Does the crystal chemistry of layer silicates play a role in its development? *The Canadian Mineralogist* 43, 311-325.
- Gusev A.A., 1997. Representative volume element size for elastic composites: a numerical study. *Journal of the Mechanics and Physics of Solids* 45, 1449-1459.

- Hatch N.L., Stanley R.S., 1988. Post-Taconian structural geology of the Rowe-Hawley zone and the Connecticut Valley belt west of the Mesozoic basins. In: *The Bedrock Geology of Massachusetts*. USGS, Washington, DC, C1-C36.
- Hearmon, R.F.S., 1979. The elastic constants of crystals and other anisotropic materials, in: Hellwege, K.H., Hellwege, A.M. (Eds.), *Landolt-Börnstein Tables*, III/18. Springer-Verlag, pp.1-244.
- Higham, N.J., 2008, *Functions of matrices: Theory and computation*, Society for Industrial & Applied Mathematics, 445 p.
- Hill R., 1952. The elastic behaviour of a crystalline aggregate. *Proceedings of the Physical Society of London, Section A* 65, 349-354.
- Hill R., 1965. A self-consistent mechanics of composite materials. *Journal of the Mechanics and Physics of Solids* 13, 213-222.
- Hirth G., Tullis J., 1994. The brittle-plastic transition in experimentally deformed quartz aggregates. *Journal of Geophysical Research* 99, 11731-11747.
- Hobbs B.E., 1968. Recrystallization of single crystals of quartz. *Tectonophysics* 6, 353-401.
- Hobbs B.E., Means W.D., Williams P.F., 1976. *An Outline of Structural Geology*. John Wiley & Sons, Inc., New York.
- Hobbs B.E., Mühlhaus H.B., Ord A., Zhang Y., Moresi L., 2000. Fold geometry and constitutive behaviour. In: Jessell M.W. & Urai J.L. (Eds.), *Stress, Strain and Structure*, A volume in honour of WD Means. *Journal of the Virtual Explorer* (online).
- Hobbs B., Regenauer-Lieb K., Ord A., 2008. Folding with thermal-mechanical feedback. *Journal of Structural Geology* 30, 1572-1592.
- Houseknecht D.W., 1988. Intergranular pressure solution in four quartzose sandstones. *Journal of Sedimentary Petrology* 58, 228-246.
- Hughes, T.J.R., 2000. *The finite element method: Linear static and dynamic finite element analysis*. Dover Publications. 672 p.
- Ivanka T.I., Kern H.M., Nikitin A.N., 2005. Directional dependence of P- and S-wave propagation and polarization in foliated rocks from the Kola Superdeep well: Evidence from laboratory measurements and calculations based on TOF neutron diffraction. *Tectonophysics* 407, 25-42.
- Ji, S., Wang, Q., Xia, B., 2002. *Handbook of Seismic Properties of Minerals, Rocks and Ores*, Polytechnic International Press, Canada, 630 p.
- Ji S., Wang Q., Xia B., Marcotte D., 2004. Mechanical properties of multiphase materials and rocks: a phenomenological approach using generalized means. *Journal of Structural Geology* 26, 1377-1390.

- Jiang M., Jasiuk I., 2001. Scale and boundary conditions effects in elastic properties of random composites. *Acta Mechanica* 148, 63-78.
- Joesten R., 1991. Grain-boundary diffusion kinetics in silicate and oxide minerals. In: Ganguly J. (Ed.), *Diffusion, atomic ordering, and mass transport, selected topics in Geochemistry*. Springer Verlag, 345-395.
- Johnson A.M., Fletcher R.C., 1994. *Folding of Viscous Layers*. Columbia University Press, New York.
- Johnson J.E., Christensen N.I., 1995. Seismic anisotropy of shales. *Journal of Geophysical Research* 100, 5991-6003.
- Johnson S.E., Vernon R.H., Upton P., 2004. Foliation development and progressive strain-rate partitioning in the crystallizing carapace of a tonalite pluton: microstructural evidence and numerical modeling. *Journal of Structural Geology* 26, 1845-1865.
- Johnson S.E., Dupee M.E., Guidotti C.V., 2006. Porphyroblast rotation during crenulation cleavage development: an example from the aureole of the Mooselookmeguntic pluton, Maine, USA. *Journal of Metamorphic Geology* 24, 55-73.
- Johnson S.E., Jin Z., Naus-Thijssen F.M.J., Koons P.O., 2010. Coupled deformation and metamorphism in the roof of a tabular mid-crustal igneous complex. *Bulletin of the Geological Society of America* (in press).
- Kaneshima S., Ando M., Kimura S., 1988. Evidence from shear-wave splitting for the restriction of seismic anisotropy to the upper crust. *Nature* 335, 627-629.
- Kanit T., Forest S., Galliet I., Mounoury V., Jeulin D., 2003. Determination of the size of the representative volume element for random composites: statistical and numerical approach. *International Journal of Solids and Structures* 40, 3647-3679.
- Karato S., 1987. Seismic anisotropy due to lattice preferred orientation of minerals: Kinematic or dynamic?. In: Manghnani M.H. & Syono Y. (Eds.), *High-Pressure Research in Mineral Physics*. American Geophysical Union, Washington, D.C., 455-471.
- Karato S., Forte A.M., Liebermann R.C., Masters G., Stixrude L., 2008. Introduction: Probing Earth's deep interior. In: Karato S., Forte A.M., Liebermann R.C., Masters G. & Stixrude L. (Eds.), *Earth's Deep Interior, Mineral Physics and Tomography, From the Atomic to the Global Scale*. Geophysical Monograph 117, American Geophysical Union, Washington, DC, 1-2.
- Karato S., Jung H., Katayama I., Skemer P., 2008. Geodynamic significance of seismic anisotropy of the upper mantle: New insights from laboratory studies. *Annual Review of Earth and Planetary Sciences* 36, 59-95.
- Karato S.I., 2008. *Deformation of Earth Materials, An Introduction to the Rheology of Solid Earth*. Cambridge University Press, New York.
- Kitamura K., 2006. Constraint of lattice-preferred orientation (LPO) on V_p anisotropy of amphibole rich rocks. *Geophysical Journal International* 165, 1058-1065.

- Koons P.O., Craw D., Cox S.C., Upton P., Templeton A.S., Chamberlain C.P., 1998. Fluid flow during active oblique convergence: A Southern Alps model from mechanical and geochemical observations. *Geology* 26, 159-162.
- Kramer M.J., Seifert K.E., 1991. Strain enhanced diffusion in feldspars. In: Ganguly J. (Ed.), *Diffusion, atomic ordering, and mass transport, selected topics in Geochemistry*. Springer Verlag, 286-303.
- Langer S.A., Reid A.C.E., Haan S.I., Garcia R.E., Lua R.C., Coffman V.R., 2008. The OOF2 Manual, Revision 3.7 for OOF2 Version 2.0.4 .
- Lloyd G.E., Butler R.W.H., Casey M., Mainprice D., 2009. Mica, deformation fabrics and the seismic properties of the continental crust. *Earth and Planetary Science Letters* 288, 320-328.
- Lloyd G.E., Kendall J.M., 2005. Petrofabric derived seismic properties of a mylonitic quartz simple shear zone: implications for seismic reflection profiling. In: Harvey P.K., Brewer T.S., Pezard P.A. & Petrov V.A. (Eds.), *Petrophysical Properties of Crystalline Rocks*. Geological Society Special Publication 240, 75-94.
- Lloyd G.E., Law R.D., Mainprice D., 2010. Predicting seismic properties from three-dimensional microstructures - a new look at an old quartzite. In: Law R.D., Butler R.W.H., Holdsworth R., Krabbendam M. & Strachan R. (Eds.), *Continental Tectonics and Mountainbuilding - The Legacy of Peach and Horne* . Special Publication 335, Geological Society, London, 603-622.
- Logan D.L., 2007. *A First Course in the Finite Element Method*. Thomson, Toronto.
- Love G., Scott V.D., 1978. Evaluation of a new correction procedure for quantitative electron probe analysis . *Journal of Physics D: Applied Physics* 11, 1369-1376.
- Mahan K., 2006. Retrograde mica in deep crustal granulites: Implications for crustal seismic anisotropy. *Geophysical Research Letters* 33, L24301, oi:10.1029/2006GL028130.
- Mainprice D., 1990. A Fortran program to calculate seismic anisotropy from the lattice preferred orientation of minerals. *Computers and Geosciences* 16, 385-393.
- Mainprice D., 1997. Modelling anisotropic seismic properties of partially molten rocks found at mid-ocean ridges. *Tectonophysics* 279, 161-179.
- Mainprice D., 2007. Seismic anisotropy of the deep Earth from a mineral and rock physics perspective. In: Schubert G. & Bercevicci D. (Eds.), *Treatise on Geophysics*, volume 2. Elsevier, 437-491.
- Mainprice D., Humbert M., 1994. Methods of calculating petrophysical properties from lattice preferred orientation data. *Surveys in Geophysics* 15, 575-592.
- Mainprice, D., Nicolas, A., 1989. Development of shape and lattice preferred orientations: application to the seismic anisotropy of the lower crust, *Journal of Structural Geology*, 11, 175-189.

- Mainprice D., Barruol G., Ben Ismaïl W., 2000. The seismic anisotropy of the earth's mantle: from single crystal to polycrystal. In: Karato S.I., Forte A.M., Liebermann R.C., Masters G. & Stixrude L. (Eds.), *Earth's Deep Interior: Mineral Physics and Tomography From Atomic to Global Scale; Geophysical Monograph 117*. American Geophysical Union, 237-264.
- Mancktelow N.S., 1994. On volume change and mass transport during the development of crenulation cleavage. *Journal of Structural Geology* 16, 1217-1231.
- Marlow P.C., Etheridge M.A., 1977. Development of a layered crenulation cleavage in mica schists of the Kanmantoo group near Macclesfield, South Australia. *Geological Society of America Bulletin* 97, 354-368.
- Mason, T.A., Adams, B.L., 1999. Use of microstructural statistics in predicting polycrystalline material properties, *Metallurgical and Materials Transactions A* 30A, 969-979.
- Masters G. & Stixrude L. (Eds.), *Earth's Deep Interior: Mineral Physics and Tomography From Atomic to Global Scale; Geophysical Monograph 117*. American Geophysical Union, 237-264.
- Matthies S., Humbert M., 1993. The realization of the concept of a geometric mean for calculating physical constants of polycrystalline materials. *Physica Status Solidi (b)* 177, K47-K50.
- Mauler A., Burlini L., Kunze K., Philippot P., Burg J.P., 2000. P-wave anisotropy in eclogites and relationship to the omphacite crystallographic fabric. *Physics and Chemistry of the Earth A* 25, 119-126.
- McNeil L.E., Grimsditch M., 1993. Elastic moduli of muscovite mica. *Journal of Physics: Condensed Matter* 5, 1681-1690.
- McWilliams C.K., Wintsch, R.P., Kunk, M.J., 2007. Scales of equilibrium and disequilibrium during cleavage formation in chlorite and biotite-grade phyllites, SE Vermont. *Journal of Metamorphic Geology* 25, 895-913.
- McSkimin H.J., Andreatch Jr P., Thurston R.N., 1965. Elastic moduli of quartz versus hydrostatic pressure at 25 degrees C and 195.8 degrees C. *Journal of Applied Physics* 36, 1624-1632.
- Means W.D., Rogers J., 1964. Orientation of purphyllite synthesized in slowly strained materials. *Nature* 204, 244-246.
- Means W.D., Williams P.F., 1972. Crenulation cleavage and faulting in an artificial salt-mica schist. *Journal of Geology* 80, 569-591.
- Meltzer A., Christensen N., 2001. Nanga Parbat crustal anisotropy: Implications for interpretation of crustal velocity structure and shear-wave splitting. *Geophysical Research Letters* 28, 2129-2132.
- Meyer E.E., Greene G.W., Alcantar N.A., Israelachvili J.N., Boles J.R., 2006. Experimental investigation of the dissolution of quartz by a muscovite mica surface: Implications for pressure solution. *Journal of Geophysical Research* 111, B08202.

- Moench R.H., Hildreth C.T., 1976. Geologic map of the Rumford Quadrangle, Oxford and Franklin Counties, Maine. United State Geological Survey: Map GQ-1272. Scale 1:62,500.
- Montagner J.P., Guillot L., 2002. Seismic anisotropy and global geodynamics. In: Ribbe P.H. & Rosso J.J. (Eds.), *Plastic Deformation of Minerals and Rocks; Reviews in Mineralogy and Geochemistry*, volume 51. Mineralogical Society of America, 353-385.
- Mooney W.D., 2007. Crust and lithospheric structure - global crustal structure. In: Schubert G., Romanowicz B. & Dziewonski A. (Eds.), *Treatise on Geophysics, Volume 1, Seismology and structure of the Earth*. Elsevier, 361-417.
- Naus-Thijssen F.M.J., Johnson S.E., Koons P.O., 2010. Numerical modeling of crenulation cleavage development: A polymineralic approach. *Journal of Structural Geology* 32, 330-341.
- Naus-Thijssen F.M.J., Goupee A.J., Vel S.S., Johnson S.E., in press. The influence of microstructure on seismic wave speed anisotropy in the crust: Computational analysis of quartz-muscovite rocks. *Geophysical Journal International*.
- Nicolas A., Christensen N.I., 1987. Formation of anisotropy in upper mantle peridotite: a review. In: Fuchs K. & Froidevaux C. (Eds.), *Composition, Structure and Dynamics of the Lithosphere-Asthenosphere System*. American Geophysical Union, Washington DC, 111-123.
- Niemeijer A.R., Spiers C.J., 2002. Compaction creep of quartz-muscovite mixtures at 500°C: preliminary results on the influence of muscovite on pressure solution. In: de Meer S., Drury M.R., de Bresser J.H.P. & Pennock G.M. (Eds.), *Deformation Mechanisms, Rheology and Tectonics: Current Status and Future Perspectives*. Geological Society, London, Special Publications, 200, 61-71.
- Nye J.F., 1957. *Physical Properties of Crystals: Their Representation by Tensors and Matrices*. Oxford University Press, London.
- Oelkers E.H., Bjørkum P.A., Murphy W.M., 1996. A petrographic and computational investigation of quartz cementation and porosity reduction in North Sea sandstones. *American Journal of Science* 296, 420-452.
- Okaya, D.A., Christensen, N., Stanley, D., Stern, T., 1995. Crustal anisotropy in the vicinity of the Alpine Fault Zone, South Island. *New Zealand Journal of Geology and Geophysics* 38, 579-583.
- Okaya, D.A., Christensen, N.I., 2002. Anisotropic effects of non-axial seismic wave propagation in foliated crustal rocks, *Geophysical Research Letters* 29, 1507. doi:10.1029/2001GL014285.
- Okaya, D.A., McEvelly, T.V., 2003. Elastic wave propagation in anisotropic crustal material possessing arbitrary internal tilt, *Geophysical Journal International* 153, 344-358.

- Ozacar, A.A., Zandt, G., 2004. Crustal seismic anisotropy in central Tibet: implications for deformation style and flow in the crust, *Geophysical Research Letters* 31, L23601. doi:10.1029/2004GL021096.
- Pagel M., Barbin V., Blanc P., Ohnenstetter D., 2000. Cathodoluminescence in Geosciences: An Introduction. In: Pagel M., Barbin V., Blanc P. & Ohnenstetter D. (Eds.), *Cathodoluminescence in Geosciences*. Springer Verlag, Berlin, 1-21.
- Passchier C.W., Trouw R.A.J., 2005. *Microtectonics*. Springer-Verlag.
- Peselnick L., Nicolas A., Stevenson P.R., 1974. Velocity anisotropy in a mantle peridotite from the Ivrea zone: Application to upper mantle anisotropy. *Journal of Geophysical Research* 79, 1175-1182.
- Price N.J., Cosgrove J.W., 1990. *Analysis of Geological Structures*. Cambridge University Press.
- Prior D.J., Mariani E., Wheeler J., 2009. EBSD in the Earth Sciences: Applications, Common Practice, and Challenges. In: Schwartz A.J., Kumar M., Adams B.L. & Field D.P. (Eds.), *Electron Backscatter Diffraction in Materials Science*, second edition. Springer, 345-360.
- Pulford A., Savage M., Stern T., 2003. Absent anisotropy: The paradox of the Southern Alps Orogen. *Geophysical Research Letters* 30, doi:10.1029/2003GL017758.
- Ramberg H., 1960. Relationships between lengths of arc and thickness of pygmatically folded veins. *American Journal of Science* 258, 36-46.
- Ramberg H., 1961. Contact strain and fold instability of a multilayered body under compression. *Geologische Rundschau* 51, 405-439.
- Ramberg H., 1963. Fluid dynamics of viscous buckling applicable to folding of layered rocks. *Bulletin of the American Association of Petroleum Geologists* 47, 484-505.
- Readman, P.W., Hauser, F., O'Reilly, B.M., Do, V.C., 2009. Crustal anisotropy in southwest Ireland from analysis of controlled source shear-wave data, *Tectonophysics* 474, 571-583.
- Reid A.C.E., Langer S.A., Lua R.C., Coffman V.R., Haan S., Garcia E.R., 2008. Image-based finite element mesh construction for material microstructures. *Computational Materials Science* 43, 989-999.
- Reuss A., 1929. Berechnung der Fließgrenze von Mischkristallen auf grund der Plastizitätsbedingung für Einkristalle. *Zeitschrift für angewandte Mathematik und Mechanik* 9, 9-58.
- Richter D.K., Götte T., Götze J., Neuser R.D., 2003. Progress in application of cathodoluminescence (CL) in sedimentary petrology. *Mineralogy and Petrology* 79, 127-166.
- Robin P.Y.F., 1979. Theory of metamorphic segregation and related processes. *Geochimica et Cosmochimica Acta* 43, 1587-1600.

- Ronde A.A. de, Stünitz H., 2007. Deformation-enhanced reaction in experimentally deformed plagioclase-olivine aggregates. *Contributions to Mineralogy and Petrology* 153, 699-717.
- Rusk B.G., Reed M., Dilles J.H., Kent A.J.R., 2006. Intensity of quartz cathodoluminescence and trace-element content in quartz from the porphyry copper deposit at Butte, Montana. *American Mineralogist* 91, 1300-1312.
- Rutter E.H., 1983. Pressure solution in nature, theory and experiment. *Journal of the Geological Society of London* 140, 725-740.
- Rutter E.H., Wanten P.H., 2000. Experimental study of the compaction of phyllosilicate-bearing sand at elevated temperature and with controlled pore water pressure. *Journal of Sedimentary Research* 70, 107-116.
- Saha D., 1998. Local volume change vs overall volume constancy during crenulation cleavage development in low grade rocks. *Journal of Structural Geology* 20, 587-599.
- Sanchez-Palencia, E., 1981. Nonhomogeneous media and vibration theory. *J. Acoust. Soc. Am.*, 69, 884.
- Sanchez-Palencia E., 1983. Homogenization method for the study of composite media. *Asymptotic Analysis II* 985, 192-214.
- Savage M.K., 1999. Seismic anisotropy and mantle deformation: What have we learned from shear wave splitting?. *Reviews of Geophysics* 37, 65-106.
- Savage M.K., Duclos M., Marson-Pidgeon K., 2007. Seismic anisotropy in South Island, New Zealand. In: Okaya D., Stern T. & Davey F. (Eds.), *A Continental Plate Boundary: Tectonics at South Island, New Zealand, Geophysical Monograph Series 175*. American Geophysical Union, 95-114.
- Scheltema K.E., 2003. Microstructural analysis of crenulation cleavage and garnet prophyroblast microfabrics in the Moretown formation, western Massachusetts: Implications for models of prophyroblast growth and crenulation cleavage formation. MSc. Thesis, University of Massachusetts, Amherst.
- Schoneveld C., 1979. The geometry and the significance of inclusion patterns in syntectonic prophyroblasts. Ph.D. thesis, Universiteit Leiden, the Netherlands.
- Schwarzer R.A., Field D.P., Adams B.L., Kumar M., Schwartz A.J., 2009. Present state of electron backscatter diffraction and prospective developments, 2nd edition . In: Schwartz A.J., Kumar M., Adams B.L. & Field D.P. (Eds.), *Electron Backscatter Diffraction in Materials Science*. Springer, New York, 1-20.
- Seront B., Mainprice D., Christensen N.I., 1993. A determination of the three-dimensional seismic properties of anorthosite: Comparison between values calculated from the petrofabric and direct laboratory measurements. *Journal of Geophysical Research* 98, 2209-2221.
- Shapiro, N.M., Ritzwoller, M.H., Molnar, P., Levin, V., 2004. Thinning and flow of Tibetan crust constrained by seismic anisotropy, *Science*, 305, 233.

- Sharpe D., 1849. On slaty cleavage. *The Quarterly Journal of the Geological Society of London* 5, 111-129.
- Sherrington, H.F., Zandt, G., Fredriksen, A., 2004. Crustal fabric in the Tibetan Plateau based on waveform inversions for seismic anisotropy parameters, *Journal of Geophysical Research* 109, B02312. doi:10.1029/2002JB002345.
- Silver P.G., 1996. Seismic anisotropy beneath the continents: Probing the depths of geology. *Annual Reviews of Earth and Planetary Sciences* 24, 385-432.
- Simmons, G., 1964. Velocity of shear waves in rocks to 10 kilobars, *Journal of Geophysical Research* 69, 1123-1130.
- Sippel R.F., 1968. Sandstone petrology, evidence from luminescence petrography. *Journal of Sedimentary Petrology* 38, 530-554.
- Sorby H.C., 1857. On some facts connected with slaty cleavage. *British Association for the Advancement of Science Report 1857*, 92-93.
- Sorby H.C., 1863. On the direct correlation of mechanical and chemical forces. *Proceedings of the Royal Society of London* 12, 538-550.
- Sorby H.C., 1880. On the structure and origin of non calcareous rocks. *Proceedings of the Geological Society of London* 36, 46-92.
- Sprunt E.S., Nur A., 1977. Destruction of porosity through pressure solution. *Geophysics* 42, 726-741.
- Stephansson O., 1974. Stress-induced diffusion during folding. *Tectonophysics* 22, 233-251.
- Silver P.G., 1996. Seismic anisotropy beneath the continents: Probing the depths of geology. *Annual Reviews of Earth and Planetary Sciences* 24, 385-432.
- Tatham D.J., Lloyd G.E., Butler R.W.H., Casey M., 2008. Amphibole and lower crustal seismic properties. *Earth and Planetary Science Letters* 267, 118-128.
- Terada K., Hori M., Kyoya T., Kikuchi N., 2000. Simulation of the multi-scale convergence in computational homogenization approaches. *International Journal of Solids and Structures* 37, 2285-2311.
- Tomachak P.B., Brown M., Solar G.S., Becker H.J., Centorbi T.L., Tian J., 2005. Source contributions to Devonian granite magmatism near the Laurentian border, New Hampshire and Western Maine, USA. *Lithos* 80, 75-99.
- Tommasi A., Mainprice D., Canova G., Chastel Y., 2000. Viscoplastic self-consistent and equilibrium-based modeling of olivine lattice preferred orientations: Implications for the upper mantle seismic anisotropy. *Journal of Geophysical Research* 105, 7893-7908.
- Tullis T.E., Horowitz F.G., Tullis J., 1991. Flow laws of polyphase aggregates from end-member flow laws. *Journal of Geophysical Research* 96, 8081-8096.

- Ullemeyer K., Braun G., Dahms M., Kruhl J.H., Olesen N.Ø., Siegesmund S., 2000. Texture analysis of a muscovite-bearing quartzite: a comparison of some currently used techniques. *Journal of Structural Geology* 22, 1541-1557.
- Valcke S.L.A., Casey M., Lloyd G.E., Kendall J.M., Fisher Q.J., 2006. Lattice preferred orientation and seismic anisotropy in sedimentary rocks. *Geophysical Journal International* 166, 652-666.
- van der Pluijm B.A., Ho N., Peacor D.R., 1994. High-resolution X-ray texture goniometry. *Journal of Structural Geology* 16, 1029-1032.
- Vaughan M.T., Guggenheim S., 1986. Elasticity of muscovite and its relationship to crystal structure. *Journal of Geophysical Research* 91, 4657-4664.
- Vel S.S., Goupee A.J., 2010. Multiscale thermoelastic analysis of random heterogeneous materials, Part I: Microstructure characterization and homogenization of material properties. *Computational Materials Science* 48, 22-38.
- Venables J.A., Harland C.J., 1973. Electron backscatter patterns - a new technique for obtaining crystallographic information in the scanning electron microscope. *Philosophical Magazine* 27, 1193-1200.
- Vergne, J., Wittlinger, G., Farra, V., Su, H., 2003. Evidence for upper crustal anisotropy in the Songpan-Ganze (northeastern Tibet) terrane, *Geophysical Research Letters* 30, 1552. doi:10.1029/2002GL016847.
- Vernon R.H., 1998. Chemical and volume changes during deformation and prograde metamorphism of sediments. In: Treloar P.J. & O'Brien P.J. (Eds.), *What drives metamorphism and metamorphic reactions?*. Geological Society, London, Special Publications, 138, 215-246.
- Vernon R.H., 2004. *A Practical Guide to Rock Microstructure*. Cambridge University Press, Cambridge, UK.
- Vernon R.H., Clarke G.L., 2008. *Principles of Metamorphic Petrology*. Cambridge University Press.
- Voigt W., 1928. *Lehrbuch der Kristallphysik*. B.G. Teubners Lehrbücher, Leipzig.
- Wark D.A., Watson E.B., 2006. The TitaniQ: a titanium-in-quartz geothermometer. *Contributions to Mineralogy and Petrology* 152, 743-754.
- Weiss, T., Siegesmund, S., Rabbel, W., Bohlen, T., Pohl, M., 1999. Seismic velocities and anisotropy of the lower continental crust: A review, *Pure Applied Geophysics* 156, 97-122.
- Wendt A.S., Bayuk I.O., Covey-Crump S.J., Wirth R., Lloyd G.E., 2003. An experimental and numerical study of the microstructural parameters contributing to the seismic anisotropy of rocks. *Journal of Geophysical Research* 108, 2365, doi:10.1029/2002JB001915.

- Weyl P.K., 1959. Pressure solution and the force of crystallization - A phenomenological theory. *Journal of Geophysical Research* 64, 2001-2025.
- Wilkinson A.J., 1991. Quantitative deformation studies using electron back scatter patterns. *Acta Metallurgica et Materialia* 39, 3047-3055.
- Williams M.L., Scheltema K.E., Jercinovic M.J., 2001. High-resolution compositional mapping of matrix phases: implications for mass transfer during crenulation cleavage development in the Moretown Formation, western Massachusetts. *Journal of Structural Geology* 23, 923-939.
- Williams P.F., 1972. Development of metamorphic layering and cleavage in low grade metamorphic rocks at Bermagui, Australia. *American Journal of Science* 272, 1-47.
- Willis J.R., 1977. Bounds and self-consistent estimates for the overall properties of anisotropic composites. *Journal of the Mechanics and Physics of Solids* 25, 185-202.
- Wilshire H.G., Trask N.J., 1971. Structural and textural relationships of amphibole and phlogopite in peridotite inclusions, Dish Hill, California. *The American Mineralogist* 56, 240-255.
- Wintsch R.P., Dunning J., 1985. The effect of dislocation density on the aqueous solubility of quartz and some geologic implications: a theoretical approach. *Journal of Geophysical Research* 90, 3649-3657.
- Worley B., Powell R., Wilson C.J.L., 1997. Crenulation cleavage formation: evolving diffusion, deformation and equilibration mechanisms with increasing metamorphic grade. *Journal of Structural Geology* 19, 1121-1135.
- Wright T.O., Henderson J.R., 1992. Volume loss during crenulation cleavage formation in the Meguma Group, Nova Scotia, Canada. *Journal of Structural Geology* 14, 281-290.
- Xu, Y., Li, Z., Roecker, S.W., 2007. Uppermost mantle structure and its relation with seismic activity in the central Tien Shan, *Geophysical Research Letters* 34, L10304. doi:10.1029/2007GL029708.
- Žák J., Verner K., Týcová P., 2008. Grain-Scale processes in actively deforming magma mushes: New insights from electron backscatter diffraction (EBSD) analysis of biotite schlieren in the Jizera granite, Bohemian Massif. *Lithos* 106, 309-322.
- Zhang Y., Mancktelow N.S., Hobbs B.E., Ord A., Mühlhaus H.B., 2000. Numerical modelling of single-layer folding: clarification of an issue regarding the possible effect of computer codes and the influence of initial irregularities. *Journal of Structural Geology* 22, 1511-1522.
- Zinkernagel U., 1978. Cathodoluminescence of quartz and its application to sandstone petrology. In: Fuchtbauer H. & Milliman J.D. (Eds.), *Contributions to Sedimentology*. E. Schweizerbart'sche Verlagsbuchhandlung, Stuttgart, 1-69.

Appendix A

A SENSITIVITY STUDY REGARDING RESULTS OBTAINED WITH AEH-FE

A.1. Introduction

The asymptotic expansion homogenization method combined with the finite element method (AEH-FE) is used to calculate effective elastic properties of rocks based on orientation maps obtained using electron backscatter diffraction (EBSD). EBSD is a scanning electron microscope technique that can be used for both phase identification and the analysis of crystallographic orientations in a sample. Electrons bombarding the sample diffract from the crystal lattice, generating a number of bands on a phosphor screen that each represent a set of lattice planes, with a width that correlates to the lattice spacing (Goldstein et al., 2003). The bands together form an electron backscatter diffraction pattern (EBSP) that is characteristic of the phase and orientation of the crystal. EBSPs can be collected automatically over a predefined grid allowing the linkage of EBSD data to spatial position within a sample and thus creating a mineral orientation map. The map size is determined by the size of the area of interest and the step size that is chosen between the sampled points. The size of the area of interest is determined by sample heterogeneity (the area analyzed needs to be representative for the sample), or the size of the feature or microstructure of interest. The step size depends on the grain size of the minerals in the sample (a minimum number of data points are necessary per grain) and the amount of detail required.

Because of computational limitations it is not always possible to calculate a bulk AEH-FE result from one large map with a sufficiently fine mesh. In these instances the map is divided into smaller regions which are analyzed separately. The average of the results of those smaller regions provides the bulk elastic moduli of the studied map. In this Appendix we test the heterogeneity/homogeneity of three samples by comparing the results from different sized maps, and by investigating the efficiency of random sampling versus tiling. We also present a sensitivity study that compares elasticity results derived from one large map versus the averaged results of a number of smaller maps with varying mesh densities.

A.2. Samples

For the sensitivity analyses reported here, we use a peridotite sample with compositional layering and two phyllosilicate-rich samples with textures typically found in deformed crustal rocks. The peridotite sample (sample DH13) comes from Dish Hill in Southern California. Dish Hill is a cone of basanite located about 70 miles east of Barstow. Fission-track age dating of

apatite from a granitic inclusion sets the age of the cone to 2.1±0.2 m.y. (Wilshire and Trask, 1971). Peridotite inclusions in the basanite consist of olivine, enstatite, diopside and spinel. The sample was polished with progressively finer grades of diamond suspension (down to 0.3 µm), followed by a chemo-mechanical polish with colloidal silica for approximately 8 hours. EBSD mineral orientation data were derived using the EDAX-TSL EBSD detector on the Tescan Vega II Scanning Electron Microscope at the Department of Earth Sciences, University of Maine. Chemical analyses were performed simultaneously using EDAX Genesis energy dispersive spectroscopy (EDS). The diffraction patterns were background corrected and processed using EDAX-TSL OIM Data Collection 5 software. The patterns were recorded at a working distance of 25mm, using 20 kV acceleration voltage, with the uncoated sample tilted 20° to the incident beam. The map was collected with a square grid and a step size of 20 µm. Post processing procedures included removing single point measurements and dilating the map to fill up all non-indexed points. Figure A1 shows a photomicrograph, a compositional map, the EBSD mineral orientation map, and pole figures with crystal orientations of this sample.

The phyllosilicate-rich sample with the planar foliation comes from the Mooselookmeguntic igneous complex aureole in western Maine (sample D3053). The main part of the Mooselookmeguntic complex was emplaced approximately 370 Ma into steeply dipping metaturbidites that were folded during the Devonian, subduction-related, Acadian orogeny (Tomachak et al., 2005). A zone of contact metamorphism, extending 5-10 km from the contact, and a zone of deformation, extending ~3 km from the contact, formed due to the emplacement of the complex. A strain gradient was preserved in the aureole with a deformation fabric that evolves through all stages of crenulation cleavage formation (e.g., Johnson et al., 2006, 2010). The sample was collected approximately 400 meters from the contact with the intrusive complex and preserved the final stage of crenulation cleavage development: a pervasive planar foliation, parallel to the intrusive contact, defined by muscovite and biotite grains in a quartz and plagioclase matrix. The sample was polished with progressively finer grades of diamond suspension, down to 3 µm, followed by a polish with 1 and 0.3 µm alumina suspension on a nap pad, and a polish with colloidal silica for 3 minutes. The acquisition and post processing of the orientation data was done the same as described above, except that this map was collected with a hexagonal grid and a step size of 4 µm. Figure S2 shows a photomicrograph, a compositional map, the EBSD mineral orientation map, and pole figures with crystal orientations of this sample.

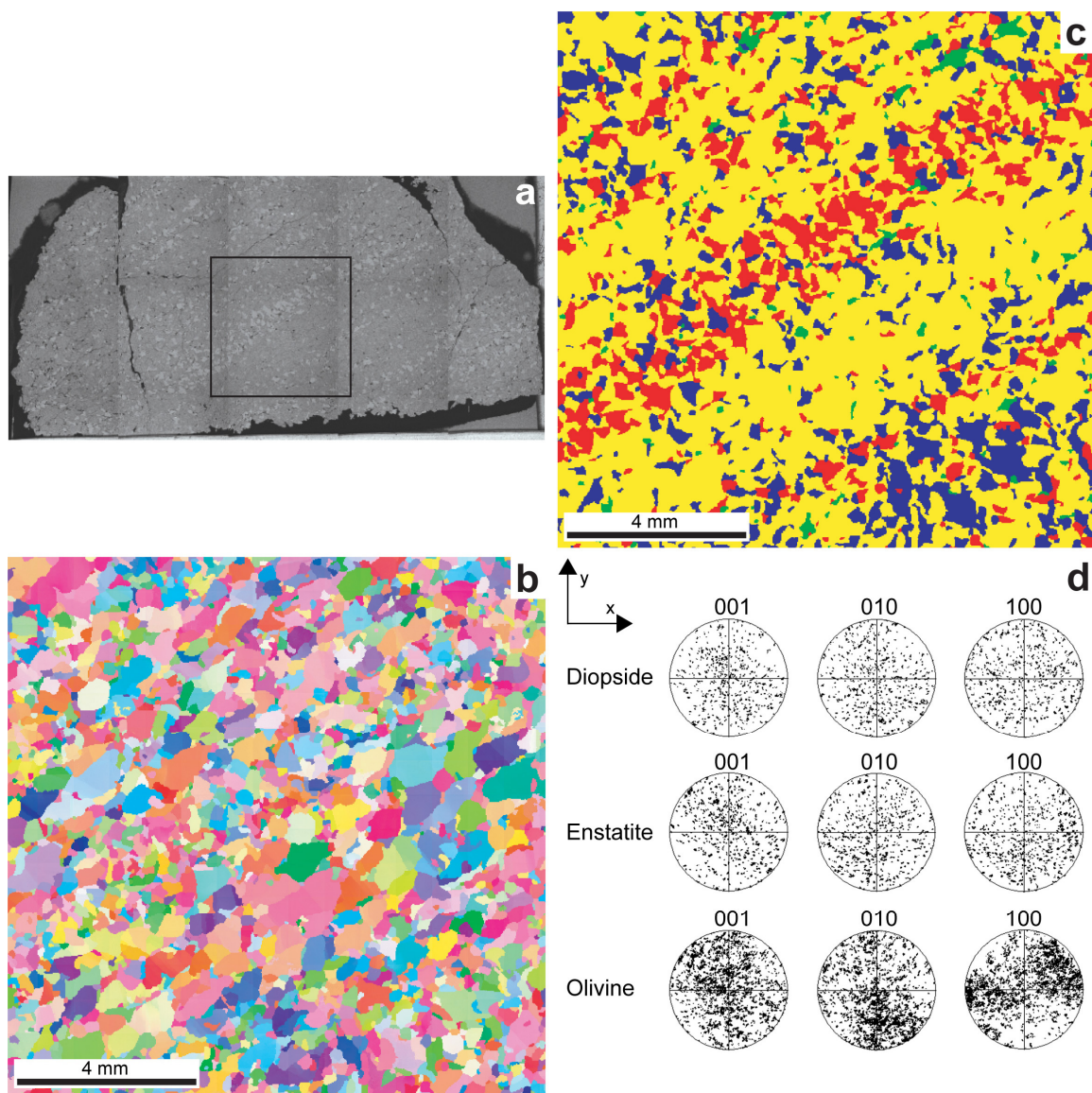


Figure A1. Sample DH13. (a) The backscattered electron map. (b) The EBSD mineral orientation map of the area indicated in (a). (c) The corresponding phase map in which yellow is olivine, red is diopside, blue is enstatite, and green is spinel. (d) The pole figures of the main minerals plotted in the lower hemisphere.

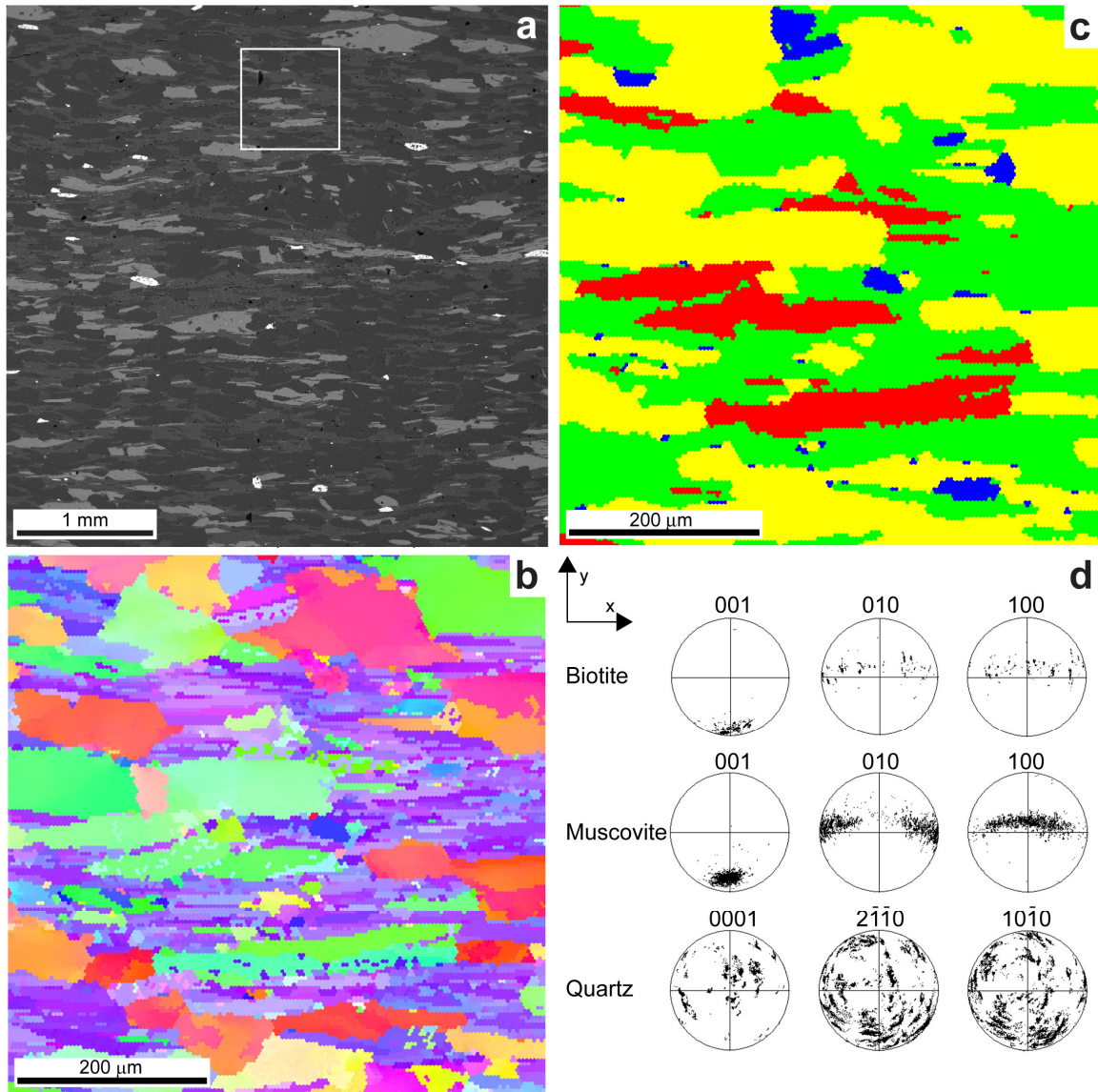


Figure A2. Sample D3053. (a) The backscattered electron map. (b) The EBSD mineral orientation map of the area indicated in (a). (c) The corresponding phase map in which yellow is quartz, red is biotite, blue is feldspar, and green is muscovite. (d) The pole figures of the main minerals plotted in the lower hemisphere.

Sample MT23P1 comes from the Moretown Formation in western Massachusetts. The sample has a well developed crenulation cleavage, defined by muscovite and biotite in a quartz and plagioclase matrix. The Moretown formation consists of upright to steeply-dipping folds in which an axial planar crenulation cleavage has developed in the fold hinges. This sample, its texture, and its geological settings are described in more detail in the accompanying paper. The paper contains a description of how the sample was prepared and how the EBSD map from this sample was derived (similar as described above).

A.3. Window Size and Mesh Density

For the sensitivity analyses presented in this supplement, the two parameters varied are the window size and mesh density. The window size is the part of the EBSD map over which the elastic bulk properties are calculated. The window size is varied to test the representativeness of the samples and to subdivide a map that is too large and detailed to mesh and analyze. For our purposes, the window size is taken as a square area, and the length of each side of this square is expressed as the fraction (F) of the shortest dimension of the full map. The full map can either be square or rectangular, but the most convenient value of F is obtained by ensuring that the long dimension of the map is an integer multiple of the short dimension.

The accuracy of a FE calculation depends on the quality of the FE mesh. Elements must be small enough to give accurate results while minimizing computational effort (Logan, 2007). The FE yields an upper bound on the true stiffness, so the solutions for the stiffness will decrease with an increasing number of elements (Desai and Abel, 1972; Logan, 2007). For our mesh we use six-noded triangular elements because they yield the best results for a given number of degrees of freedom (e.g. Cook et al., 2002). The mesh density indicates the number of elements per area investigated. Figure A3 gives an example of meshes used to make calculations for the crenulation cleavage sample. Table A1 gives an overview of the corresponding average number of elements for specific window sizes of that sample.

A.4. Heterogeneity/Homogeneity of Samples

A.4.1. Sensitivity of Sample Size

Accurate computational analysis of tensor variables such as stress, strain and elastic stiffness from heterogeneous samples require that a representative area or volume element is analyzed. For the analyses presented in this Appendix and the paper we are limited to sample sizes based on the size of a thin section, limitations regarding the size of the EBSD map (a

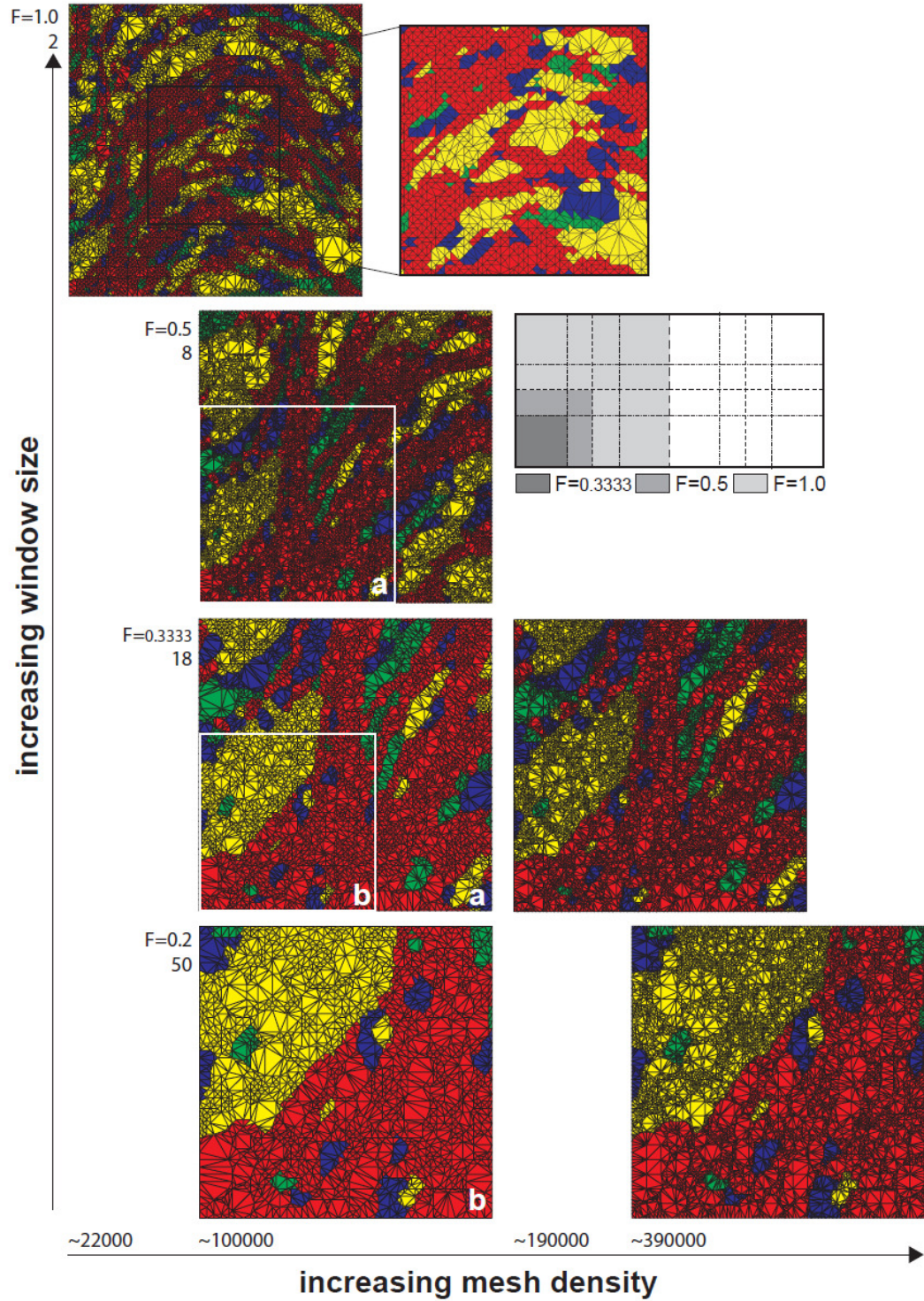


Figure A3. Examples of meshes for different window sizes and mesh densities for sample MT23P1. The numbers along the increasing window size axis indicate the fraction (F) and the total number of windows necessary to calculate the elastic properties of the entire sample. The numbers along the increasing mesh density axis indicates the approximate number of elements the entire sample consists of.

Table A1. Overview of the number of elements for the different window sizes and mesh densities for sample MT23P1. The highlighted setups have a comparable mesh density.

| F | windows | density | # of elements | | |
|--------|---------|---------|---------------|-------|-------|
| | | | average | min | max |
| 1 | 2 | 60 | 11050 | 11264 | 10836 |
| 0.5 | 8 | 80 | 12976 | 11702 | 14086 |
| 0.3333 | 18 | 52 | 5580 | 4618 | 6414 |
| 0.3333 | 18 | 80 | 10357 | 8930 | 11634 |
| 0.25 | 32 | 40 | 3265 | 2612 | 4106 |
| 0.25 | 32 | 80 | 8810 | 7210 | 10706 |
| 0.2 | 50 | 32 | 2100 | 1464 | 2634 |
| 0.2 | 50 | 80 | 7808 | 5338 | 9844 |

combination of step size and time available on the SEM) and computational limitations (based on number of data points). In continuum mechanics the concept of a representative volume element (RVE) plays a crucial role in determining the appropriate scale of analysis (Jiang and Jasiuk, 2001). Drugan and Willis (1996) define a RVE as “the smallest material volume element of the composite for which the usual spatially constant overall modulus’ macroscopic constitutive representation is a sufficiently accurate model to represent mean constitutive response”. Using this definition, we conducted sensitivity analyses to determine if the chosen maps are representative for the rock. We calculated the bulk stiffness of a series of windows with increasing size of the same sample. If the sample is statistically homogeneous, the solution will converge once a critical window size is reached. This critical window size will be a representative area for the sample and should give similar results regardless of the location of the window in the sample.

We calculated the bulk elastic properties of a range of window sizes with comparable mesh densities for each sample (Figure A3). For the peridotite sample (DH13large) the solutions quickly converge and a window size of 0.5 gives a representative result for this thin section. The stiffness moduli calculated for the map derived from the planar foliation sample (D3053) converge at a window size of 0.5, indicating that the map is representative for the thin section. In contrast, the stiffnesses do not fully converge for the crenulation cleavage sample (MT23P1) owing to the geometric and mineralogical heterogeneity within the sample. The curves for the stiffness moduli possibly flatten out at a window size of 0.9 or 1.0, but a larger sample would be required to test this. Because of the strong control on the anisotropy exerted by the crenulations, the microfold wavelength can be interpreted as a characteristic length scale. Our purpose here is

to examine the effect of a crenulation cleavage on the seismic anisotropy, so the map is chosen in a way that represents one characteristic length, which also allows the sample to be treated as periodic.

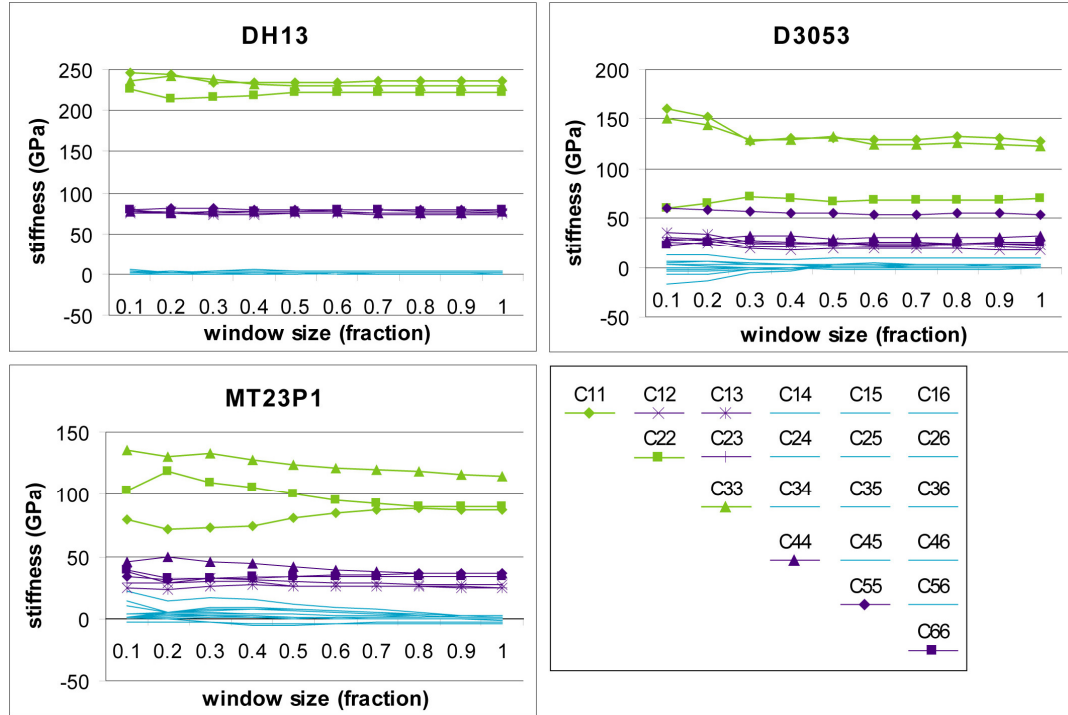


Figure A4. The AEH stiffnesses for increasing window sizes for the three different samples.

A.4.2. Sensitivity of Sampling Random Windows

A study by Gusev (1997) on a periodic composite consisting of two elastically isotropic phases showed that the overall elastic constants of a composite can be accurately predicted by sampling just a few randomly positioned windows. In order to test if this approach applies to our polyminerale rock samples we computed the C11 and C22 moduli for a number of randomly positioned windows within the peridotite and planar foliation samples (see Figure A4). The size of the windows ($F=0.3333$ in both cases) is smaller than the representative window size calculated in the previous section. The individual results per randomly positioned window and the cumulative average of these results are plotted and compared against the C11 and C22 moduli calculated for the entire sample. The average result of 9 tiled windows of the same size ($F=0.3333$) is included as comparison as well. The mesh density in all these examples is kept constant.

For both sample DH13 and sample D3053 the cumulative average of the randomly positioned windows does eventually converge to the value calculated from the entire map. For sample DH13 all the cumulative averages are within 1.5% of the result for the entire sample, indicating that the sample is statistically homogeneous to a fair degree and averaging the properties of just a few random measurements will give an accurate result. For sample D3053 27 random measurements needed to be averaged to arrive at a value that falls within 1.5% of the entire sample value. It is clear from this analysis that dividing the sample into 9 tiled windows is more efficient than randomly positioning the analysis window, especially if the sample is heterogeneous. The randomly positioned windows reanalyze various regions of the sample, and more iterations are required to average out the heterogeneity.

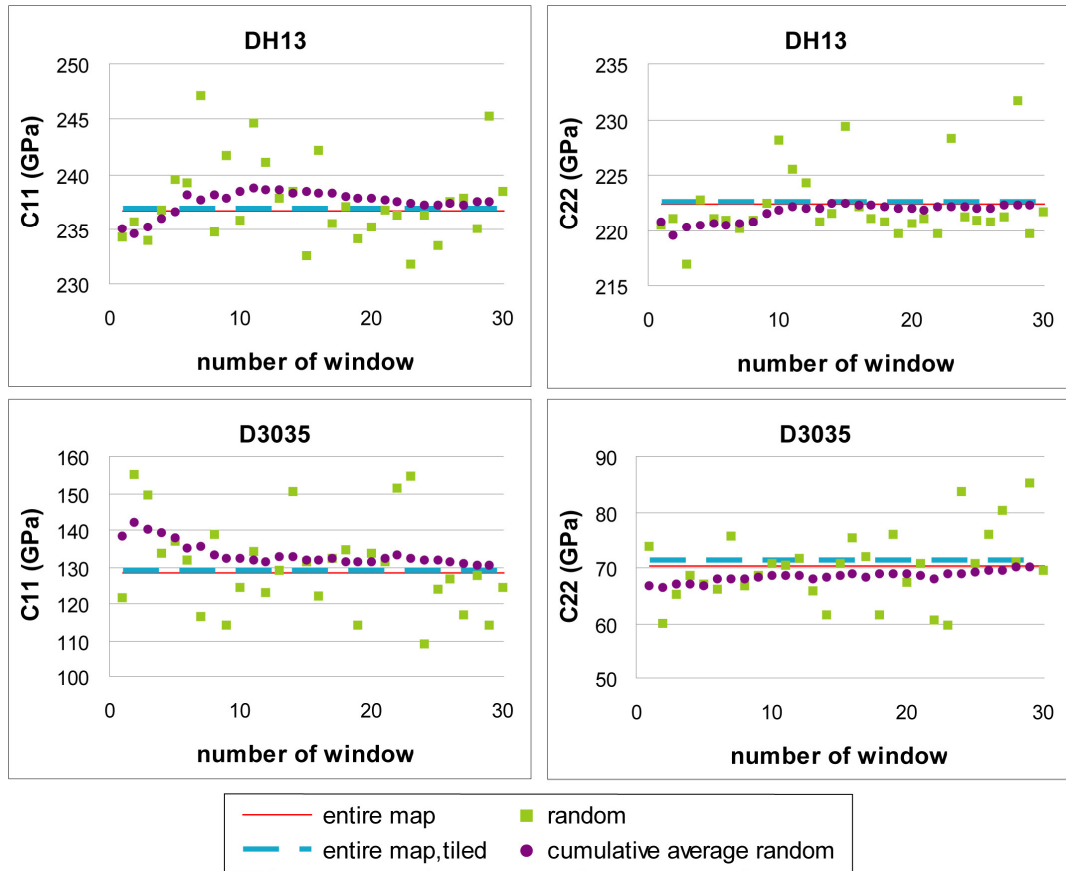


Figure A5. Comparison of the C11 and C22 stiffness moduli for samples DH13 and D3053 calculated from (1) the entire map, (2) the average of 9 tiled samples covering the entire map, (3) 30 random samples from the entire map, and (4) the cumulative average of the random samples.

A.5. Dividing a Map into Smaller Maps

Owing to the relatively fine mesh densities required to conduct FE analysis on rock microstructures, it is computationally favorable to divide a large map into smaller regions. In this section we show sensitivity analyses of both this subdivision and the mesh density. Sample D3053 is divided into 1, 2x2, 3x3 and 4x4 windows with comparable mesh densities and the finest mesh possible for the specific window sizes. Sample MT23P1 is rectangular and is divided into 1x2, 2x4, 3x6, 4x8 and 5x10 windows. For MT23P1 the mesh densities are comparable for all except the 1x2 maps, which have a lower mesh density for computational reasons. Data calculated using the finest mesh possible for each specific window size are also presented. All results are shown in Figure A6. As a comparison the figure also includes the Voigt, Reuss, VRH and geometric mean results calculated using Mainprice's ANIS_Ang_PC program (Mainprice, 1990; available at ftp://www.gm.univ-montp2.fr/mainprice//CareWare_Unicef_Programs/).

A.5.1. Sensitivity to the Number of Maps

The plots on the left hand side of Figure A6 shows that the Voigt and Reuss averages all are very similar regardless of which calculation method is used. Small differences can be expected because the Voigt and Reuss stiffnesses calculated by the AEH-FE program are based on the mesh instead of the actual input (as is the case with ANIS_Ang_PC).

The AEH-FE results increase slightly with increasing number of windows, which is caused by the increasing number of boundaries (the boundary effects begin to play a larger role). This is in accordance with findings of Kanit et al. (2003). Ideally we would calculate our results with a fine mesh and a small number of windows. Because the calculated AEH-FE results all lie within 3% of each other (within 1.5% for sample D3053), we find it acceptable to use a reasonable fine mesh and an intermediate number of windows.

A.5.2. Sensitivity to the Mesh Density

Figure A6 shows that the mesh refinement does not significantly affect the results. In most cases the results are slightly lower with increased mesh density, which reflects the fact that the finite method yields an upper bound on the true stiffness (Desai and Abel, 1972; Logan, 2007). From our experience the mesh density has a larger influence on stress and strain calculations than on bulk stiffness calculations. For the calculation of bulk elasticity a relatively coarse mesh can be applied.

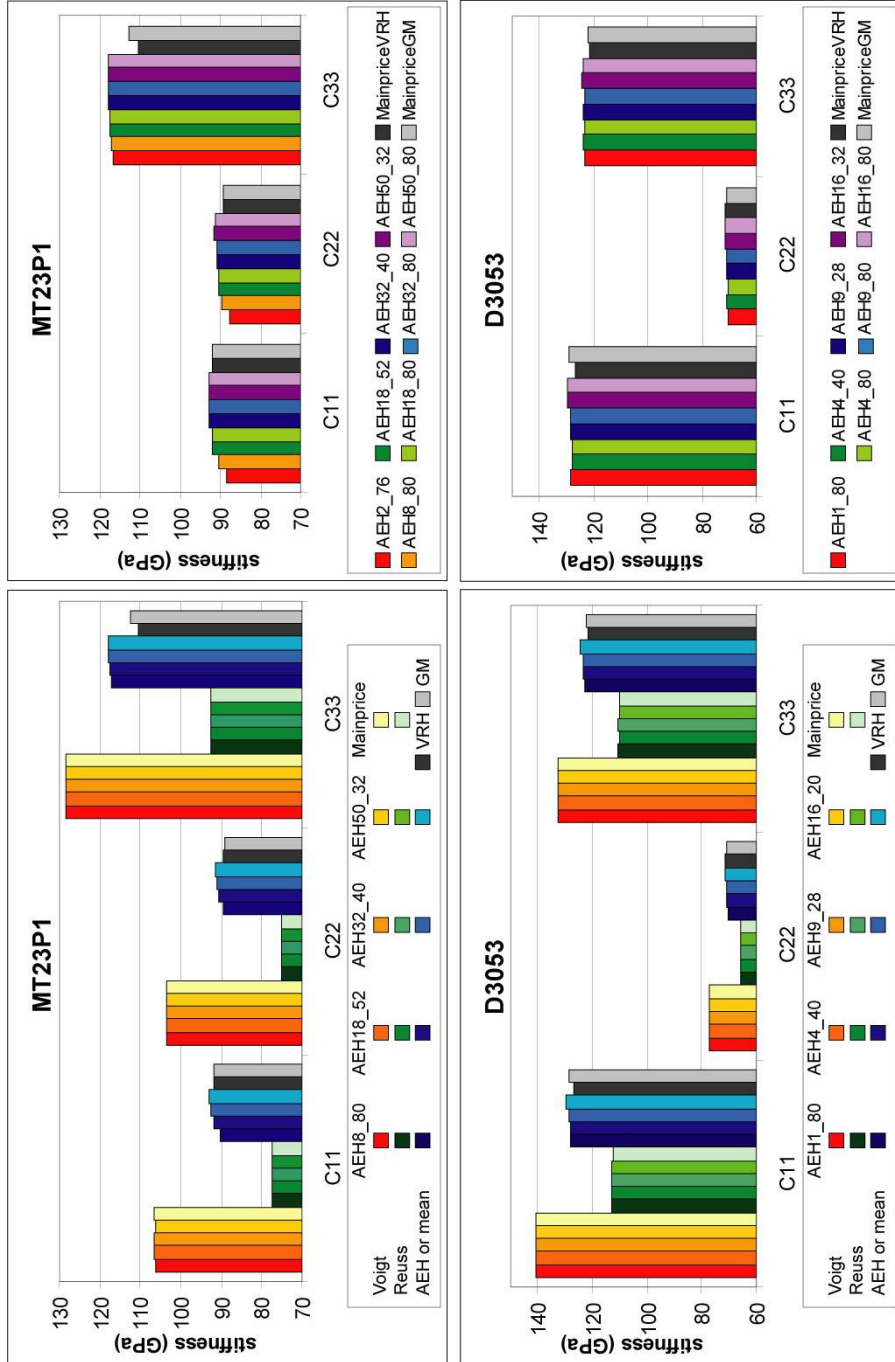


Figure A6. C11, C22 and C33 stiffness components calculated from the average of multiple window sizes with comparable mesh densities (left plots) and with different mesh densities (right plots). The plots on the left also contain the Voigt and Reuss averages obtained both with the AEH program and the ANIS_Ang_PC program from Mainprice (1990). The names in the legend are built up as follows: (1) method used to calculate the modulus (“AEH” or “Mainprice”), (2) the number of total windows the map was divided in, and (3) a number indicating the mesh density (a higher number indicates a finer mesh). VRH indicates Voigt Reuss Hill average and GM indicates the geometric mean.

A.6. Concluding Remarks

1) To investigate if the presented EBSD orientation maps are representative areas of the thin sections, we performed a study in which we increased the sample size. Even though this method does not turn out to be applicable to all rocktypes, the results show that the samples from this sensitivity analysis study are representative sample areas.

2) Although sampling a few randomly positioned windows is an efficient way to calculate the bulk elastic properties of samples that are homogeneous and effectively isotropic, it is not a useful method for polymineralic materials that are composed of anisotropic minerals. By dividing an entire map into tiled windows that have the same size and mesh density as the randomly positioned sample windows, an accurate result is achieved more rapidly than when sampling the map randomly.

3) Sensitivity analyses show that dividing the map into multiple smaller maps has a larger effect on the bulk elastic stiffnesses of the entire map than changing the mesh density. Increasing the number of windows increases the influence of boundary effects. Even with a coarse mesh (and fewer windows) the calculated results are representative for the area studied. The data we present in the paper are calculated using a reasonably fine mesh that defines the phases and most of the grains well, and that has the least number of windows that are computationally convenient given the chosen mesh density.

Appendix B

MASS TRANSFER OF QUARTZ DURING CRENULATION CLEAVAGE FORMATION: A CATHODOLUMINESCENCE STUDY

B.1. Introduction

Crenulation cleavage is the most common type of cleavage in multiply-deformed pelitic rocks. The fabric is characterized by phyllosilicate-rich domains (P-domains) in which the phyllosilicates define the overall cleavage separated by quartz- and feldspar-rich domains (QF-domains). This characteristic differentiation of minerals is thought to result from dissolution of quartz and feldspar in the P-domains and either the precipitation of the dissolved material in the QF-domains or the removal of the dissolved material from the local system. Quartz grains in this fabric typically show no evidence for intracrystalline deformation or recrystallization.

Williams et al. (2001) presented high-resolution compositional maps from samples of the Moretown Formation in western Massachusetts that contain a crenulation cleavage. In these rocks, multiple stages of crenulation cleavage development are present: an almost planar S_2 foliation in the F_3 fold limbs and a well-developed S_3 crenulation cleavage is present in the F_3 fold hinge regions. Williams et al. (2001) showed that overgrowths formed on plagioclase and muscovite grains that have geometries that indicate that they formed during crenulation cleavage formation. They found An_{14-16} rims overgrew An_{03} cores in both the P- and QF-domains and phengitic muscovite overgrew muscovite in the P-domains. In the fold limbs, where the crenulation cleavage is well-developed, the plagioclase grains are smaller in the crenulation limbs than in the crenulation hinges. In the crenulation hinges the plagioclase cores have aspect ratios of about 3:1 that are aligned with the S_2 cleavage. The overgrowths are more equant in shape in the crenulation hinges. In the crenulation limbs the cores have smaller aspect ratios compared to those in the crenulation hinges. The overgrowths have large aspect ratios and are aligned with the

new S_3 crenulation cleavage. In the fold hinges, where the crenulation cleavage is not or very poorly developed, the second generation plagioclase primarily occurs as needles, fibers, and strain shadows aligned with the S_2 cleavage.

Both quartz and feldspar relocate during crenulation cleavage formation. Because of this, microstructures similar to those found in plagioclase by Williams et al. (2001) should also be present in quartz. Quartz does not have as great of a range in chemistry as plagioclase, so compositional mapping is not a useful method to explore these geometries in quartz. Instead, Cathodoluminescence (CL) is a better method to investigate the mass transfer of quartz during crenulation cleavage development because it is able to unveil the presence of trace elements or dislocations in minerals such as quartz. I used CL imaging to investigate quartz overgrowths and other microstructures related to crenulation cleavage development from samples from the Mooselookmeguntic Pluton aureole in western Maine and the Moretown Formation in western Massachusetts.

B.2. Sample Locality

I studied the CL behavior of quartz in 6 samples from the Mooselookmeguntic Pluton aureole, western Maine, representing 4 different stages of crenulation cleavage development. The main part of the Mooselookmeguntic Pluton was emplaced approximately 370 Ma into steeply dipping metaturbidites that were folded during the subduction-related, Acadian orogeny (Tomascak et al., 2005). A zone of contact metamorphism, extending 5-10 km from the contact, and a zone of deformation, extending ~3 km from the contact, formed due to the emplacement of the pluton. A strain gradient was preserved in the aureole with a deformation fabric that evolves through 5 stages of crenulation cleavage formation (e.g. Johnson et al., 2006, 2010). Figure B1 shows a schematic drawing of the 5 stages of crenulation cleavage development in the area as they are defined by Johnson et al. (2006). Sample D3034 was collected at the greatest distance from the pluton and has a pervasive planar foliation representing stage 1 of crenulation cleavage.

Stage 1 represents the regional schistosity that is found outside the strain aureole of the pluton. Sample D3005 has a slight crenulation and represents stage 2. Samples D3051, D2010, and Ra36n have a well-developed crenulation cleavage and represent stage 4. Sample D2013 was collected closest to the pluton and also has a pervasive planar foliation at an angle to the regional schistosity, representing stage 5. Figure B2 shows a geologic map of the area east of the Mooselookmeguntic Pluton with the sample localities.

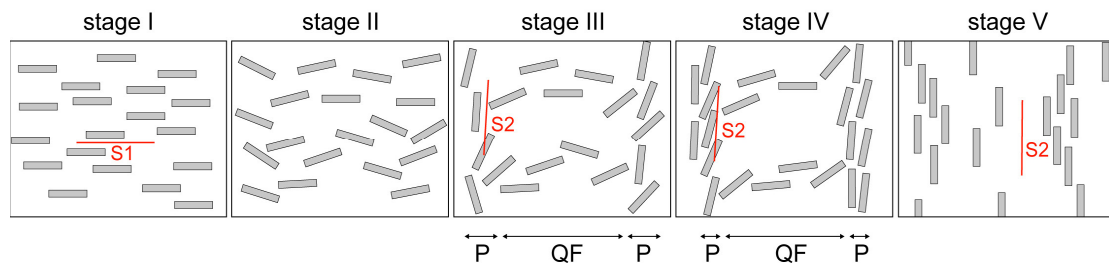


Figure B1. Five stages of crenulation cleavage formation as found in the Mooselookmeguntic Pluton aureole. Stage 1 is the microstructure present outside the pluton strain aureole and has a dominant structural fabric that is the regional schistosity (S1) that is defined by the preferred orientation of muscovite laths and elongate quartz and plagioclase grains. Stage 2 has a moderate crenulation of the regional foliation. At stage 3 the rocks show a well-developed crenulation cleavage. Rocks at stage 4 show a strongly developed crenulation cleavage. At stage 5, a transition from a differentiated cleavage to a pervasive foliation adjacent to the pluton is present in the rocks.

I also studied the CL behavior of quartz in one sample from the Moretown Formation, western Massachusetts. The Moretown Formation represents a forearc basin that was thrust onto Laurentia during the Taconic orogeny (Hatch and Stanley, 1988). The formation is characterized by interbedded schist and quartzite-to-greywacke layers, ranging in thickness from centimeters to meters. During the Acadian orogeny the dominant regional foliation was folded into upright to steeply-dipping westward verging folds (F_3), with amplitudes of meters up to tens of meters (Hatch and Stanley, 1988; Williams et al., 2001). The F_3 folds display a crenulation cleavage that is absent or only weakly developed on fold-limbs and that becomes more intense toward the fold hinges. The sample studied, MT1G1, is from the same slab used by Williams et al. (2001).

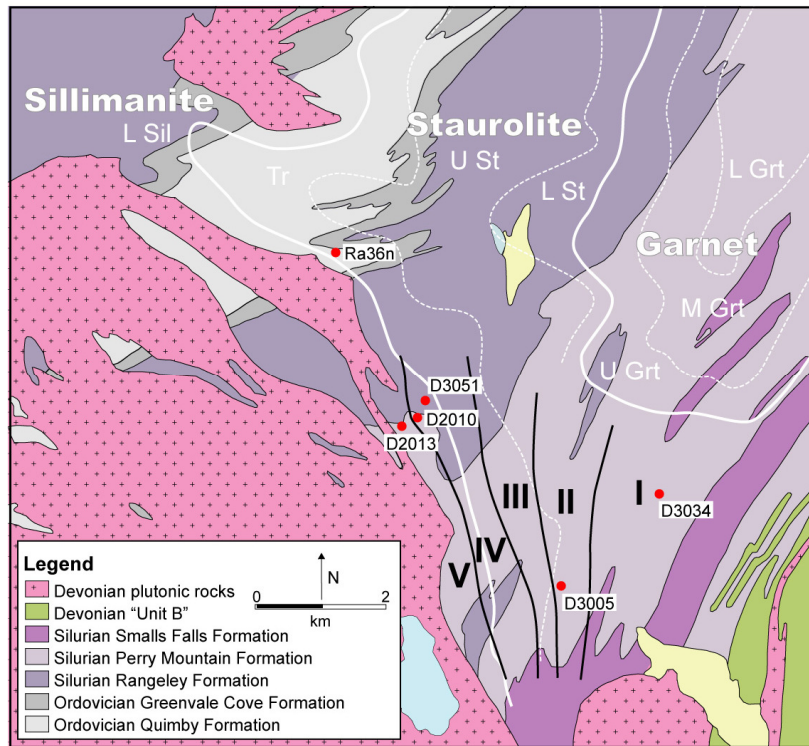


Figure B2. Geological map of the area east of the Mooselokmeguntic Pluton, western Maine showing the sample locations (red dots). The white (dashed) lines indicate metamorphic (sub-) zones. The black lines indicate the zones with the different stages of crenulation cleavage development. Modified from Moench & Hildreth, 1976, Dupee, 2005 and Johnson et al., 2006.

B.3. Cathodoluminescence - Background

Cathodoluminescence (CL) refers to the emission of photons (particles of light within the visible range and UV radiation) by a material that is under bombardment by electrons from a cathode. Luminescence (which literally means “weak glow” in Latin) can also be caused by bombardment from other energy sources: photoluminescence is generated by the bombardment of high-energy UV photons, ionoluminescence is produced by a beam of energetic ions, and x-rays generate radioluminescence (Pagel et al., 2000). The phenomenon of luminescence was first recognized in the seventeenth century, but the method was not used in science until the 1960’s (e.g. Smith and Stenstrom, 1965). Early studies were carried out on a petrographic microscope with an attached cathode gun or by using an electron probe microanalyzer (EPMA). Later the

scanning electron microscope (SEM) was used to generate high-resolution, high-magnification cathodoluminescence images. In geology, CL is mainly used for observations in carbonate and silicate (mainly quartz and feldspars) minerals and zircon. Often zoning displayed by CL is not visible with other kinds of imaging or even chemical mapping.

The reason for CL to occur is linked to the energy from the beam that is applied to the sample and the defects that are present in the valence band of the mineral. When sufficient energy is applied to a mineral, the electrons in the low energy valence band can be excited to the higher energy conduction band. If this happens, a “hole” is left behind in the valence band. Once the energized electrons are in the conduction band they will quickly lose energy ($\sim 10^{-8}$ s) after which they will want to return to the valence band. Defects in the band gap can be considered to be electron traps that shortly intercept and hold electrons as they move through the band gap from the conduction band back to the valence band. When a beam of high energy electrons interacts with a crystal, the energy is partitioned in various ways (X-rays, backscatter electrons, secondary electrons, phonons, etc). Part of the energy of the beam will excite electrons promoting non-localized electrons from the valence band to the conduction band. When the promoted electrons undergo de-excitation and move back to the valence band, the electrons will encounter one or multiple traps, such as point defects, clustered defects (both are extrinsic luminescence centers), impurities, non-stoichiometry, structural imperfections due to radiation damage, shock damage or poor ordering (intrinsic luminescence centers). The presence of traps at discrete energy levels within the band gap is a precondition for emission of photons in the visible light range. If there are no traps present, the electrons fall directly back to the valence band emitting photons with wavelengths in the near UV range. Traps that empty rapidly (timescale of microseconds) produce photons with energies in the near-UV and visible portions of the electromagnetic spectrum. The greater the number of electron traps present in a crystal, the greater the number of CL emissions in the visible range. If the band gap is small, the electrons tend to decay nonradiatively by phonon

emission, rather than radiatively by emission of a photon. The gap to the adjacent lower level needs to have a critical value in order for it to emit photons.

Numerous workers have investigated the relationship between cathodoluminescence color of quartz and provenance. Consensus has been reached regarding the following relationships (e.g. Zinkernagel, 1978; Götze et al., 2001; Boggs and Kringsley, 2006):

- 1) Blue to violet CL: plutonic quartz (commonly more red-violet), as well as quartz phenocrysts in volcanic rock, and high-grade metamorphic (or contact metamorphic) quartz ($T > 573^{\circ}\text{C}$ and fast cooling conditions);
- 2) Red CL: matrix quartz in volcanic rocks;
- 3) Brown CL: quartz from high and low grade regional metamorphic rocks, metamorphized igneous rocks, contact metamorphic rocks, metasediments;
- 4) No CL or weakly luminescent: authigenic quartz in sediments ($T < 300^{\circ}\text{C}$);
- 5) Short-lived green or blue CL: hydrothermal and pegmatitic quartz.

Boggs et al. (2002) stated that CL color is not a reliable indicator of quartz provenance because the CL colors of metamorphic quartz exhibit a wide variation, overlapping both the color fields of volcanic and plutonic quartz. Another common problem with CL color studies is that the CL color changes with increasing radiation of the sample, commonly a shift from blue toward red is observed (e.g. Sippel, 1968; Zinkernagel, 1978). According to Richter et al., 2003, the nature of color shift can have provenance significance as well. The most frequently observed color in feldspars is blue CL. There is no definite relationship between the CL colors of feldspar and provenance. Observing CL color in a cathodoluminescence microscope is a subjective process, therefore, it is common practice to gather CL spectra with a spectrometer in addition to CL images (e.g. Gaft et al., 2005; Boggs and Kringsley, 2006). Factors that can influence the color of a CL image are: the sample temperature, the beam current, the acceleration voltage, the contrast and brightness, the magnification, the collection time, the carbon coat thickness, and the distance between sample and detector (Boggs and Kringsley, 2006).

The blue CL color in metamorphic and plutonic quartz is often linked to the presence of trace elements of Ti in the crystal lattice. The amount of Ti in quartz can be used as a geothermometer, using TitaniQ (Wark and Watson, 2006; Spear and Wark, 2009). Other possible trace elements in quartz that can cause CL are Al, K, Li, Na, Fe, P (e.g. Marshall, 1988; Demars et al., 1996; Götze et al., 2001; Rusk et al., 2006). Other workers state that CL in quartz is mainly caused by structural defects (e.g. Götze et al., 2001; Richter et al., 2003). In order to obtain information on the cause(s) of cathodoluminescence (or the nature of the luminescence centers) additional techniques and instruments are necessary. For trace-element analysis common techniques include EPMA, secondary ion mass spectrometry (SIMS), laser-ablation-inductivity coupled plasma mass spectrometry (LA-ICP-MS), and particle-induced X-ray emission (PIXE and micro-PIXE). An example of a technique for evaluating defects in crystal structures is electron paramagnetic resonance (EPR).

CL is used by workers to study pressure solution and its influence on porosity in sedimentary rocks (e.g Sprunt and Nur, 1977; Evans et al., 1994). CL is useful for this because the intergranular relationships and pore spaces are very distinct, although caution must be used when interpreting natural examples because of the change in luminescence with time. It is sometimes possible to differentiate between a detrital grain and an authigenic overgrowth if the two types of quartz contain different impurities or crystal defects. Detrital quartz commonly appears bright, whereas the overgrowths are dark. Although the rocks from the Mooselookmeguntic Pluton aureole and the Moretown Formation are metamorphic in nature, I expect that the mass transfer of quartz during crenulation cleavage will show comparable grains with overgrowths.

B.4. Method

B.4.1. Cathodoluminescence

In order to investigate the mass transfer of quartz during crenulation cleavage formation CL images were taken from several samples at different stages of crenulation cleavage development. The CL, and simultaneously derived SEM, images were taken using the Gatan ChromaCL detector on the Tescan Vega Scanning Electron Microscope at the University of Maine's Department of Earth Sciences. The images were collected from untilted, carbon coated samples at a working distance of 12 mm, using a 20 kV acceleration voltage and a beam current of ~11nA. In order to minimize changes in the CL color from beam damage, the images were taken as soon as possible once the location of interest was reached. To get a good idea of the presence and geometry of overgrowths in the different domains of crenulation cleavage and because of limitations in field of view, a mosaic of images (up to 260) was collected across the different domains (P and QF). The images were manually stitched in Adobe's Illustrator, with a different layer for each of the following: SEM images, the colored CL images, and, in some cases, just the blue component of the color CL images.

B.4.2. Chemical Analysis

Because the blue CL color in metamorphic quartz is associated with the presence of trace amounts of titanium, I used the Cameca SX-100 electron microprobe at the University of Maine to determine if measurable amounts of Ti are present in the samples of the Mooselookmeguntic Pluton aureole and if these amounts could be used to calculate peak temperature conditions using the TitaniQ (Ti in quartz) geothermometer (Wark and Watson, 2006). Ti K-alpha X-rays were counted simultaneously using PET crystals on four spectrometers from which the results were averaged. The carbon coated samples were analyzed using a 15kV, 150nA, 20µm beam with a counting time of 300 seconds. Fifteen point measurements per region (core or rim) were taken for each grain (4 grains in total). The electron microprobe was calibrated using a rutile standard.

Detection limits and analytical error were determined using a 95% confidence level of peak and background measurements (adapted Love and Scott, 1978). With the number of measurements taken (15), the detection limit is 29.4 ppm.

B.5. Results

The CL behavior of quartz grains in samples representing different stages of crenulation cleavage is studied to identify overgrowths and relate them to mass transfer of quartz during the formation of this fabric. In the Mooselookmeguntic Pluton samples the quartz grains have a reddish/blue color that shifts to orange/red over time with accumulated beam damage. The plagioclase grains in these samples have a bright blue color. Other minerals in these samples show no CL. The CL of the quartz grains display red colors at the grain boundaries. Most grains show a gradation of color from red to blue within the grain (Figure B3a-d, f). Other quartz grains show a distinct blue core with a gradation to red in the rim (Figure B3e, g-l). These blue cores commonly display filled fractures that are not visible with the light microscope or SEM (Figure B3h, j-l).

In the Moretown sample, the quartz grains have a gradation of colors from bright orange to darker orange. The plagioclase grains display clearly the core and rim features that were reported by Williams et al. (2001): in CL the An_3 cores are red and the An_{14-16} rims are blue (Figure B4). The blue component of the color CL images display core and rim features in the quartz grains that are not visible in the full spectrum images. Other minerals in this sample show no CL.

B.5.1. CL of Quartz per Stage – Mooselookmeguntic Pluton Aureole Samples

The quartz grains in the samples furthest away from the pluton (stage I and II of crenulation cleavage development) typically display the color gradation from blue to red without a clear core-rim boundary (Figure B3a-d). In the samples collected closer to the pluton (stage IV

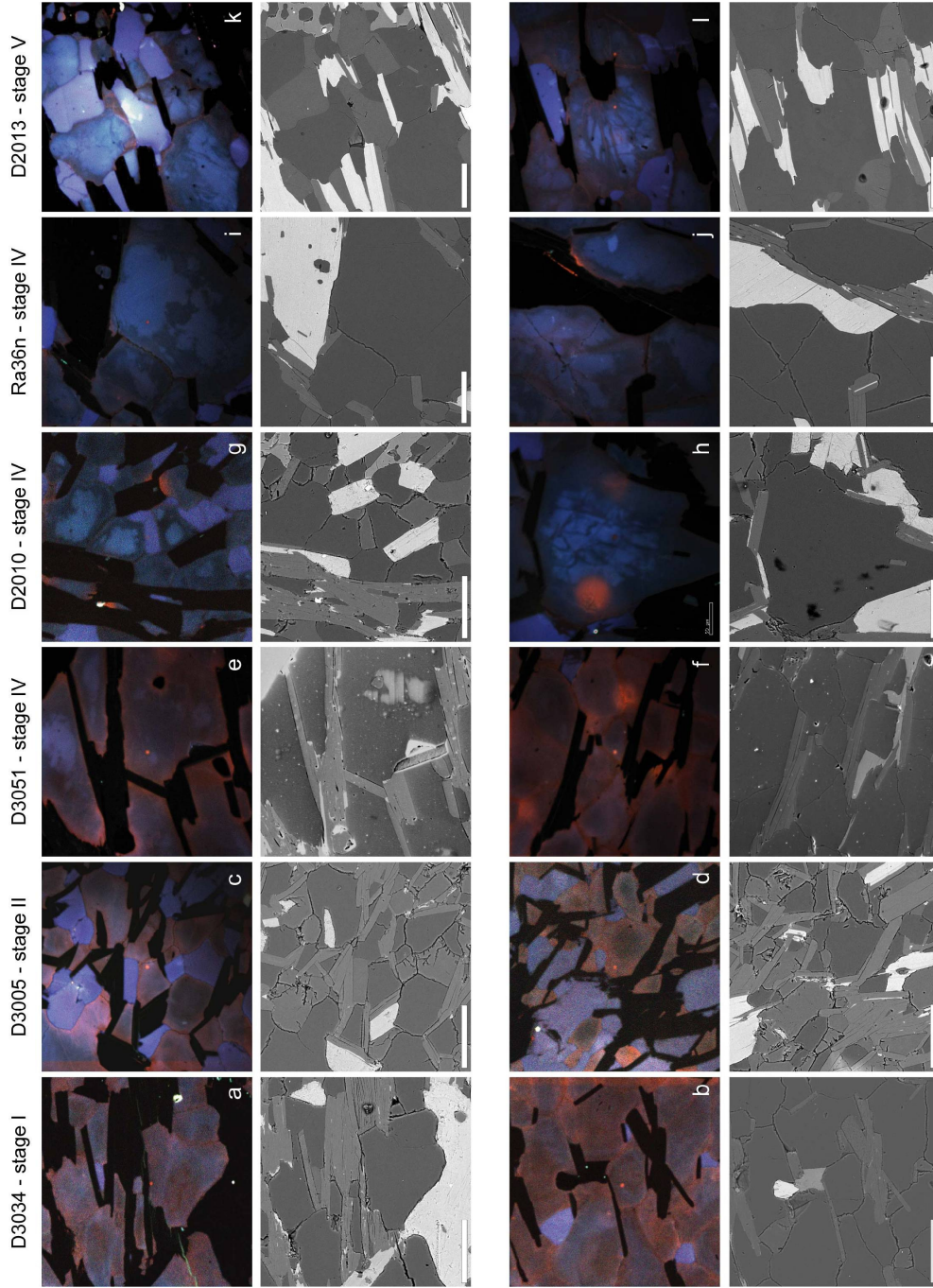


Figure B3. Color CL and corresponding BSE images of specific features within each sample from the Mooselookmeung Pluton aureole. In all color CL images, the bright blue grains are plagioclase grains, the red-blue grains are quartz, and the grains with no CL (black) are muscovite and/or biotite. An explanation of the displayed features can be found in the text. The scale bars in the BSE images are all 100 μ m.

and V), the quartz grains show similar CL structures, but in these samples, grains are also present that have bright blue cores. These cores commonly show healed fractures (Figure B3h, j-l) and can be shaped very irregularly (Figure B3h-l). The fractures in the grain in Figure B3l show a radiating pattern off a biotite grain. The healed fractures are only visible in the bright blue cores.

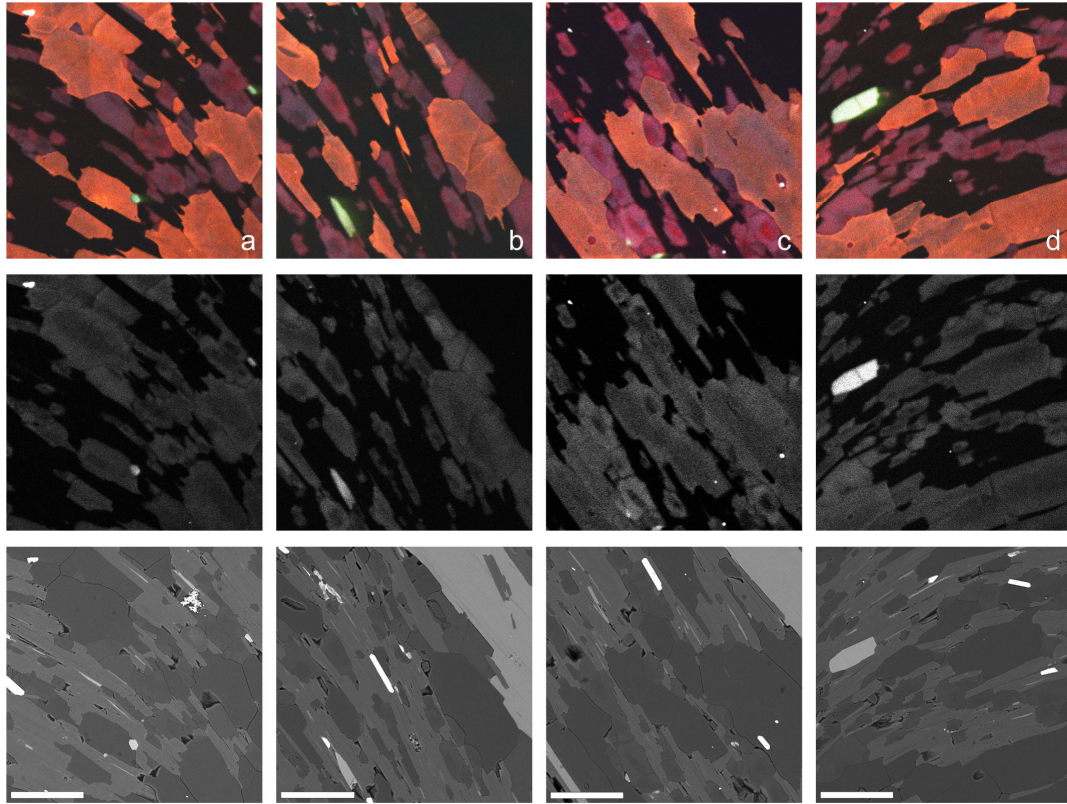


Figure B4. Color CL and corresponding blue component CL and BSE images for sample MT1G1. The orange grains in the color CL images are quartz grains, the red and blue grains are plagioclase, and the grains with no CL (black) are muscovite and/or biotite. More explanation on the features in this figure can be found in the text. The scale bars in the BSE images are all 100 μ m.

B.5.2. CL of Quartz per Domain – Mooslookmeguntic Pluton Aureole Samples

Color CL mosaic maps of several mm² are made per sample (containing both P and QF domains for stage IV samples) to get a better indication of the spatial variation of the structures described above. Figure B5 shows the map of sample D3034. The quartz grains in this sample show the gradation of blue to red colors as also shown in Figures B3a-d. None of the grains have distinct cores and rims. Figure B6 and B7 show the mosaics of samples D3051 and Ra36n, both

with a well developed crenulation cleavage. Although the quartz grains in the P-domains are smaller, they do contain bright blue cores as well. Sample Ra36n has much more plagioclase and quartz grains with bright blue cores. The shapes of the cores are irregular. Unlike the other stage IV and the stage V samples, the sampled area of sample D3051 shows no healed fractures.

B.5.3. CL of Quartz – Moretown Formation Sample

The color CL mosaic map of sample MT1G1 is shown in Figure B8. The traced cores in the quartz grains are based on observations in the blue component images. The cores are elongated and aligned with the S_2 fabric. The mapped P-domain has little to no quartz, and cores and rims could not be distinguished in the few quartz grains that are present in this domain.

B.5.4. Ti Concentrations

Four grains with bright blue CL cores from sample Ra36n were chemically analyzed for Ti using the electron microprobe. Fifteen point measurements were taken in each core and the same amount of measurements were taken in the rim of each grain. The results can be found in Figures B9 and B10, and Table B1. Figure B9 shows the wt% Ti (averaged from the 4 spectrometers) per measured point. Table B1 shows the average concentration per region (core or rim) for each grain. The table shows both the average amount of Ti per region of the raw data and the data that excludes certain measurements. Figure B10 shows the wt% Ti per spectrometer per measured point. The outcomes are non-conclusive; the concentrations of Ti were all below 0.003 wt%, which is below the detection limit. There was no pattern between the averages of the cores and the rims. In 3 out of the 4 grains the concentrations of Ti appeared to be higher in the rim than in the core. Yet, considering the results of the individual spectrometers, the variation appears to be large for a number of measurements. Especially the values of Ti SP5/1 appear to be significantly different in comparison to the values of other spectrometers for a large number of measurements.

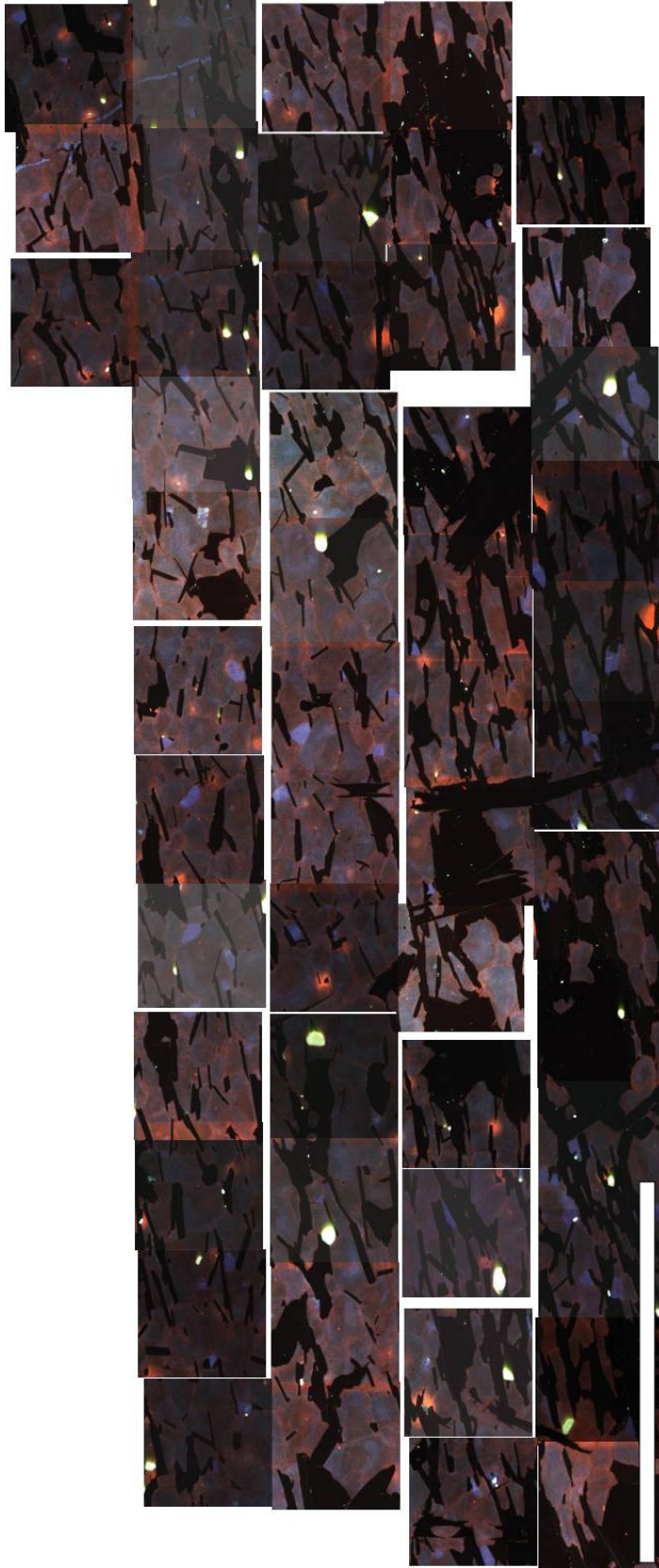


Figure B5. Mosaic of color CL images of sample D3034 (stage D). The bright blue grains are plagioclase grains, the red-blue grains are quartz, and the grains with no CL (black) are muscovite and/or biotite. The scale bar has a width of 1 mm. An explanation of the displayed features can be found in the text.

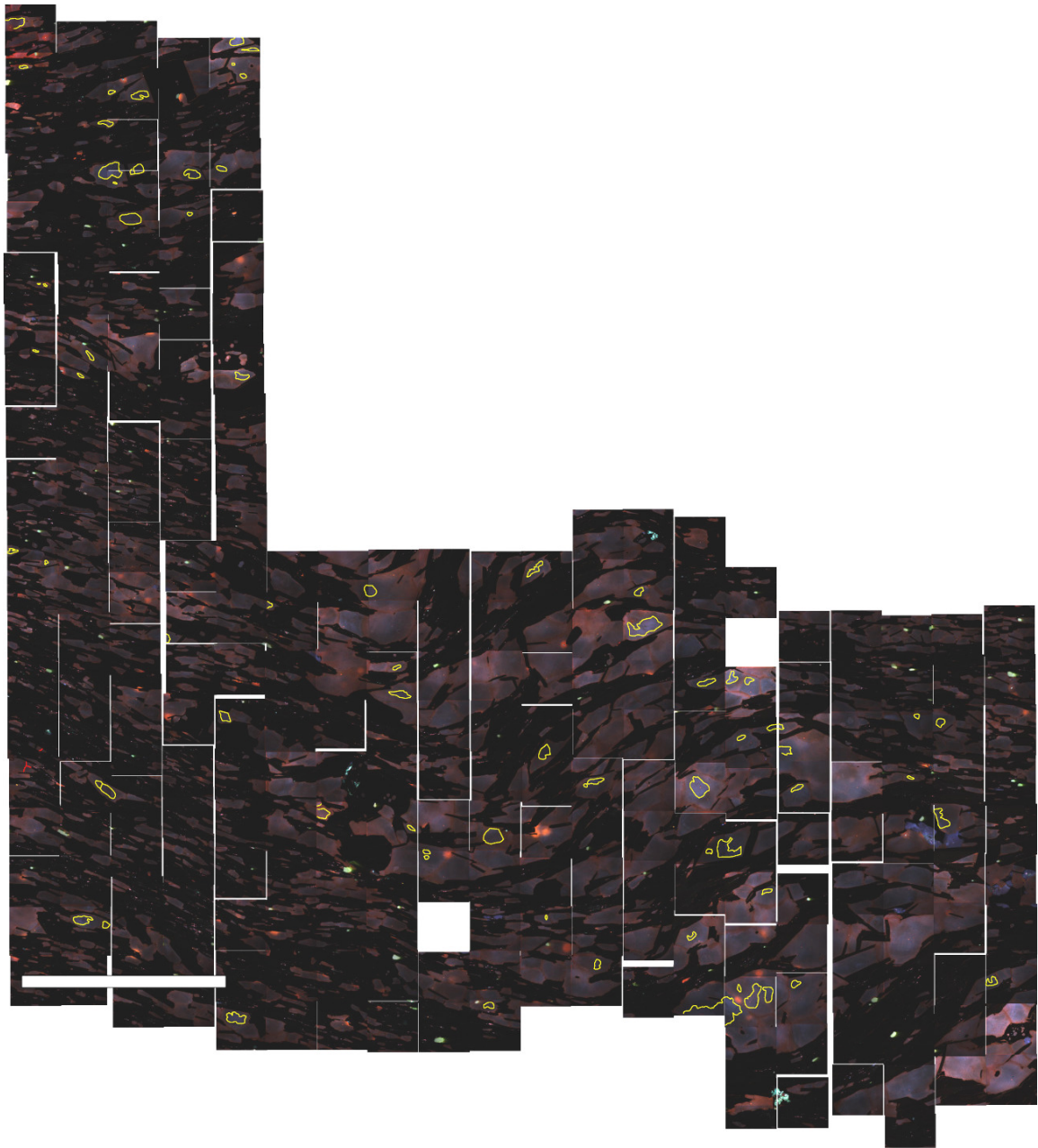


Figure B6. Mosaic of color CL maps of sample D3051 (stage IV). The bright blue grains are plagioclase grains, the red-blue grains are quartz, and the grains with no CL (black) are muscovite and/or biotite. The scale bar has a width of 1 mm. Bright blue cores in the quartz grains are outlined in yellow. More explanation can be found in the text.

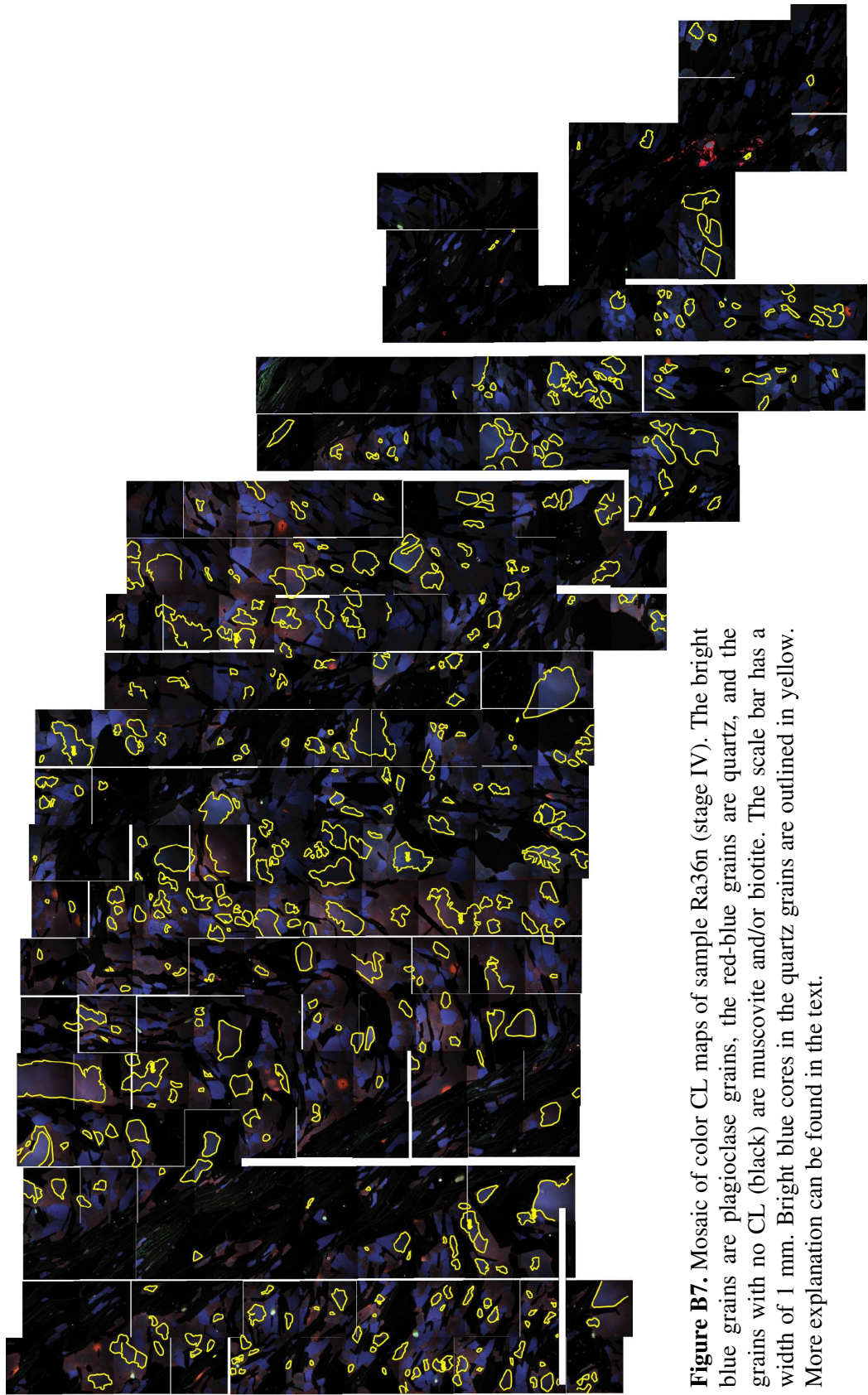


Figure B7. Mosaic of color CL maps of sample Ra36n (stage IV). The bright blue grains are plagioclase grains, the red-blue grains are quartz, and the grains with no CL (black) are muscovite and/or biotite. The scale bar has a width of 1 mm. Bright blue cores in the quartz grains are outlined in yellow. More explanation can be found in the text.

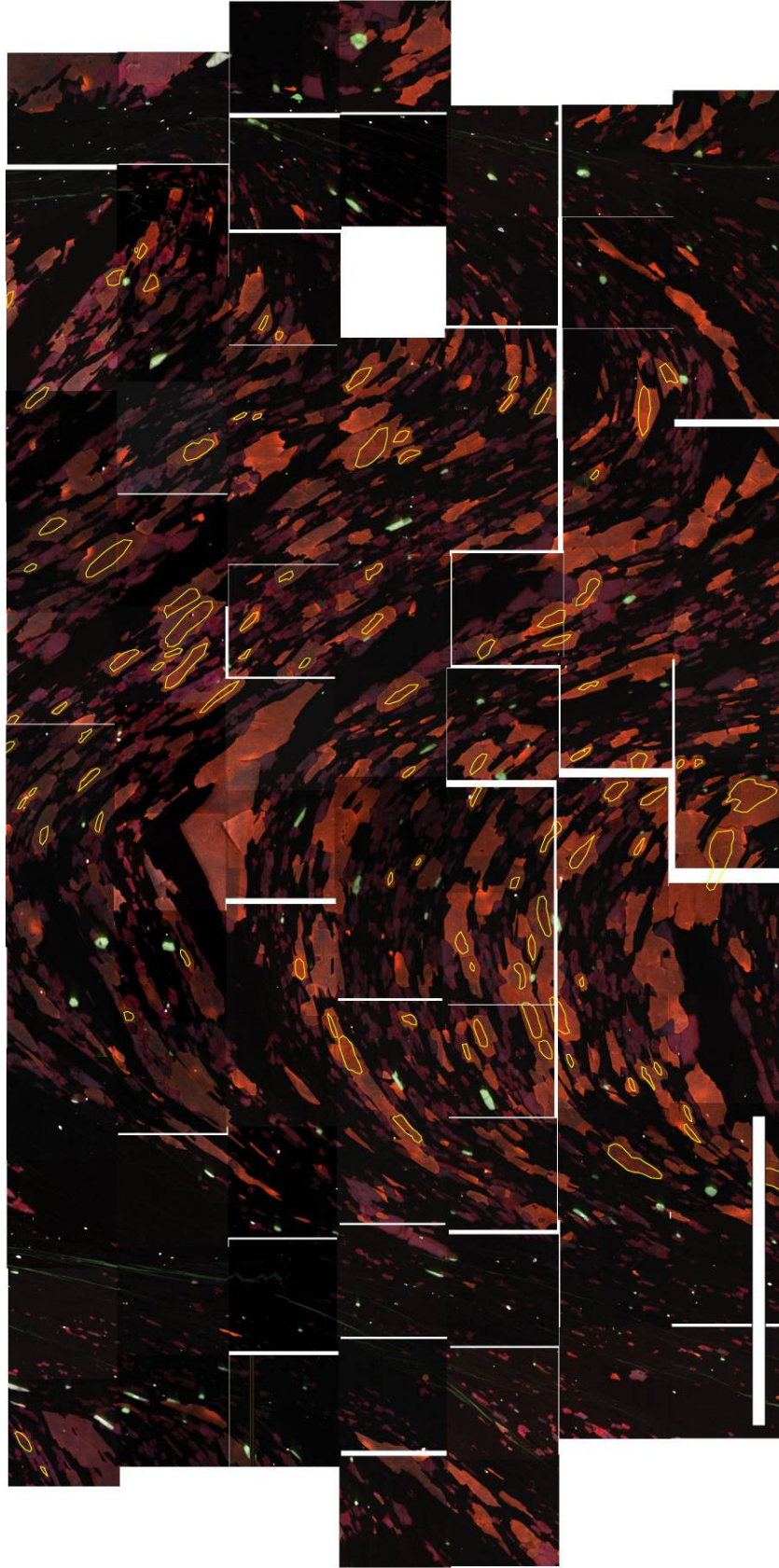


Figure B8. Mosaic of color CL maps of sample MT1G1. The orange grains are quartz, the red and blue grains are plagioclase, and the grains with no CL (black) are muscovite and/or biotite. Cores that could be identified in quartz grains in the blue component images (not shown here) are outlined in yellow. The scale bar has a width of 1 mm. More explanation on the features in this figure can be found in the text.

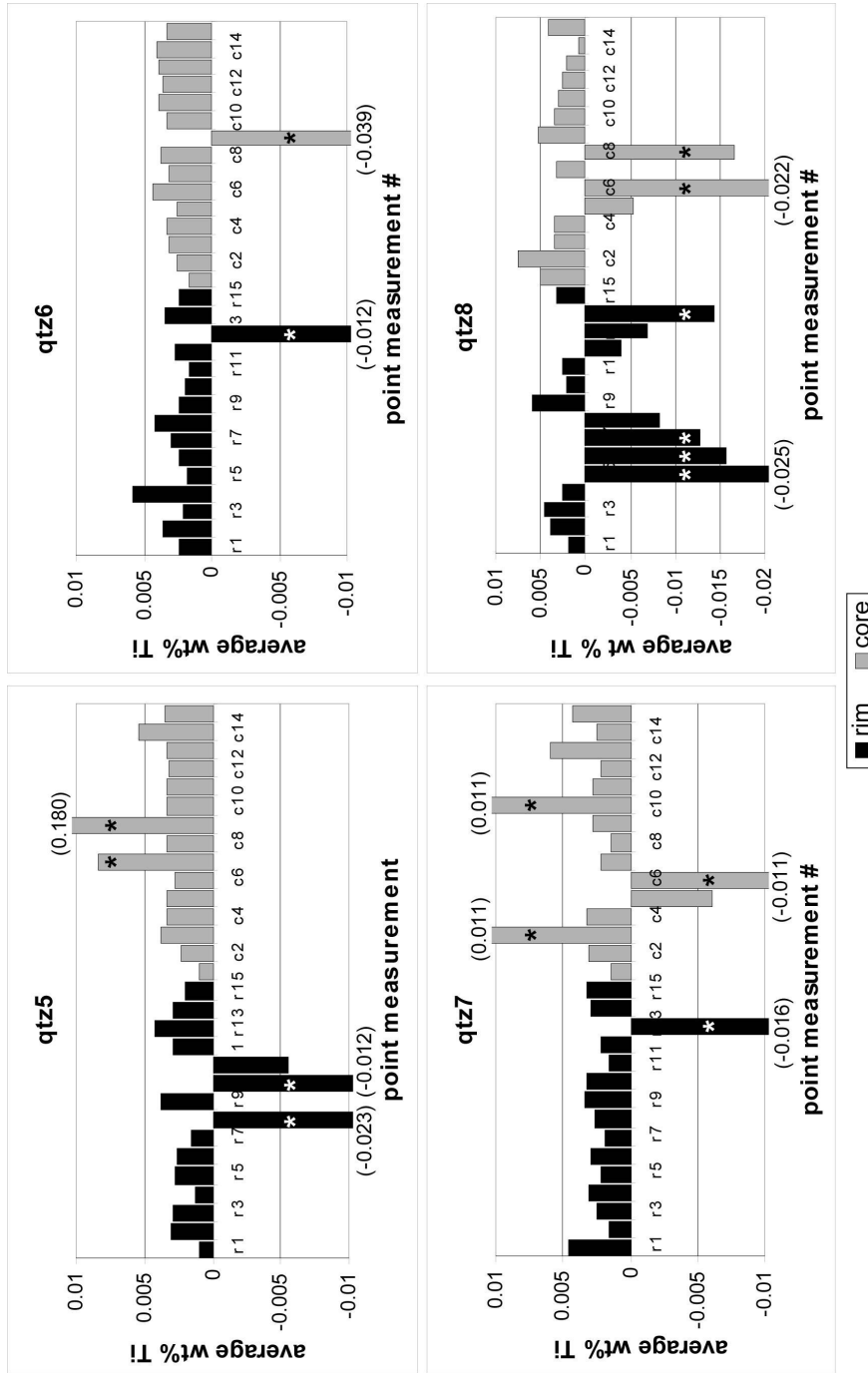


Figure B9. Average wt% of Ti per point measurements for 4 quartz grains from sample Ra36n. The measurements with a star inside are statistically off and not taken into consideration in the calculation of the average wt% of Ti in the rim and core (see also table 1).

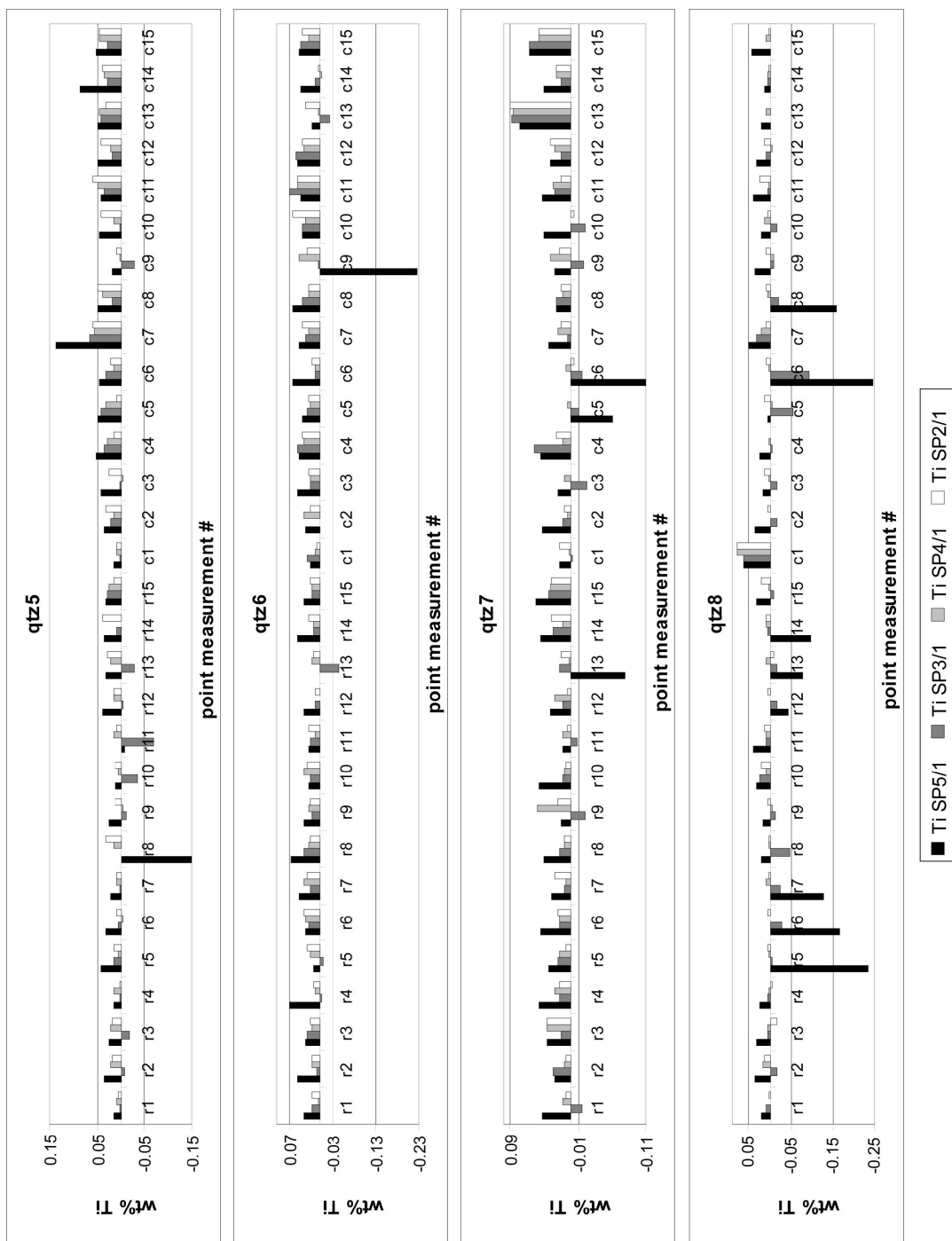


Figure B10. Wt% of Ti per point measurement per individual spectrometer for four quartz grains from sample Ra36n. (See also table 1)

Table B1. Probe analysis measurements of wt% Ti for four quartz grains from sample Ra36n. The tables show average wt% Ti from the four spectrometers and the individual spectrometer measurements. The average concentration per rim and core are also shown

| qtz5 | | | | | | | | | | | qtz6 | | | | | | | | | | |
|------------------|------------|----------|------------------|-----------------------------------|----------|------------------|------------|------------------|-----------------------------------|----------|----------|--|--|--|--|--|--|--|--|--|--|
| Point | Ti average | Ti SP5/1 | Ti SP3/1 | Ti SP4/1 | Ti SP2/1 | Point | Ti average | Ti SP5/1 | Ti SP3/1 | Ti SP4/1 | Ti SP2/1 | | | | | | | | | | |
| rim 1 | 0.001022 | 0.014735 | 0.000721 | 0.006909 | 0.004014 | rim 1 | 0.002371 | 0.035926 | 0.020007 | 0.003141 | 0.019442 | | | | | | | | | | |
| rim 2 | 0.002963 | 0.036961 | -0.00949 | 0.02203 | 0.017695 | rim 2 | 0.003556 | 0.052999 | 0.006801 | 0.017757 | 0.018704 | | | | | | | | | | |
| rim 3 | 0.002857 | 0.025226 | -0.01763 | 0.020438 | 0.01825 | rim 3 | 0.00212 | 0.032477 | 0.030699 | 0.019503 | 0.020505 | | | | | | | | | | |
| rim 4 | 0.001193 | 0.016297 | 0.002951 | 0.01586 | 0.001598 | rim 4 | 0.005872 | 0.07075 | -0.00225 | 0.011602 | 0.014211 | | | | | | | | | | |
| rim 5 | 0.002703 | 0.040509 | 0.013723 | 0.005402 | 0.015369 | rim 5 | 0.001864 | 0.015024 | -0.00717 | 0.021543 | 0.029937 | | | | | | | | | | |
| rim 6 | 0.002536 | 0.030347 | 0.006707 | -0.00429 | 0.009756 | rim 6 | 0.002368 | 0.033358 | 0.024653 | 0.033487 | 0.035542 | | | | | | | | | | |
| rim 7 | 0.001499 | 0.021737 | 0.000589 | 0.008235 | 0.009209 | rim 7 | 0.003048 | 0.048842 | 0.021692 | 0.037299 | 0.028382 | | | | | | | | | | |
| rim 8 | -0.02344 | -0.14918 | -0.00205 | 0.014117 | 0.032606 | rim 8 | 0.004167 | 0.067055 | 0.038156 | 0.027592 | 0.020584 | | | | | | | | | | |
| rim 9 | 0.003807 | 0.02486 | -0.01042 | -0.00543 | 0.013441 | rim 9 | 0.002322 | 0.037645 | 0.018768 | 0.024902 | 0.023243 | | | | | | | | | | |
| rim 10 | -0.01152 | 0.011859 | -0.03548 | 0.004755 | 0.010192 | rim 10 | 0.001989 | 0.024863 | 0.022919 | 0.035431 | 0.028154 | | | | | | | | | | |
| rim 11 | -0.00563 | -0.00837 | -0.06803 | 0.014707 | 0.007159 | rim 11 | 0.001704 | 0.025058 | 0.020801 | 0.010052 | 0.024616 | | | | | | | | | | |
| rim 12 | 0.002917 | 0.03884 | -0.00456 | 0.014993 | 0.016824 | rim 12 | 0.002621 | 0.035885 | 0.010472 | 0.000012 | 0.011862 | | | | | | | | | | |
| rim 13 | 0.004295 | 0.032915 | -0.02751 | 0.022295 | 0.029196 | rim 13 | -0.01217 | -0.00082 | -0.04492 | 0.019249 | 0.013591 | | | | | | | | | | |
| rim 14 | 0.002955 | 0.036998 | 0.00969 | -0.00313 | 0.037132 | rim 14 | 0.00338 | 0.053224 | 0.01605 | 0.015193 | 0.025679 | | | | | | | | | | |
| rim 15 | 0.002043 | 0.031274 | 0.028085 | 0.024312 | 0.013906 | rim 15 | 0.002318 | 0.037984 | 0.017716 | 0.0191 | 0.02149 | | | | | | | | | | |
| core 1 | 0.000932 | 0.014775 | 0.003252 | 0.008144 | 0.008487 | core 1 | 0.001632 | 0.021602 | 0.029458 | 0.010976 | 0.007463 | | | | | | | | | | |
| core 2 | 0.002227 | 0.033854 | 0.020373 | 0.01485 | 0.032325 | core 2 | 0.002578 | 0.034331 | -0.00139 | 0.037318 | 0.021656 | | | | | | | | | | |
| core 3 | 0.003824 | 0.043267 | 0.000516 | -0.00601 | 0.025777 | core 3 | 0.003169 | 0.051803 | 0.02286 | 0.021697 | 0.025928 | | | | | | | | | | |
| core 4 | 0.003286 | 0.052419 | 0.035534 | 0.028064 | 0.014803 | core 4 | 0.003275 | 0.046659 | 0.050986 | 0.035138 | 0.04115 | | | | | | | | | | |
| core 5 | 0.003337 | 0.050212 | 0.043392 | 0.032496 | 0.009059 | core 5 | 0.002544 | 0.041013 | 0.028375 | 0.02201 | 0.02514 | | | | | | | | | | |
| core 6 | 0.002766 | 0.04401 | 0.031952 | 0.014973 | 0.020883 | core 6 | 0.004354 | 0.062224 | 0.011284 | 0.010012 | 0.020146 | | | | | | | | | | |
| core 7 | 0.008334 | 0.136184 | 0.066116 | 0.056846 | 0.057465 | core 7 | 0.003112 | 0.049007 | 0.033008 | 0.025479 | 0.039011 | | | | | | | | | | |
| core 8 | 0.003321 | 0.049722 | 0.019468 | 0.037436 | 0.048145 | core 8 | 0.0038 | 0.061373 | 0.0041514 | 0.02552 | 0.026902 | | | | | | | | | | |
| core 9 | 0.180334 | 0.01791 | -0.02728 | 0.000267 | 0.009574 | core 9 | -0.0388 | -0.22528 | 0.003769 | 0.04904 | 0.028268 | | | | | | | | | | |
| core 10 | 0.003396 | 0.04701 | 0.000817 | 0.015272 | 0.040527 | core 10 | 0.00332 | 0.041656 | 0.038954 | 0.034072 | 0.061968 | | | | | | | | | | |
| core 11 | 0.003375 | 0.042531 | 0.03619 | 0.050354 | 0.057664 | core 11 | 0.003883 | 0.044988 | 0.070581 | 0.053449 | 0.052041 | | | | | | | | | | |
| core 12 | 0.003232 | 0.050235 | 0.018666 | 0.022387 | 0.042397 | core 12 | 0.003603 | 0.053152 | 0.054473 | 0.035969 | 0.041702 | | | | | | | | | | |
| core 13 | 0.003297 | 0.050246 | 0.041249 | 0.044598 | 0.031195 | core 13 | 0.003931 | 0.0174 | -0.02151 | 0.004307 | 0.035011 | | | | | | | | | | |
| core 14 | 0.005344 | 0.08644 | 0.030005 | 0.035441 | 0.038215 | core 14 | 0.003968 | 0.044586 | 0.010149 | -0.00408 | 0.004895 | | | | | | | | | | |
| core 15 | 0.003479 | 0.052983 | 0.029129 | 0.044222 | 0.046474 | core 15 | 0.003227 | 0.048226 | 0.04573 | 0.026723 | 0.04031 | | | | | | | | | | |
| average wt% rim | | | all measurements | highlighted measurements excluded | | average wt% rim | | all measurements | highlighted measurements excluded | | | | | | | | | | | | |
| average wt% core | | | 0.001935 | 0.002462 | | average wt% core | | 0.002836 | 0.00112 | | | | | | | | | | | | |
| | | | 0.003217 | 0.000977 | | | | 0.003314 | 0.000711 | | | | | | | | | | | | |

Table B1 (continued). Probe analysis measurements of wt% Ti for four quartz grains from sample Ra36n. The tables show average wt% Ti from the four spectrometers and the individual spectrometer measurements. The average concentration per rim and core are also shown.

| qtz7 | | qtz8 | | | | | | | | | |
|------------------|------------|-----------------------------------|----------|----------|----------|---------|------------|----------|-----------|----------|----------|
| Weight% | | Weight% | | | | | | | | | |
| Point | Ti average | Ti SP5/I | Ti SP3/I | Ti SP4/I | Ti SP2/I | Point | Ti average | Ti SP5/I | Ti SP3/I | Ti SP4/I | Ti SP2/I |
| rim 1 | 0.004648 | 0.044272 | -0.01508 | 0.012925 | 0.00897 | rim 1 | 0.001794 | 0.02059 | 0.008727 | -0.00356 | 0.002662 |
| rim 2 | 0.001652 | 0.023783 | 0.0268 | 0.010996 | 0.008693 | rim 2 | 0.003973 | 0.037563 | -0.01782 | 0.017089 | 0.012771 |
| rim 3 | 0.002495 | 0.035438 | 0.015509 | 0.035653 | 0.036725 | rim 3 | 0.004489 | 0.034301 | 0.007311 | 0.007786 | -0.01627 |
| rim 4 | 0.003039 | 0.049148 | 0.018241 | 0.025131 | 0.017002 | rim 4 | 0.002576 | 0.025782 | 0.005643 | 0.003354 | -0.00555 |
| rim 5 | 0.002142 | 0.034261 | 0.020043 | 0.017129 | 0.008653 | rim 5 | -0.02509 | -0.23398 | -0.00715 | 0.002964 | 0.005635 |
| rim 6 | 0.002865 | 0.04615 | 0.016485 | 0.01678 | 0.020712 | rim 6 | -0.0157 | -0.16591 | -0.0285 | -0.00351 | 0.007825 |
| rim 7 | 0.001917 | 0.02923 | 0.011496 | 0.008323 | 0.024747 | rim 7 | -0.01285 | -0.12656 | -0.02361 | 0.010336 | 0.003931 |
| rim 8 | 0.002607 | 0.040331 | 0.018132 | 0.010095 | 0.010596 | rim 8 | -0.00827 | 0.021902 | -0.04657 | 0.009937 | 0.001471 |
| rim 9 | 0.003454 | 0.015769 | -0.02088 | 0.049703 | 0.020536 | rim 9 | 0.005898 | 0.015757 | -0.01224 | -0.00415 | 0.00742 |
| rim 10 | 0.003289 | 0.047141 | 0.011946 | 0.011217 | 0.007666 | rim 10 | 0.002097 | 0.032924 | 0.024546 | 0.009752 | 0.019784 |
| rim 11 | 0.001568 | 0.012638 | -0.00968 | 0.012563 | 0.006707 | rim 11 | 0.002551 | 0.038771 | 0.009874 | 0.009006 | 0.014348 |
| rim 12 | 0.002157 | 0.032719 | 0.011946 | 0.025197 | 0.005102 | rim 12 | -0.00405 | -0.04372 | -0.01787 | -0.00157 | 0.007269 |
| rim 13 | -0.01647 | -0.07821 | 0.017715 | 0.003266 | 0.015562 | rim 13 | -0.00682 | -0.0767 | -0.01769 | 0.008205 | -0.00989 |
| rim 14 | 0.002872 | 0.045621 | 0.027978 | 0.013696 | 0.030005 | rim 14 | -0.01433 | -0.09832 | 0.004852 | 0.010827 | 0.009843 |
| rim 15 | 0.003227 | 0.052321 | 0.034496 | 0.032002 | 0.028223 | rim 15 | 0.003281 | 0.034579 | -0.00891 | 0.001921 | 0.021913 |
| core 1 | 0.0014 | 0.017148 | -0.00144 | 0.002637 | 0.01633 | core 1 | 0.005059 | 0.063956 | 0.063227 | 0.078324 | 0.080422 |
| core 2 | 0.00308 | 0.044448 | 0.013532 | 0.006358 | 0.010699 | core 2 | 0.007434 | 0.035032 | -0.01824 | -0.00285 | 0.006825 |
| core 3 | 0.011381 | 0.020943 | -0.02363 | 0.009979 | 0.000336 | core 3 | 0.003532 | 0.01842 | -0.01518 | 0.00159 | 0.011993 |
| core 4 | 0.003292 | 0.045514 | 0.054541 | 0.012295 | 0.02142 | core 4 | 0.003415 | 0.026163 | -0.00623 | 0.003621 | -0.00126 |
| core 5 | -0.00614 | -0.06088 | -0.01118 | 0.006436 | -0.00028 | core 5 | -0.00542 | 0.005804 | -0.05563 | -0.00405 | 0.015336 |
| core 6 | -0.01083 | -0.10954 | -0.01537 | 0.008852 | -0.00379 | core 6 | -0.02162 | -0.24672 | -0.09171 | 0.002924 | 0.011478 |
| core 7 | 0.002161 | 0.03354 | 0.005135 | 0.019388 | 0.014124 | core 7 | 0.003211 | 0.050163 | 0.032265 | 0.019395 | 0.010497 |
| core 8 | 0.001487 | 0.02282 | 0.021468 | 0.013395 | 0.01433 | core 8 | -0.01663 | -0.15858 | -0.01898 | 0.006098 | 0.008707 |
| core 9 | 0.002802 | 0.023434 | -0.01734 | 0.031945 | 0.018414 | core 9 | 0.005277 | 0.03787 | -0.00901 | -0.00788 | 0.011033 |
| core 10 | 0.01117 | 0.040333 | -0.01944 | 0.000764 | -0.00399 | core 10 | 0.00349 | 0.021978 | -0.01734 | 0.012406 | 0.006267 |
| core 11 | 0.002721 | 0.0441 | 0.023878 | 0.027969 | 0.015253 | core 11 | 0.003094 | 0.042174 | 0.006834 | 0.000791 | 0.025641 |
| core 12 | 0.002112 | 0.03142 | 0.014939 | 0.024997 | 0.031273 | core 12 | 0.002639 | 0.033701 | 0.010224 | -0.00432 | 0.013177 |
| core 13 | 0.006015 | 0.076972 | 0.088695 | 0.086154 | 0.089897 | core 13 | 0.002132 | 0.022941 | -0.00279 | 0.009353 | -0.00058 |
| core 14 | 0.002497 | 0.040761 | 0.016227 | 0.021974 | 0.023034 | core 14 | 0.000783 | 0.011831 | -0.004138 | 0.004327 | 0.001724 |
| core 15 | 0.004236 | 0.062764 | 0.061537 | 0.048668 | 0.048614 | core 15 | 0.004034 | 0.044155 | -0.00323 | 0.010586 | 0.001785 |
| all measurements | | all measurements | | | | | | | | | |
| average wt% rim | | average wt% rim | | | | | | | | | |
| average wt% core | | average wt% core | | | | | | | | | |
| | | highlighted measurements excluded | | | | | | | | | |
| | | highlighted measurements excluded | | | | | | | | | |
| | | 0.00478 | | | | | | | | | |
| | | 0.002994 | | | | | | | | | |

B.6. Discussion

Color CL images were acquired from samples from the Mooselookmeguntic Pluton aureole and the Moretown Formation to investigate the mass transfer of quartz during crenulation cleavage formation. Williams et al. (2001) showed that during crenulation cleavage formation overgrowths with a different chemical composition formed on plagioclase grains in the Moretown Formation; similar observations are expected for quartz. Because of a lack of chemical variability in quartz, CL imaging was used instead of chemical mapping to display internal grain-structures. Mosaics were made for mm² scale regions to investigate the spatial variation of the structures found in the quartz grains.

B.6.1. Mooselookmeguntic Pluton Aureole

B.6.1.1. Core-Rim Geometries. The results of the Mooselookmeguntic Pluton aureole show that samples collected furthest from the pluton contain quartz grains that are mottled, with color gradations from red to blue. In most grains, the grain boundaries appear red, turning more blue towards the center and darker/reddish at the center. There are no clear core-rim boundaries in the grains from samples furthest from the pluton. In samples collected closer to the pluton, more grains do show clear core-rim boundaries within quartz grains. The cores in these grains are bright blue, irregularly-shaped, and commonly contain fractures that are healed and not visible with light-microscopy or SEM. One of the goals of this study was to quantify the mass transfer from quartz during crenulation cleavage formation, but because the cores and rims in the quartz grains in the studied samples from the Mooselookmeguntic Pluton aureole appear to not have geometries that can be linked to the crenulation cleavage formation this cannot be done with the samples studied.

B.6.1.2. Ti in Quartz. The concentration of bright blue cores is variable between samples with a stage IV crenulation cleavage, but it appears that the concentration is highest nearest to the pluton. This suggests that the cores may have formed during pluton emplacement. The bright blue

color is indicative of higher temperatures and contact metamorphism. Alternatively, the observation that there is a higher concentration of bright blue cores closer to the pluton might be coincidental. The cores may be inherited, and the variability between samples can be explained by the geologic provenance (turbidite sequence) of the area. The bright blue color in higher temperature quartz is commonly associated with the presence of titanium in the lattice (e.g. Spear and Wark, 2009). The concentrations of titanium in quartz grains from electron microprobe quantitative analysis were not sufficient to give a reliable temperature calculation (using TitaniQ, Wark and Watson, 2006), even in the brighter blue cores. When eliminating the measurements made with spectrometer Ti SP5/1, the data points taken in the core do consistently give higher totals of Ti than the points analyzed in the rims, which corresponds better with what is expected, but the measured values are still highly variable and may not be reliable. More work needs to be done to perfect the method of measuring trace amounts of Ti on the electron microprobe, or, alternatively, an apparatus more suitable for measuring trace elements in minerals, such as ICP-MS, should be employed to work out the concentrations of Ti in these rocks. Other causes for the blue CL coloring, such as other trace elements than Ti or defects, should be investigated as well.

B.6.1.3. Fracturing. The healed fractures also appear to be only present at higher concentrations in rocks closest to the pluton. The radial fracturing of the quartz grain adjacent to a biotite grain in Figure B31 suggests that the fractures formed in-situ. The fracturing may be linked to the pluton emplacement; Dutrow and Norton (1995) calculated that fluids contained in isolated pores and fractures expand when temperatures rise due to contact metamorphism, produce and maintain pore fluid pressures that are sufficient to propagate fractures closest to a pluton. During crenulation cleavage development gradients of mean stress and volumetric strains form between the different domains (P and QF) and especially at the grain interfaces the values can be high (Naus-Thijssen et al., 2010), possibly enough to cause fracturing in the quartz. Volumetric changes due to the temperature rise caused by the pluton can cause the fracturing as well.

B.6.2. Moretown Formation

The quartz grains in the sample of the Moretown Formation do show core and rim geometries that are associated with crenulation cleavage formation. The cores in the QF-domains are elongated and aligned with the S_2 foliation and the overgrowths are fairly equant in shape, consistent with the structures of the plagioclase grains in this domain as described by Williams et al. (2001). Only one small area in one sample was studied, and more CL mapping will be necessary to do any calculations regarding mass transfer of quartz during crenulation cleavage formation. A CL detector that has a larger field of view and that can be set up to create automated maps will make this exercise less time consuming.

B.6.3. Implications for Crenulation Cleavage Formation

The studied samples show the same type of fabric: crenulation cleavage, but come from two different geological settings, the results from this study only amplify that. The crenulation cleavage from the Mooslookmeguntic Pluton aureole is formed in a contact metamorphic setting, whereas the fabric in the rocks from the Moretown Formation has a tectonic history. The differences in temperature, deformation rate, fluid flow, and associated metamorphic reactions, causes that one set of samples (from the Moretown Formation) is suitable for quantifying mass transfer of both quartz and feldspar (this study and Williams et al., 2001), whereas the other set of samples shows interesting features related to the pluton emplacement, but no indication of mass transfer.

B.7. Conclusions

CL images of samples from the Mooslookmeguntic Pluton aureole and the Moretown formation were used to study the mass transfer of quartz during crenulation cleavage formation. The main findings are:

1) Quartz grains in the rocks from the Mooselookmeguntic Pluton Aureole show mottled structures away from the pluton, and grains with bright blue, fractured cores are found in samples collected closest to the pluton. The geometries of the cores and rims indicate that they are probably not associated with the crenulation cleavage formation process that can be found in these rocks. The bright cores and the fractures that are present in these samples are most likely associated with the rising temperature and rising pore fluid pressures associated with the pluton.

2) Quartz grains in the rocks from the Moretown formation do show core and rim geometries that are associated with crenulation cleavage formation, but more investigation is necessary to come to conclusions regarding the amount of mass transfer of quartz during the formation of this fabric.

BIOGRAPHY OF THE AUTHOR

Félice Naus-Thijssen was born in Geulle, the Netherlands on August 4, 1980. She grew up in Geulle, Blerick and Maastricht and graduated Atheneum at Trichter College in Maastricht in 1998. She attended Universiteit Utrecht in the Netherlands and received her propedeuse in Geology in 2000. She graduated and received her Master's of Science degree in Geology, with distinction, in February 2004. After travelling and doing volunteer work in Peru she moved to the US, together with her husband, to pursue a Ph.D. degree in 2005. Félice is a candidate for a Doctor in Philosophy degree in Earth Sciences from The University of Maine in May, 2011.